AD-A147 517 STUDY OF INFRARED ATMOSPHERIC EMISSION(U) MASSACHUSETTS 1/2
UNIV AMHERST ASTRONOMY RESEARCH FACILITY H SAKAI
DEC 83 UMASS-ARF-83-333 AFGL-TR-84-0006
UNCLASSIFIED F19628-81-K-0007 F/G 17/5 NL

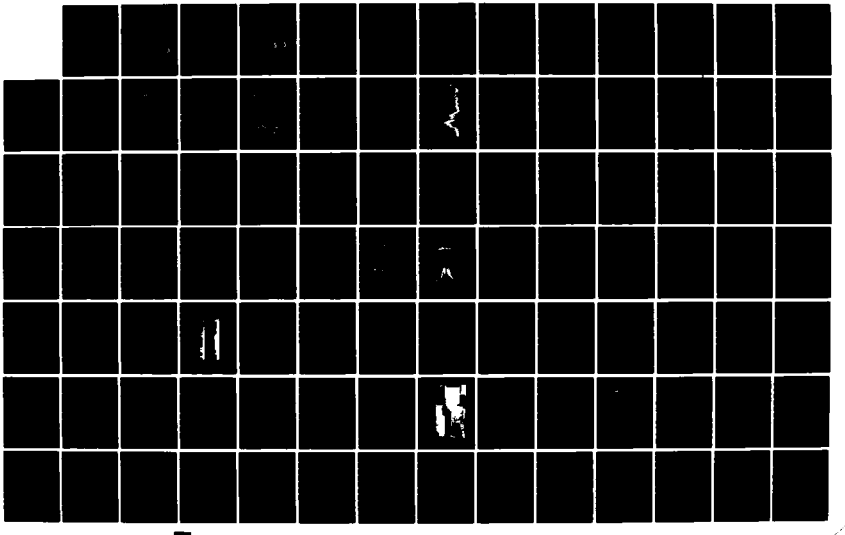

1.0
1.1
1.25
1.4
1.6
1.8
2.0
2.2
2.5
2.8
3.2
3.6
4.0

(12)

AFGL-TR-84-0006

STUDY OF INFRARED ATMOSPHERIC EMISSION

Hajime Sakai

Astronomy Research Facility
University of Massachusetts
Amherst MA 01003

AD-A147 517

Approved for public release; distribution unlimited.

December 1983

Final Report
02 October 1980 to 31 December 1983

DTIC
ELECTE
NOV 1 5 1984
S D
B

DTIC FILE COPY

AIR FORCE GEOPHYSICS LABORATORY
AIR FORCE SYSTEMS COMMAND
UNITED STATES AIR FORCE
HANSCOM AFB, MASSACHUSETTS 01731

84 11 05 107

This report has been reviewed by the ESD Public Affairs Office (PA) and is releasable to the National Technical Information Sevice (NTIS).

This technical report has been reviewed and is approved for publication

ALASTAIR FAIRBAIRN
Contract Manager

RANDALL E. MURPHY
Branch Chief

FOR THE COMMANDER

RANDALL E. MURPHY
Acting Director

Qualified requestors may obtain additional copies from the Defense Technical Information Center. All others should apply to the National Technical Information Service.

If your address has changed, or if you wish to be removed from the mailing list, or if the addressee is no longer employed by your organization, please notify AFGL/DAA, Hanscom AFB, MA 01731. This will assist us in maintaining a current mailing list.

Do not return copies of this report unless contractual obligations or notices on a specific document requires that it be returned.

UNCLASSIFIED

SECURITY CLASSIFICATION OF THIS PAGE (When Data Entered)

REPORT DOCUMENTATION PAGE	READ INSTRUCTIONS BEFORE COMPLETING FORM
1. REPORT NUMBER: AFGL-TR-84-0006	2. GOVT ACCESSION NO.: A147 517
3. RECIPIENT'S CATALOG NUMBER:	
4. TITLE (and Subtitle): STUDY OF INFRARED ATMOSPHERIC EMISSION	5. TYPE OF REPORT & PERIOD COVERED: Final Report 02 Oct 80 to 31 Dec 83
	6. PERFORMING ORG. REPORT NUMBER: UMASS-ARF-83-333
7. AUTHOR(s): Hajime Sakai	8. CONTRACT OR GRANT NUMBER(s): F19628-81-K-0007
9. PERFORMING ORGANIZATION NAME AND ADDRESS: Astronomy Research Facility, University of Massachusetts, Amherst MA 01003	10. PROGRAM ELEMENT, PROJECT, TASK AREA & WORK UNIT NUMBERS: 61102F, 2310G4AT
11. CONTROLLING OFFICE NAME AND ADDRESS: Air Force Geophysics Laboratory, Hanscom AFB, Massachusetts 01731, Monitor/Alastair Fairbairn/OPR	12. REPORT DATE: December 1983
	13. NUMBER OF PAGES: 110
14. MONITORING AGENCY NAME & ADDRESS (if different from Controlling Office)	15. SECURITY CLASS. (of this report): Unclassified
	15a. DECLASSIFICATION/DOWNGRADING SCHEDULE

16. DISTRIBUTION STATEMENT (of this Report)

Approved for public release; distribution unlimited.

17. DISTRIBUTION STATEMENT (of the abstract entered in Block 20, if different from Report)

DTIC ELECTE NOV 15 1984 S D B

18. SUPPLEMENTARY NOTES

19. KEY WORDS (Continue on reverse side if necessary and identify by block number)

Infrared Emission
Atmospheric Emission
Fourier Spectroscopy
Non-Penetrating Rydberg States
Time-Resolved Fourier Spectroscopy
Cryogenic Interferometer
PCM Signal Processing

20. ABSTRACT (Continue on reverse side if necessary and identify by block number)

Final Report of AFGL Contract #F19628-81-K-0007; describes the overall effort carried out during the contract period. Individual results obtained are assembled in the published papers accompanying this report.

DD FORM 1 JAN 73 1473 EDITION OF 1 NOV 65 IS OBSOLETE

UNCLASSIFIED

SECURITY CLASSIFICATION OF THIS PAGE (When Data Entered)

Chapter I

Introduction

The effort made for this study contract is grouped into two major categories:

(1) Experimental and theoretical study of the infrared emission generated in a low pressure gaseous glow discharge, and

(2) Processing of SCRIBE [Stratospheric Cryogenic Interferometer Balloon Experiment] data .

The first study was focused on the laboratory study of the infrared emission observable in the atmosphere above 100 km, while the second was on the field data of the infrared emission which was observed in the lower atmosphere below 30 km using a balloon-borne cryogenic interferometer spectrometer. Even though these studies are concerned with the infrared emission of the atmosphere, their characteristics are quite different . It would best be discussed separately. In this report, the study of the low-pressure glow discharge source will be discussed in Chapter II. The discussion of SCRIBE data will be made in Chapter III.

During the contract period, we produced twelve papers, mostly published in open literature. Our Scientific Report I was produced by assembling three papers out of these twelve works. This report is accompanied by most of our publications, eight papers.

or
n
By
Distribution/
Availability Codes
Dist | Avail and/or Special
A-1

Even though Sakai authored this report by taking a chief responsibility of assembling the works accomplished under this contract, his contributions to those published works are limited. His name, which appears on the front page of this report, should be considered as to signify his editor's role for the report. Many people made contributions leading to joint publication. Some of them were either principally or partially supported under this contract. Some publications were resulted from a collaboration with workers at different institutions. Nonetheless, the support made available under this contract was instrumental in completing those published works.

The following list summarizes our publications and presentations supported in part by this contract.

Publications:

Chang, Edward S. and Hajime Sakai, "The 5g Levels of Atomic Nitrogen," J. Phys. B: 14, L391 (1981)

Sakai, Hajime, P. Hansen, M. Esplin, R Johansson, M. Peltola and J. Strong, "Infrared Emission Spectroscopy of Glow Discharge Formed in Low Pressure Atmospheric Gases," Appl. Opt. 21, 228 (1982)

Mayants, L. S., "A New Rotation-Vibration Hamiltonian," (1982)

Sakai, H., and E. S. Chang, "Properties of Ions from Spectroscopic Data," J. Phys. B 15, L649 (1982)

Chang, Edward S., "Theory of Angular Distributions of Electrons Resonantly Scattered by Molecules. III. The Broad Resonance in N_2 and CO at 20 eV," Phys. Rev. A 27, 709 (1983).

Sakai, H., T.C. Li, W.Barowy, S.Pulchtopek, J.Pritchard, F.J. Murcray, F.H. Murcray, and G. Vanasse, "Study of Atmospheric Infrared Emission Using A Balloon-Borne Cryogenic Fourier Spectrometer," SPIE Proc. Vol. 364, 38 (1983).

Sakai, H. and G. Vanasse, "Atmospheric Infrared Emission Observed at Altitude of 27000 to 28000 m," SPIE Proc. Vol. 366, 165 (1983).

Chang, Edward S., "Theory of Rotational Branch Structure with Application to N_2 and CO," J. Phys. B 15, L873 (1982).

Chang, Edward S. and K. Yoshino, "The nf Complexes in Molecular Nitrogen," J. Phys. B, in press (1984).

Chang, Edward S., Stanley Pulchtopek, and E.E. Eyler, "Extended Analysis of 5g-4f Emissions in H_2," J. Chem. Phys., in press (1984).

Barowy, W. and H. Sakai, "Time Resolved FTS of Molecular and Atomic Infrared Emission," Infrared Physics, in press (1984).

Sakai, H., G. Vanasse, J. Pritchard, F.J. Murcray, "Cryogenic Fourier Spectroscopy for the Infrared Atmospheric Emission Measurement," to be submitted to Appl. Opt.

Presentations:

R. Johansson, M. Peltola, and H. Sakai, "Infrared Emission Spectroscopy of Atmospheric Atoms and Molecules," and Mark P. Esplin and Hajime Sakai, "High Temperature Absorption Spectrum of 4.3 Micron CO_2," presented at OSA Topical Meeting on Spectroscopy in Support of Atmospheric Measurements, Sarasota FL, November 1980.

H. Sakai, "The $w^1\Delta_u$-$a^1\pi_g$ (0-0) Band of N_2," presented at OSU 36th Annual Symposium on Molecular Spectroscopy, June 1981.

E.S. Chang, "Theory of IR Spectra from Rydberg- Rydberg Non-penetrating State Transitions," and L.S. Mayants, "New Rotation-Vibration Hamiltonian," presented at OSU Molecular Spectroscopy Symposium, June 1982.

H. Sakai and G. Vanasse, "Stratospheric Infrared Emission Observed by Balloon-Borne Cryogenic Interferometer Spectrometer," OSA Annual Meeeting, October 1982.

H. Sakai, "Molecular Constants of $^{12}C^{16}O_2$ Bands in 1900 cm^{-1} ~ 2150 cm^{-1}," and E.S. Chang, "Identification of the nf Complexes in N_2 by UV Absorption"; and E.S. Chang, "Absorption of the 5g-4f Emission Lines in H_2," presented at OSU Molecular Spectroscopy Symposium, June 1983.

Chapter II

Study of the infrared emission generated in a low-pressure gaseous glow discharge

Our study was conducted using a 12-meter-long glow discharge column shown in Figure 1. In the early part of our study , we found that the source was good in generating various species involved in the infrared emission of the upper atmosphere. However, their spectral characteristics were rather uncontrollable; we were not able to control their temporal behavior concerning the excitation or the relaxation. Their observed radiative temperatures were so extraordinary that the spectral data provided no clue for analysing what was happening in the glow discharge process. We decided to develop the time-resolved technique for making a detailed observation of the infrared emission at various phases of excitation-relaxation process in our glow discharge source.

We set the primary experimental objective to detect the atmospheric infrared emission species as many as possible, thus allowing the chemistry processes in the source to occur in a maximum extent. The flow rate of molecules in the discharge region was very slow. A molecule injected in the source was subject to many discharge cycles, in an order of 10^3, before it was pumped out from the source chamber. The discharge cycle was set to be as slow as possible for achieving a stable

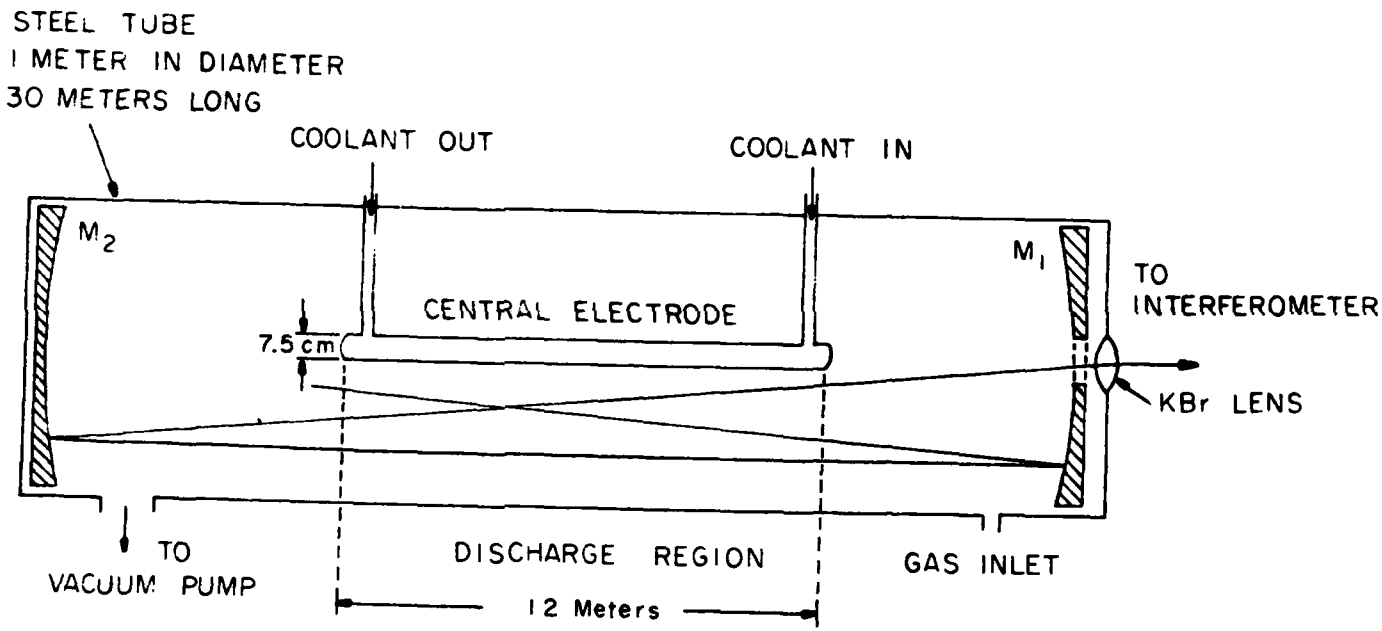
STEEL TUBE
1 METER IN DIAMETER
30 METERS LONG
COOLANT OUT
COOLANT IN
M2
M1
TO
INTERFEROMETER
CENTRAL ELECTRODE
7.5 cm
KBr LENS
TO
VACUUM PUMP
DISCHARGE REGION
GAS INLET
12 Meters

Figure 1

excitation-relaxation cycle in the emission. As a result, we were able to pick up various species, and at the same time we established no control over their excitation-relaxation evolution sequence.

The glow-discharge source was activated by applying an ac house-current of 60 Hz. The voltage at the power supply was varied up to 1000 V r.m.s, or 1400 V peak. The ballast resistance, connected in series with the discharge electrode, somewhat regulated the discharge-voltage to a constant value of 600 V. This figure was observed to be held constant, independent of the supply voltage. The current was varied by setting the supply-voltage to a desired value. Thus by setting the supply-voltage to a higher value, we were able to feed a heavier discharge current. There was a distinctively different current behavior between the two opposite polarity phases; i.e., between the phase when the central electrode was positively charged and that negatively charged. The single-polarity operation led to unstable discharge, unfit to our experimental measurement. The central electrode had to be alternately charged with opposite polarity in order to achieve a stable glow discharge in the chamber.

The technique of time-resolved Fourier spectroscopy is outlined in one of our papers [Barowy and Sakai (1984)]. One of the experimental requirements imposed on us was to gain a

reasonable signal-to-noise ratio in the observation of a relatively weak emission source. Since our source emission was generated in a repetitive pattern, our experiment was best done by implementing a step-and-hold scanning to the interferometer drive. That is to say, the interferometer was held at a given optical-path-difference position for an indefinite duration to accumulate a desired amount of the signal until a reasonable signal-to-noise ratio was achieved. Our scheme was more versatile than those developed by the French group, when the system was applied to the time-resolved measurement.

For maintaining a technical simplicity to our interferometer instrumentation, we decided to use the intensity of the laser-fringe signal as the servo-control signal.The alignment stability in the interferometer circuit, which was a paramount importance for such a servo-control scheme, was provided by an automatic optical retroreflecting tilt-compensating scheme. We adopted a pair of the readily available lightweight hollow corner-reflectors, replacing a set of the plain mirrors in both arms of the interferometer. At the same time a silicone fluid of higher viscosity than the one supplied in the original interferometer was tried, hoping to attain a quicker dissipation of the kinetic energy of the movable carriage. The interferometer drive mechanism designed with a large damping term is to achieve a fast-acting stepping drive motion. At present , we find the new damping fluid and the

existing dash pot structure in the original design provides an adequate stepping speed of approximately 10 steps per second. The present operation does not require the stepping speed of this magnitude, as the measurements deal with a weak source. The drive motor was energized by a series of the fast impulses. The control electronics and other pertinent servo-logics are described in our paper cited above.

Replacement of the plain mirrors with the hollow retro-reflecting corner mirrors in the interferometer arms lowered the mechanical precision required on the way system of the interferometer drive. The movable carriage was held much more loosely than the conventional design, resulting in a substantial reduction of the harmful static friction in its motion.

The data shown in Figure 2 are the time-resolved spectra of the N_2 glow-discharge emission. The data shown in Figure 3 are those of the O_2 emission. It is noticeable that the emission generated in an electric polarity phase differs vastly from that in another phase. The electric field at the central electrode of our source configuration is approximately 13.5 times stronger than that at the outer electrode. The electronic emission by the field is likely to occur only when the central electrode is negatively charged [the negative phase]. The electronic emission from the outer electrode is less likely

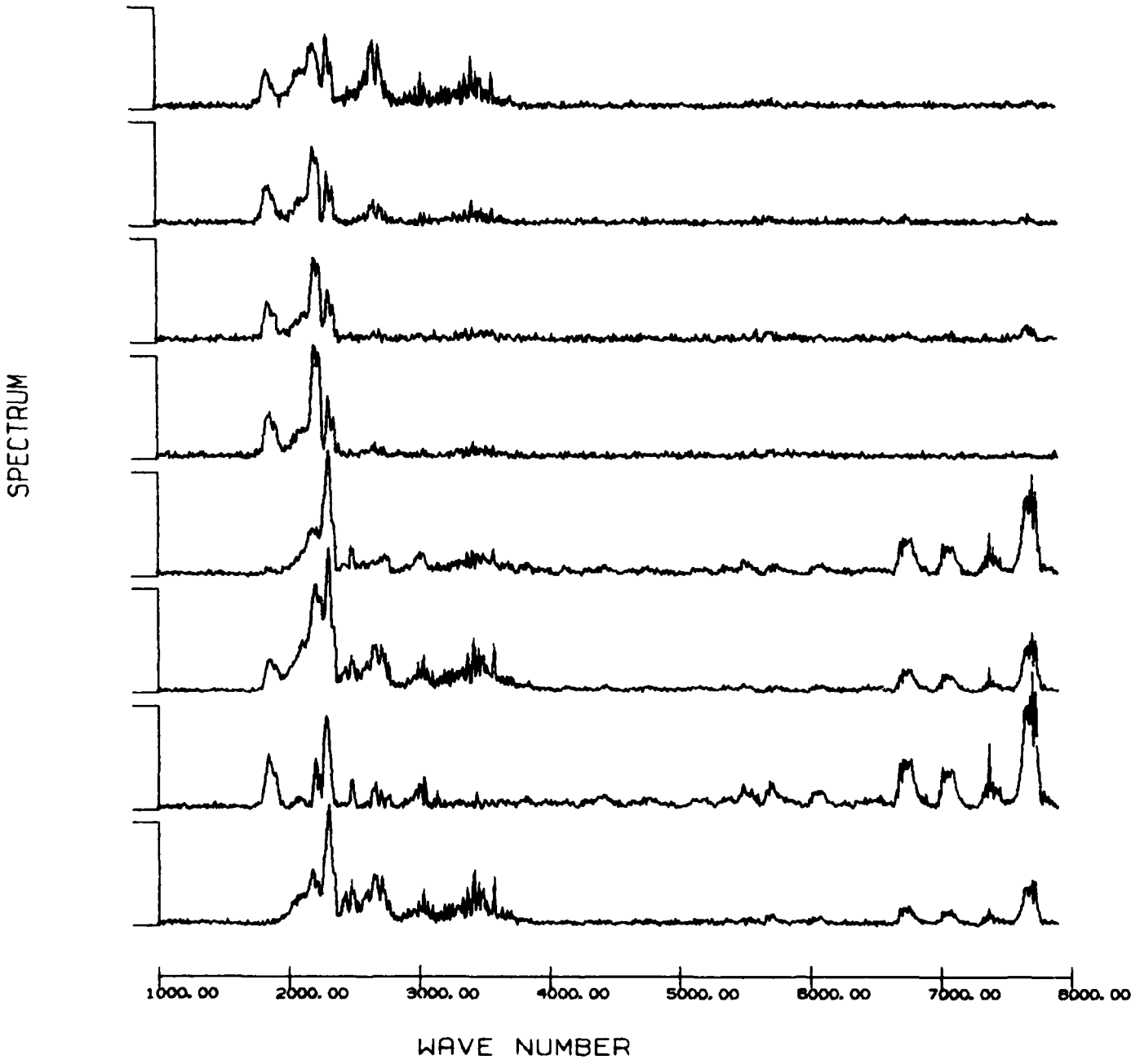

Fig. 2(a) Time-Resolved Spectral Data (Glow Discharge in N_2)

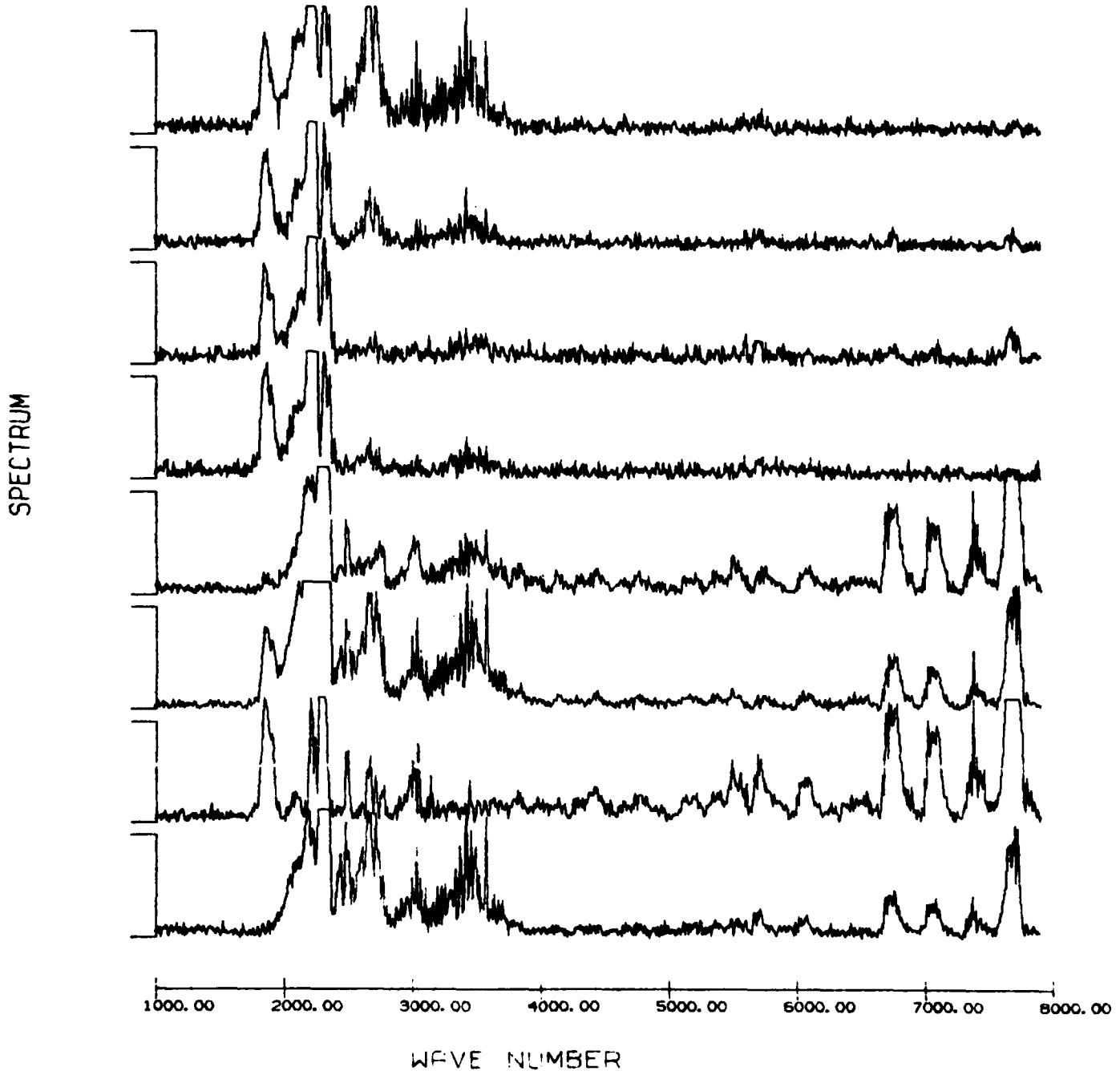

Fig. 2(b) Display of Fig. 2(a) with a larger gain factor.

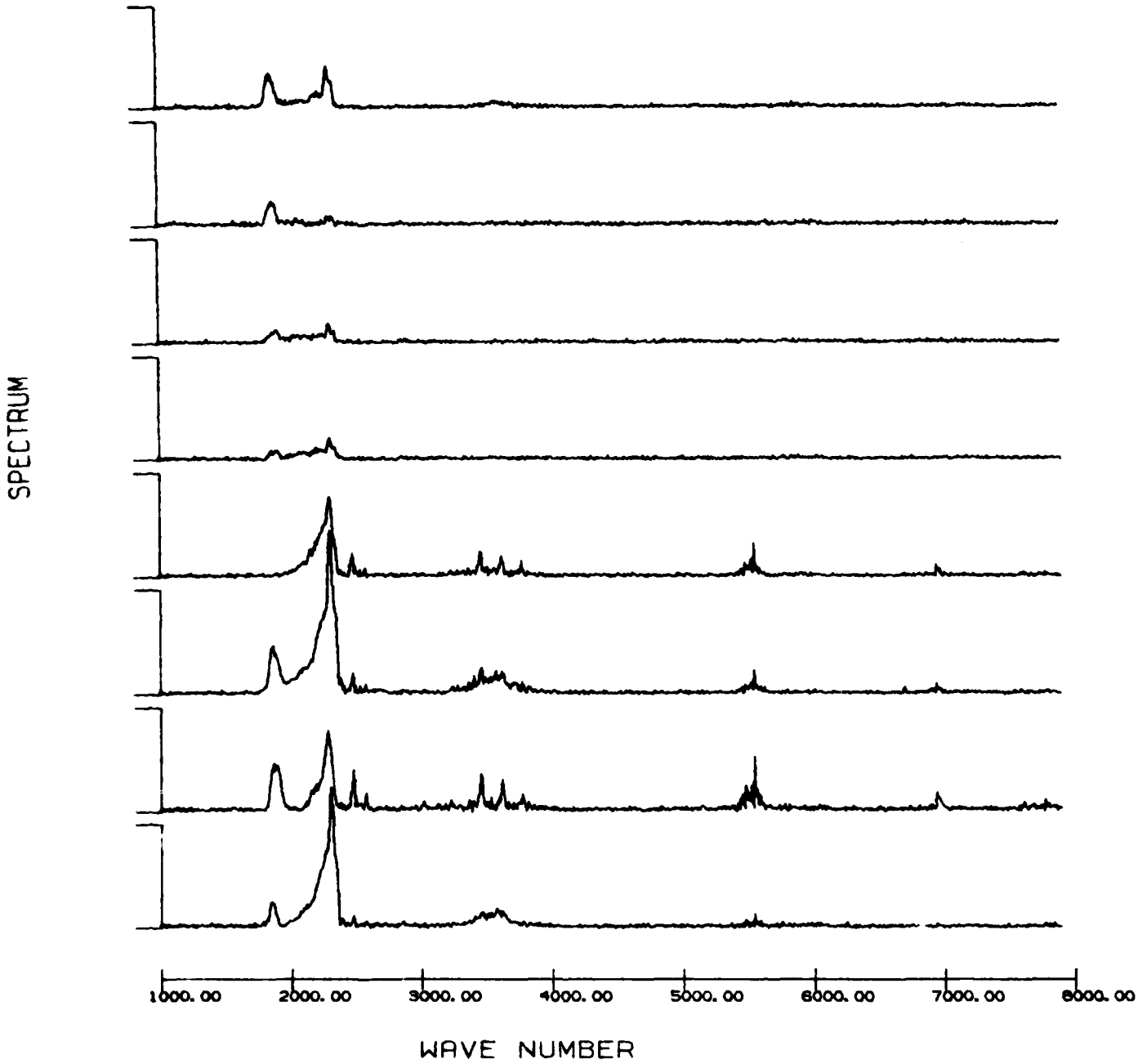

Fig. 3(a) Time-Resolved Spectral Data (Glow Discharge in O_2)

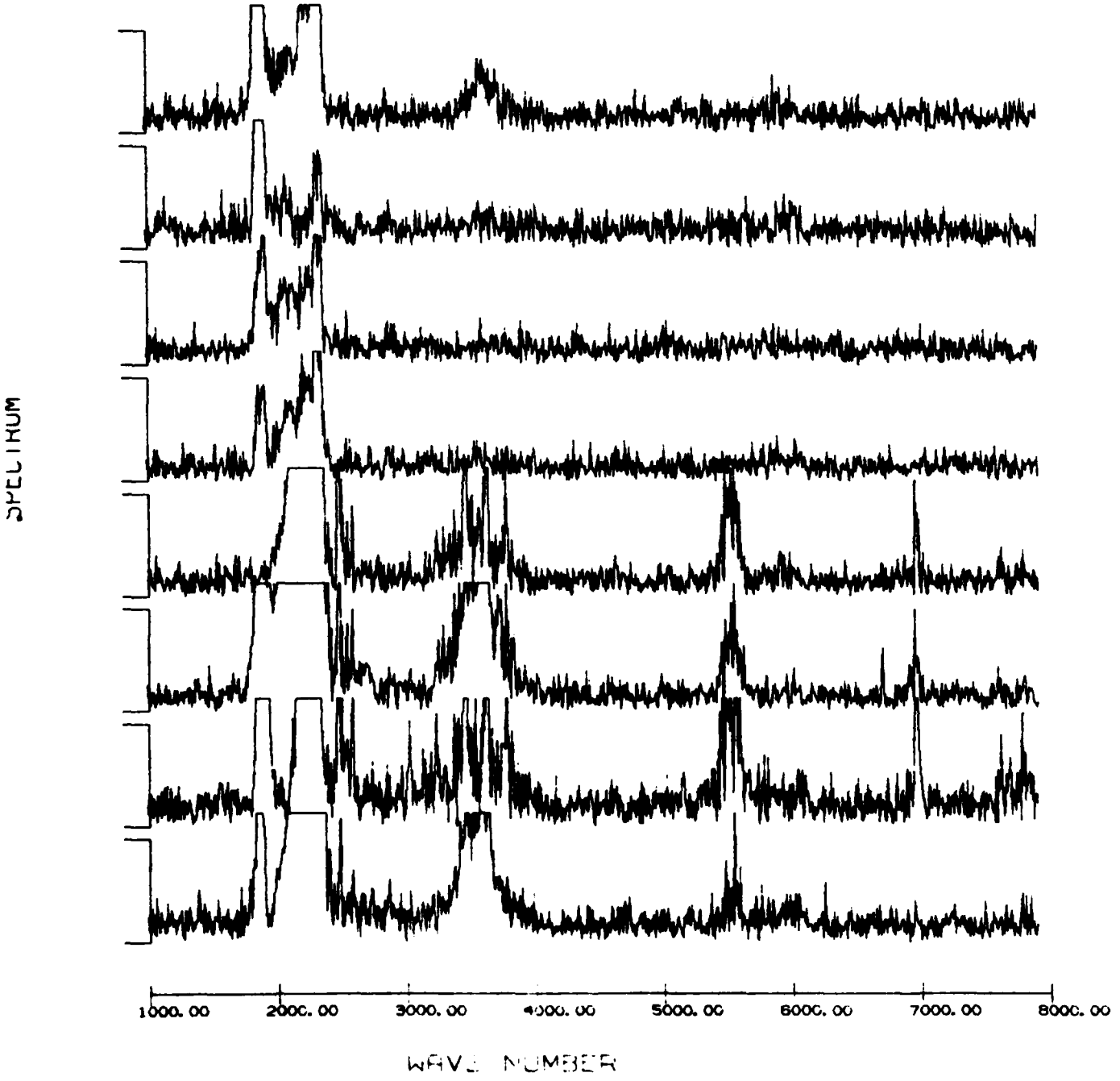

Fig. 3(b) Display of Fig. 3(a) with a larger gain.

even when that electrode is negatively charged [the positive phase]. The current observed during the positive phase is very likely carried by the positive ions, which have the mobility approximately 100 times slower than the electrons. As a consequence, the electric conduction during the negative phase is done by both the electrons and the positive ions, while the electrons are depleted from the conduction during the positive phase. Meanwhile, the current magnitudes are observed to be equal for both polarity phases. This does not mean that the current carriers in the discharge chamber are equalized for both phases. It indicates that the total amount of the current leaving the discharge chamber remains the same for both phases. A majority of the carriers moves toward the outer electrode during the positive phase, while during another phase two kinds of the carriers move in opposite directions. Those species excited by the electron collision are very likely observable only during the negative phase. The time-resolved measurement is very suitable to observe the difference in the radiative emission between these two phases. It provides a very powerful means for revealing an intricate change in the spectral characteristics at various stages of the excitation-relaxation sequence. The time-resolved data shown in Figures 2 and 3 demonstrate the capability provided by the technique in following the temporal sequence of each spectral system. For our primary goal of detecting a particular atmospheric species, we can find the most favorable time phase for the observation. The spectrum of NO^+

shown in Figure 4 gives another example of the power of the time-resolved Fourier spectroscopy technique.

During the course of our spectral analysis effort, we came to realize the structure observed at a vicinity of 2500 cm^{-1} in various spectral data can be interpreted as the 4f-5g transition of either atomic or molecular species. We had a good success in identifying the 4f-5g transition lines of the atomic nitrogen for both the line positions and the line intensity. Subsequently our theoretical effort was extended principally by E. Chang and several co-operative efforts brought a fruitful development.

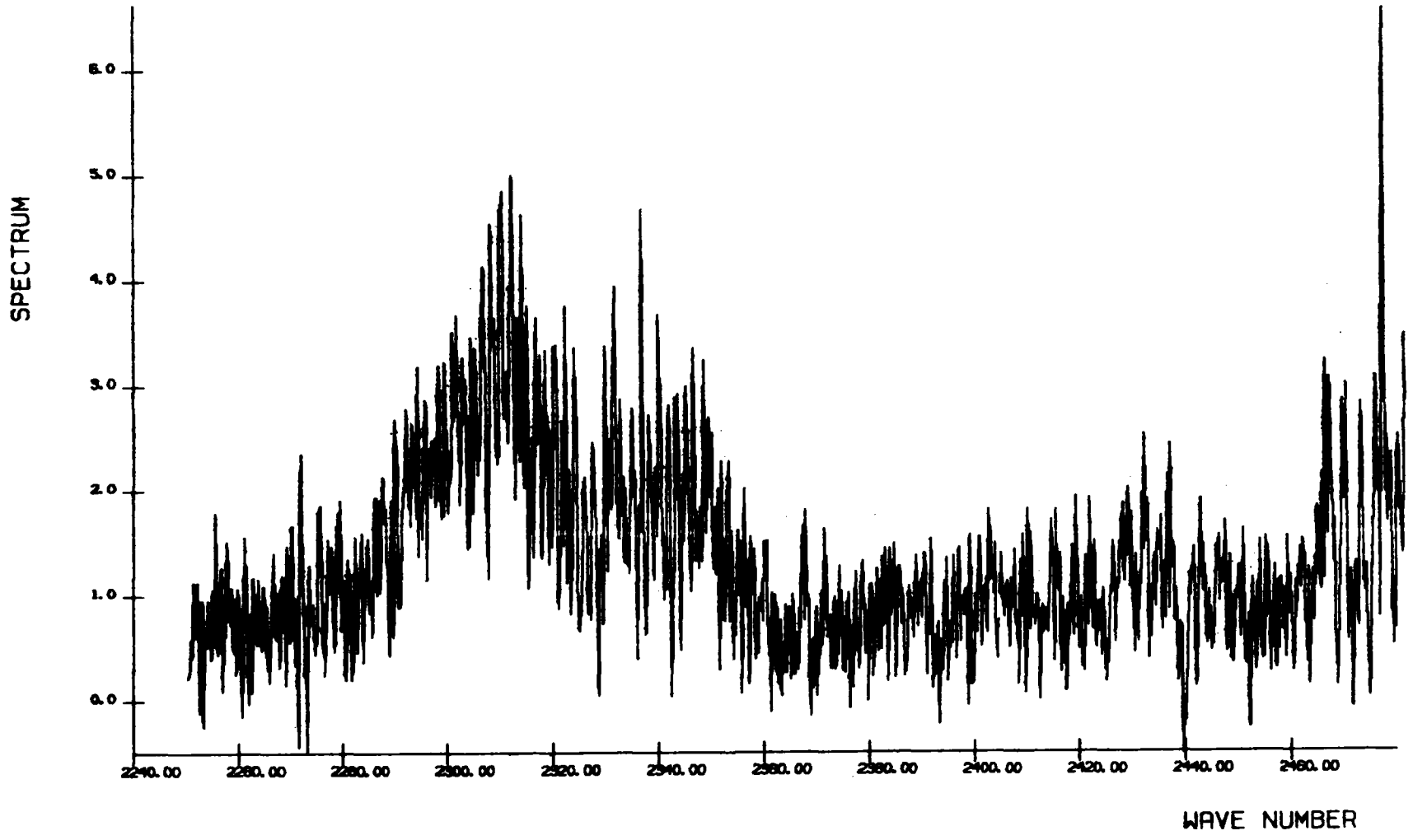

Fig. 4 NO^+ Emission

Chapter III

SCRIBE Data Processing

The work performed under the present contract for the AFGL SCRIBE program was an ongoing effort. The program itself has been described in several of our publications as well as in our previous reports. Our participation may be summarized into three major parts:

(1) Extraction of the interferogram data from the PCM telemetry data tape;

(2) Processing of the interferogram data for the spectral retrieval; and

(3) Analysis of the obtained atmospheric emission data.

Our Scientific Report II of this contract was assembled on the SCRIBE II flight data [Oct. 1982]. The parts (2) and (3) have been documented in our previous reports. The following description is on the part (1), the extraction of the interferogram data from the PCM telemetry data tape.

Introduction

The stratospheric cryogenic interferometer balloon program is a balloon-borne experiment, intending to obtain the stratospheric emission data observed along the horizontal line of sight. Four groups are involved from the onset of the program, AFGL, Idealab Inc., University of Denver and University of

Massachusetts. The obtained data during the balloon flight are transmitted to the ground station via a radio communication link. The instrumentation for this radio link was developed under a direction of the AFGL Balloon Branch which is in charge of the balloon flight operation.

PCM Telemetry Signal

The basic form of the telemetry signal is a 72-bit sequence in a binary bipolar non-return-zero-level [NRZL] format. The signal is constructed in a form of the pulse-coded modulation signal [PCM]. All the pertinent data for the flight-experiment including the digitized interferogram data are processed by the on-board PCM encoder into a 72-bit frame pattern. Each frame is made of a 20-bit synchronization identification word, a 4-bit subframe identification counter number, a 16-bit interferogram data, and four 8-bit housekeeping data. The synchronization ID code shown in Table I provides a key for identifying the basic PCM clock rate and the frame length. The interferogram data are a 12-bit output of the detector amplifier signal and a 4-bit word which indicates the status regarding its validity, the interferometer drive status, and the amplifier gain status.

The telemetry data are transmitted from the flight package at a rate of 800 K bit per second, and they are recorded on the analog magnetic tapes at the ground station. The spectral recovery process in Fourier spectroscopy requires all the

interferogram data taken at every sampling position. The extraction process of the interferogram data , therefore, allows no failure in recovering them from the recorded telemetry data which are subjected to various electrical interferences. A considerable time and effort were spent by us for achieving an improved reliablility of recovering the interferogram data from the telemetry record.

General Layout of Processing Scheme

The data extraction scheme currently used at our facility is shown in Figure 5 . The PCM telemetry record on the magnetic tape was played back by using the Honeywell 101 tape recorder. The recovered PCM signal was sent to the PCM decommutator, which produced two outputs, a parallel 16-bit signal and a clock signal synchronous to the incoming PCM signal. The home-built interface electronics between the PCM decommutator and the PDP 11/20 computer provided a temporary storage of a proper 16-bit word extracted from the serial 72-bit string of the telemetry signal, and it sent a 16-bit output to the DR11-B I/O interface of the PDP computer. The data transferred into the central memory of the PDP were eventually stored on the disk memory [RK1], and at the end they were copied onto the magnetic tape using the PIP [Peripheral Interchange Program] of the RT11 software package.

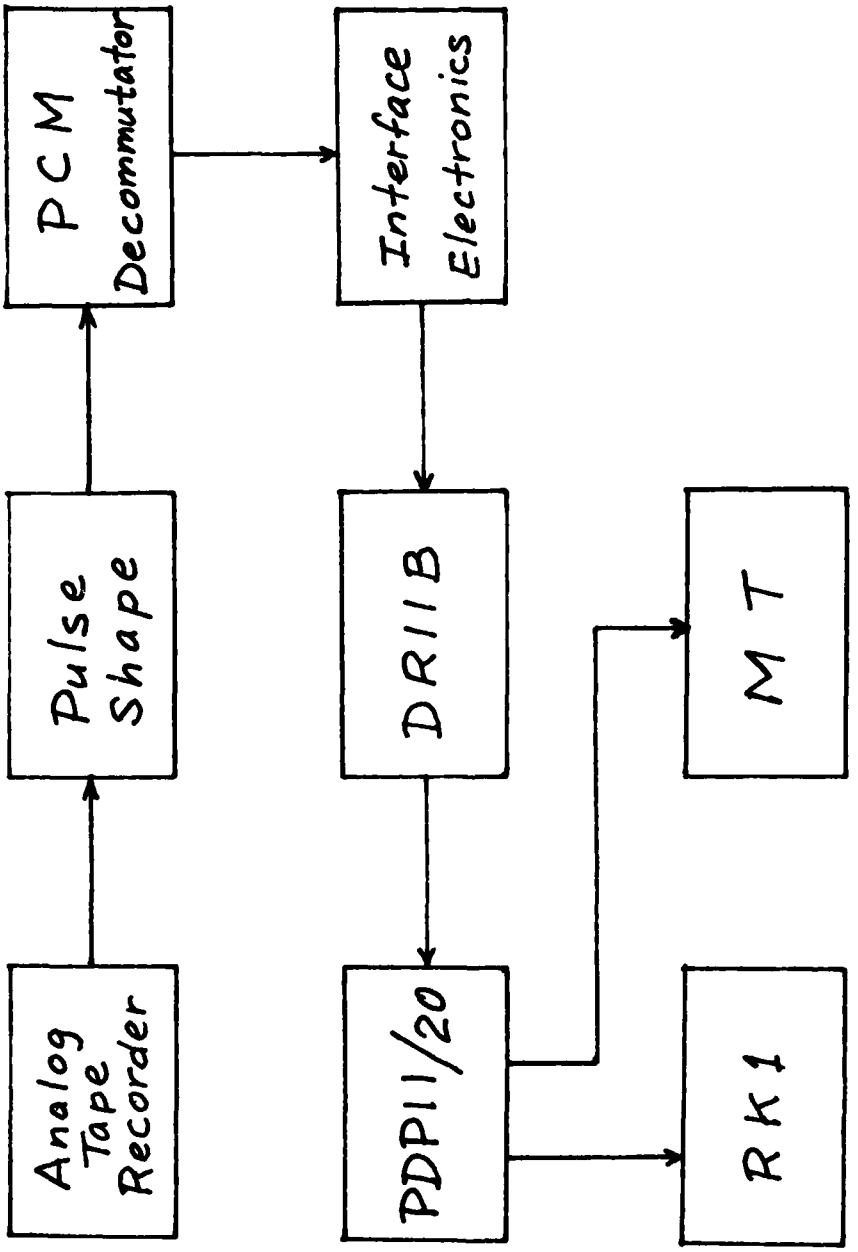

Fig. 5 Block Diagram of PCM Data Extraction Scheme

The data extraction was essentially controlled by two factors, a signal-to-noise ratio of the played-back PCM signal, and a timing jitter contained in it. The computer simulation test showed that with the specified bandwidth in the PCM electronics train the timing jitter would not exceed a figure more than a 128-th of the basic PCM pulse width, even if the harmonic distortion in the played-back signal appeared to be rather bad. We found that a pulse shaping network made by using the broadband operational amplifier, Tektronix AM501, worked adequately for our setup. The PCM decommutator used was designed for a bit rate much slower than our 800 K bit per second, and it was modified in a patchwork manner until we obtained the latest data.By taking an advantage of relatively less busy time available to us between the flights, the PCM decommutator was extensively studied and the modifications, which we concluded to be necessary from the study, were permanently implemented.

PCM Decommutator

The original design of our PCM decommutator called for a rate of 10 Kbit per second , which was far lower than our 800 KBS.In addition its synchronization logic assumed an absence of a long non-changing bit pattern, which was always present in our PCM signal. We concluded that an extensive redesign of some logics was necessary to achieve improved reliability of the operation.

The basic scheme used in our system is sketched in Figure 6. The transition detector provides a sharp pulse every time when the PCM signal undergoes an amplitude transition. The SPD phase detector operates on the clock signal generated at the VCO [voltage controlled oscillator] timing circuit and the PCM transient pulse; every time when these pulses arrive within a prescribed time interval, the SPD triggers the storage register to pass the output of the 4-bit counter to the digital-to-analog converter. The servo-error signal to the VCO which operates at an approximate rate of 16 times the basic PCM clock rate, is generated only at an instant when the transition detector provides a pulse to the SPD. A lengthy non-changing bit pattern which is present in our PCM signal makes the servo-loop in the VCO inactive, and thus the VCO locks its clock rate at the same value. Consequently no shifting of the VCO clock rate occurs in such a pulse train. All circuits which deal with fast pulse train are constructed using the fast Schottky series IC. No significant time delays are observed in our circuit when we apply the circuit for our 800 KBS PCM signal.

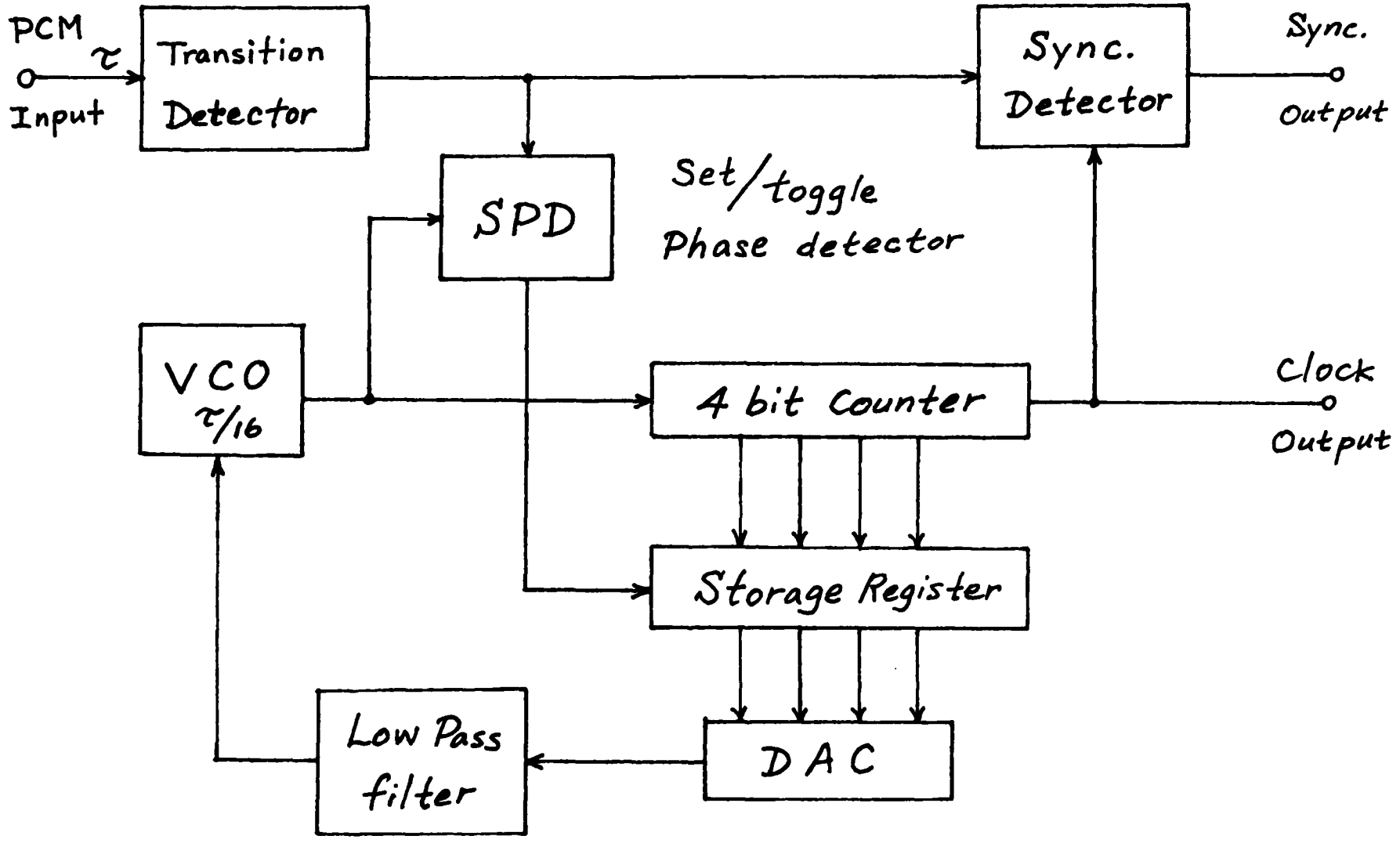

Fig. 6 Improved Bit-Synchronization Scheme

J. Phys. B: At. Mol. Phys. 15 (1981) L649–L653. Printed in Great Britain

LETTER TO THE EDITOR

Properties of ions from spectroscopic data

Edward S Chang and Hajime Sakai

Department of Physics and Astronomy, University of Massachusetts, Amherst MA 01003, USA

Received 15 July 1982

Abstract. From the spectroscopic data of non-penetrating Rydberg states of C I, N I, O I and Ne I, we have extracted the polarisability and the quadrupole moment of the ionic core. The values so obtained from different Rydberg nl levels are mutually consistent to within 1%. Comparison with the values from *ab initio* calculation shows agreement to a few per cent. Further, some empirical relations between certain Slater integrals are shown to be the direct consequence of our treatment.

It has long been known that the ionic polarisability of close-shell cores can be extracted from the energy levels of their non-penetrating Rydberg states (Edlén 1964). For the case of the two-electron core, Ölme (1969) has shown that the values of the polarisability of Li^+, Be^{2+} and B^{3+} so obtained agree with the best theoretical values to better than one per cent. In the case of open-shell cores, Rydberg states are usually analysed in the 'pair-coupling' theory (Eriksson 1956) or equivalently in the jK-coupling scheme (Humphreys *et al* 1967). Such analyses yield the average energy of each nl level (the centre of gravity), the core fine-structure splittings, the Slater integral $F_2(nl)$ and other parameters which are usually very small. Using these determined quantities, known states can be theoretically obtained accurately and unknown states can be predicted. While the value of the polarisability had been determined from the average energy in some open-core cases, it was thought that its interpretation as the core polarisability had to be modified (Litzen 1968). Consequently, no attempt was made to compare its value with the ones from *ab initio* calculations.

In this letter, we determine the polarisability of atomic cores with the configuration $2p^q$ from the average energy, and show that it agrees with theoretical values to a few per cent. More importantly, we find that the electric quadrupole moment of the core can be obtained directly from the $F_2(nl)$ integrals. Finally, the two empirical relations, (i) $n^3F_2(nl) = \text{constant}$, noted by Eriksson and Johansson (1961), and (ii) $F_2(5g)/F_2(4f) = 0.0466$, noted by Eriksson (1967), are derived explicitly. In fact, all $F_2(nl)$ are expressible as a product of the core's quadrupole moment and an analytically known proportionality constant.

The system under investigation consists of an atomic core with a well defined fine-structure labelled by the quantum number j ($\boldsymbol{j} = \boldsymbol{L}_c + \boldsymbol{S}_c$) and a non-penetrating Rydberg electron with orbital angular momentum l (typically $l \geqslant 3$). The interaction between the electron and the core is not represented by the usual quantum defect (because the electron does not penetrate the core), but by long-range interactions. The two dominant interactions are well known to be the polarisation potential and

0022-3700/82/180649+05$02.00 © 1982 The Institute of Physics

The U.S. Government is authorized to reproduce and sell this report. Permission for further reproduction by others must be obtained from the copyright owner.

the electric quadrupole potential given in au by

$$V = -\frac{e^2\alpha}{2r^4} - \frac{eQ}{r^3} P_2(\cos\theta). \tag{1}$$

In equation (1), α is the isotropic polarisability and Q is the quadrupole moment defined by (Fano and Racah 1959)

$$Q = -e(L_c\|C^{[2]}\|L_c)\langle r^2\rangle. \tag{2}$$

Treatment of equation (1) by perturbation theory, given elsewhere (Chang and Sakai 1982), yields results mathematically equivalent to pair-coupling theory. For non-penetrating states, the Rydberg electron is always exterior to the core electrons. Therefore in the Slater integral, $r_<$ refers only to the core (2p) electrons and $r_>$ to the Rydberg (nl) electrons, and the integral is then given by

$$F^2(2\mathrm{p}, nl) = e^2\langle r^2\rangle_{2\mathrm{p}}\langle r^{-3}\rangle_{nl}. \tag{3}$$

The last integral is given by Bethe and Salpeter (1967),

$$\langle r^{-3}\rangle_{nl} = \frac{\zeta^3}{n^3 l(l+\frac{1}{2})(l+1)} \tag{4}$$

where ζ is the net charge on the ionic core. With the definition $F_2(2\mathrm{p}, nl) = F^2(2\mathrm{p}, nl)/D_2(l)$ where $D_2(3) = 75$ and $D_2(4) = 385$, it is evident that

$$n^3F_2(nl) = \frac{e^2\zeta^3\langle r^2\rangle_{2\mathrm{p}}}{l(l+\frac{1}{2})(l+1)D_2(l)}. \tag{5}$$

Clearly the right-hand side of equation (5) is a constant for a particular atomic species and for a fixed value of l, as required by the first empirical observation (Eriksson and Johansson 1961). Now from equations (3) and (4), the ratio

$$F_2(2\mathrm{p}, 5\mathrm{g})/F_2(2\mathrm{p}, 4\mathrm{f}) = \frac{4^3\times 3\times\frac{7}{2}\times 4\times D_2(3)}{5^3\times 4\times\frac{9}{2}\times 5\times D_2(4)} = \frac{4^3}{5^3\times 11} = 0.046545$$

which is the second empirical rule (Eriksson 1967).

We now proceed to evaluate the core properties, α and Q, from spectroscopic data. The evaluation of α follows the standard procedure (Edlén 1964). The energy shift Δ_p of a Rydberg level is usually already found or can be obtained from the average energy E_0 and the series limit. Then $\Delta_p = \zeta^4\alpha P(n, l)$, where

$$P(n, l) = \langle r^{-4}\rangle_{nl} = R\,\frac{3n^2 - l(l+1)}{2n^5(l-\frac{1}{2})l(l+\frac{1}{2})(l+\frac{3}{2})} \tag{6}$$

is tabulated by Edlén (1964). We have ignored the contribution due to the induced quadrupole polarisability because a non-adiabatic correction was about the same order of magnitude but opposite in sign (Deutsch 1970). Table 1 shows the polarisabilities of C^+, N^+, O^+ and Ne^+ so obtained from the spectra of C I, N I, O I and Ne I. Note that for each ion the polarisability extracted from different Rydberg levels is consistent to within 1%. Two exceptions are easily explained by the original spectral lines being blended, and therefore inaccurate.

As indicated in equation (2), the quadrupole moment contains the radial matrix element $\langle r^2\rangle_{2p}$ which in turn can be extracted from the spectroscopic constant F_2 as shown in equation (3). Table 2 shows F_2 and $\langle r^2\rangle_{2p}$ obtained from the same Rydberg

Table 1. Polarisability from Rydberg levels.

Species	C I		N I		O I		Ne I	
nl	Δp (cm^{-1})	$\alpha(a_0^3)$	Δp (cm^{-1})	$\alpha(a_0^3)$	Δp (cm^{-1})	$\alpha(a_0^3)$	Δp (cm^{-1})	$\alpha(a_0^3)$
4f	23.22[a]	5.69	14.99[c]	3.67	10.42[f]	2.55	5.41[h]	1.33
5f	13.38[a]	5.72	8.59[c]	3.67	6.03[f]	2.58	3.11[h]	1.33
6f	8.20[a]	5.72	5.16[d]	3.60	3.71[f]	2.59	1.90[h]	1.33
7f	5.34[a]	5.73			2.42[f]	2.59	1.23[h]	1.32
8f	3.81[a,b]	(5.97)					0.84[h]	1.32
9f							0.60[h]	1.31
5g			2.05[e]	3.68			0.74[h]	1.32
6g					0.97[f,g]	(2.72)		

[a]Johansson (1965).
[b]Some components blended, some with J unidentified.
[c]Eriksson and Johansson (1961).
[d]McConkey *et al* (1968).
[e]Chang and Sakai (1981).
[f]Moore (1976).
[g]Blended.
[h]Litzen (1968).

Table 2. $\langle r^2\rangle_{np}$ from Rydberg levels.

Species	C I		N I		O I		Ne I	
nl	F_2 (cm^{-1})	$\langle r^2\rangle_{2p}(a_0^2)$	F_2 (cm^{-1})	$\langle r^2\rangle_{2p}(a_0^2)$	F_2 (cm^{-1})	$\langle r^2\rangle_{2p}(a_0^2)$	F_2 (cm^{-1})	$\langle r^2\rangle_{2p}(a_0^2)$
4f	2.80[a]	2.57	1.965[c]	1.805	0[f]	—	[71.42[h]/n^3	1.025]
5f	1.45[a]	2.60	1.000[c]	1.794	0[f]	—		
6f	0.84[a]	2.60	0.580[d]	1.798	0[f]	—		
7f	0.54[a]	2.61			0[f]	—		
8f	0.35[a,b]	(2.57)						
9f								
5g			{0.0948[e]	1.871				
			{0.08667	1.710				
6g					0[f,g]	—	0.0519[h]	1.024

[a] [b]Same as in table 1.

levels and atomic species as in table 1. Once again, the consistency is within 1%. In fact for Ne I, $F_2(nf)$ fitted the n^{-3} relation to within the experimental error and were not given separately for each n (Litzen 1968). In the case of N I, our $F_2(5g)$ is obtained from only two states (the unperturbed $K = 2$ and 6) of the data of Chang and Sakai (1981). This value differs by 8% from the theoretical value 0.086 67 cm^{-1} of Eriksson (1967). A more reliable value will be available when our data is fully analysed (Chang and Sakai 1982). Technically, the value for F_2 or $\langle r^2\rangle_{2p}$ extracted from spectroscopic data includes higher-order terms than just the first-order energy. Consequently, the quadrupole moment so obtained is the effective quadrupole moment, which includes a small contribution from the anisotropic polarisability.

To complete the determination of the quadrupole moment, we need to evaluate the reduced matrix element in equation (2). For the ^{2}P core, Fano and Racah (1959) give

$$(1\|C^{[2]}\|1) = 3\begin{pmatrix} 1 & 1 & 2 \\ 0 & 0 & 0 \end{pmatrix} = \sqrt{\tfrac{6}{5}}.$$

The other configurations of interest p^2 and p^3 are treated in Slater (1960). Obviously configurations $2p^{6-q}$ give the same values except for the sign, as negative electrons are replaced by positive holes. These results are displayed in table 3.

Finally, we summarise our atomic properties by showing their mean values with standard deviations and compare them with theoretical values in table 4. Our polarisabilities are in excellent agreement with the polarised pseudo-states calculation of Hibbert *et al* (1977). Similarly, our quadrupole moments agree very well with theoretical values, even though those of Sen (1979) are for a different system with an additional 3s electron.

We conclude that the polarisability and the quadrupole moment of an atomic core can be extracted from non-penetrating Rydberg states with an accuracy of 1%. These values are useful in the calculation of photoionisation, free–free transitions and as tests for wavefunctions and computational methods. In spectroscopy, we have derived the two empirical rules observed by Eriksson and will show how the core properties can be used to predict other Rydberg states.

Table 3. The reduced matrix element in equation (2) $-e(L\|C^{[2]}\|L)$.

Configuration \ L	S	P	D
np		$-e\sqrt{\frac{6}{5}}$	
np^2	0	$+e\sqrt{\frac{6}{5}}$	$-e\sqrt{\frac{14}{5}}$
np^3	0	0	0
np^4	0	$-e\sqrt{\frac{6}{5}}$	$+e\sqrt{\frac{14}{5}}$
np^5		$+e\sqrt{\frac{6}{5}}$	

Table 4. Polarisability and quadrupole moment.

	$\alpha(a_0^3)$		$Q(ea_0^2)$	
	Present	Theory	Present	Theory
C^+	5.72 ± 0.02	5.62[a]	−2.82 ± 0.02	−2.834,[b] −2.804[c]
N^+	3.66 ± 0.04	3.63[a]	1.97 ± 0.01	2.024[c]
O^+	2.58 ± 0.02	2.57[a]	0	0
Ne^+	1.32 ± 0.01	1.27[a]	1.122 ± 0.001	1.283[c]

[a] Hibbert *et al* (1977).
[b] Shorer (1982).
[c] Sen (1979) actually $2p^q$ 3s.

We thank A Dalgarno for useful correspondence. This work was supported by Air Force Contract No F19628-81-K-0007.

References

Bethe H A and Salpeter E E 1957 *Quantum Mechanics of One and Two Electron Atoms* (New York: Academic)

Chang E S and Sakai H 1981 *J. Phys. B: At. Mol. Phys.* **14** L391–5

—— 1982 to be published

Deutsch C 1970 *Phys. Rev. A* **2** 43–8

Edlén B 1964 *Encyclopedia of Physics* vol 27 (Heidelberg: Springer)

Eriksson K B S 1956 *Phys. Rev.* **102** 102–4

—— 1967 *Ark. Fys.* **35** 225–8

Eriksson K B S and Johansson I 1961 *Ark. Fys.* **19** 235–47

Fano U and Racah G 1959 *Irreducible Tensorial Sets* (New York: Academic)

Hibbert A, Vo Ky Lan and LeDourneuf M 1977 *J. Phys. B: At. Mol. Phys.* **10** 1015–25

Humphreys C J, Paul E, Cowan R D and Andrew K L 1967 *J. Opt. Soc. Am.* **57** 855–64

Johansson L 1965 *Ark. Fys.* **31** 201–34

Litzen U 1968 *Ark. Fys.* **38** 317–24

McConkey J W, Burns D J and Kernahan J A 1968 *J. Quant. Spectrosc. Radiat. Transfer* **8** 823–8

Moore C 1976 *NBS Tables of Atomic Spectra* NSRDS-NBS 3, §7 (Washington, DC: US Govt Printing Office)

Ölme A 1969 *Ark. Fys.* **40** 35–47

Sen K D 1979 *Phys. Rev.* **20** 2276–7

Shorer D L 1982 private communication, courtesy of A Dalgarno

Slater J C 1960 *Quantum Theory of Atomic Structure* (New York: McGraw-Hill)

PHYSICAL REVIEW A VOLUME 27, NUMBER 2 FEBRUARY 1983

Theory of angular distributions of electrons resonantly scattered by molecules. III. The broad resonance in N_2 and Co at 20 eV

Edward S. Chang
Department of Physics and Astronomy, University of Massachusetts, Amherst, Massachusetts 01003
(Received 30 June 1982)

Theoretical expressions for the vibrational excitation differential cross section (DCS) are given for the $^2\Sigma_u^+$ and the $^2\Sigma^+$ resonances. They fit some recent data on N_2 and CO, respectively, at an electron impact energy of about 20 eV. These fits allow us to obtain individual rotational-vibrational DCS's. It is demonstrated that the discrepancy between the DCS data from different experiments is due to varying energy resolution resulting in selective partial exclusion of some rotational branches. Further, theoretical DCS's for each rotational branch in both gases are found, which are verifiable with the new experimental technique used to separate out the rotational branches at 2 eV.

It is well known that resonances enhance the vibrational excitation cross sections of molecules by electron impact.[1] In such instances, the angular distribution of the scattering electron or the differential cross section (DCS) can often be predicted without an *ab initio* calculation. Such a theory was given in an earlier paper[2] referred to as I, and an application to CO at 1.8 eV was discussed[3] in II. In the present work, we apply the theory developed in I to the vibrational and rotational excitation of N_2 and CO at about 20 eV.

The enhancement of the vibrational cross section in N_2 was first observed by Pavlovic *et al.*,[4] who placed the position of the resonance at 22 eV with a width of 3 to 4 eV. Calculations based on the multiple scattering model by Dehmer *et al.*[5] show a $^2\Sigma_u^+$ resonance in the 15- to 35-eV range. They recognized that the identification was not complete until the DCS was calculated but were discouraged by the strong dependence of the observed DCS with energy in the resonance region, refuting the postulate of a single resonance.[4] Fortunately, more recent measurements of the vibrational DCS in CO as well as in N_2 by Tanaka[6,7] and his collaborators, and in both gases by Tronc *et al.*,[8] showed little variation with energy. These data enable us to fit theoretical angular distributions obtained by an extension of I. Thus we are able to reject other possible resonances such as $f\pi$, $f\delta$, and $f\phi$, while confirming the $f\sigma$ resonance in both N_2 and CO. However, the best fit with experiment is achieved only when the $^2\Sigma_u^+$ resonance in N_2 admits some p component, and $^2\Sigma^+$ resonance in CO some d component.

Further, the same theory yields the individual rotational-vibrational DCS's for the $^2\Sigma_u^+$ and the $^2\Sigma^+$ resonance. It can be seen that the theoretical DCS's for the higher rotational branches are very different from the (elastic) Q branch. Therefore their exclusion through higher energy resolution, e.g., 30 meV, will result in serious distortion of the measured vibrational DCS. In particular, this effect appears to account for the very different DCS of Pavlovic *et al.*[4] from the other two experimental groups. Independently, the theoretical rotational-vibrational DCS can be directly verified with the new experimental technique of Jung *et al.*,[9] as their 2-eV data has confirmed the theory of the $^2\Pi$ resonance discussed in II.

In I, we have derived an expression for the angular distribution of electrons scattered from a Σ-state molecule. It is written as a sum over the angular momentum transfer j_t of a certain Clebsch-Gordan coefficient squared multiplied by a standard angular function, both found in Table I of I. Assuming the resonance to be of symmetry Λ, the appropriate column in the block $l=3$ is multiplied by the angular functions in the same row and then added up for all contributing values of the angular momentum transfer, $j_t=0$, 2, 4, and 6. Then the following DCS's are obtained:

for $f\sigma(\Lambda=0)$,

$$\frac{d\sigma}{d\Omega}=0.713(1+5.69\cos^2\theta-17.7\cos^4\theta+14.3\cos^6\theta), \tag{1a}$$

for $f\pi(\Lambda=1)$,

$$\frac{d\sigma}{d\Omega}=0.201(1+18.2\cos^2\theta-52.1\cos^4\theta+40.9\cos^6\theta), \tag{1b}$$

 ©1983 The American Physical Society

The U.S. Government is authorized to reproduce and sell this report. Permission for further reproduction by others must be obtained from the copyright owner.

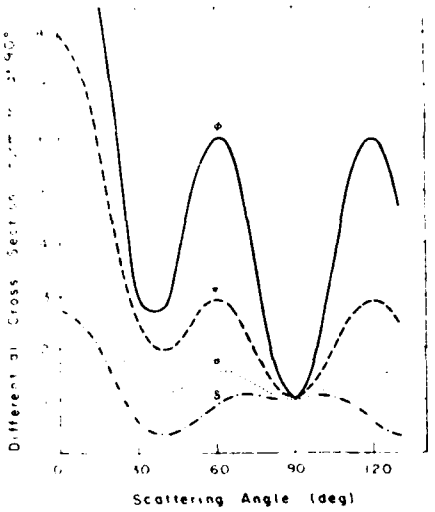

FIG. 1. Theoretical angular distributions for f-wave electrons assuming the symmetry for the molecular resonant states.

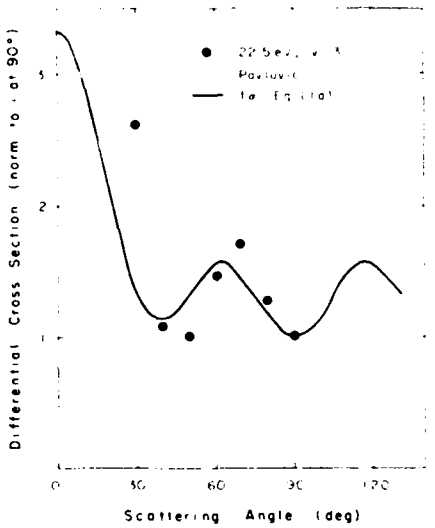

FIG. 2. Experimental angular distribution for electrons having excited the $v=3$ state in N_2, compared with simplified theory.

for $f\delta(\Lambda=2)$,

$$\frac{d\sigma}{d\Omega}=0.534(1+2.41\cos^2\theta-13.6\cos^4\theta+12.9\cos^6\theta), \tag{1c}$$

for $f\phi(\Lambda=3)$,

$$\frac{d\sigma}{d\Omega}=0.119(1+47.3\cos^2\theta-134\cos^4\theta+99.9\cos^6\theta). \tag{1d}$$

In Fig. 1, these four curves are plotted for $\theta=0°$ to 130°. It can be seen that they are distinctly different from each other. Generally speaking, the two curves $f\pi$ and $f\phi$ are too high at 60° and the curve of $f\delta$ it too low at 40° to fit the experimental data on N_2 and CO at about 20 eV (see Figs. 2, 3, and 5). However, the $f\sigma$ curve fits some data very well. A remarkable fit shown in Fig. 2 is the N_2 data of Pavlovic *et al.*[4] for $v'=3$ at 22.5 eV. It should be pointed out that the fit may be very poor at other energies. Fortunately, such variation with energy is contradicted by the more recent measurements of Tanaka *et al.*[7] and of Tronc *et al.*[8] To compare with their data in detail, we need a more general expression for the $^2\Sigma_u^+$ resonance than just from the f wave.

We now derive the general DCS for a $^2\Sigma_u^+$ resonance in a homonuclear molecule. In principle, higher partial waves, e.g., $l=5,7,\ldots$ may also contribute to the resonance, but here they can be excluded from consideration of the large centrifugal barrier, as $l=4,6,\ldots$ were excluded from the $^2\Pi_g$ resonance at a lower energy. Then the *ungerade* symmetry requirement leaves us with just the p wave ($l=1$) as well as the f wave ($l=3$). This admixture of two partial waves in a resonance can be described by a single parameter, called the mixing parameter $\tan\beta$. In fact, precisely this situation arose in II of this series.[10] We find

$$\frac{d\sigma}{d\Omega}(v'\leftarrow v)=\pi\sigma_{v'v}\sum_{j_t}[(1+\cos2\beta)^2(10,j_t0\,|\,10)^2\Theta(j_t,1111\theta)+(1-\cos2\beta)^2(30,j_t0\,|\,30)^2\Theta(j_t,3333\theta)+2\sin^22\beta(30,j_t0\,|\,10)^2\Theta(j_t,1133\theta)]. \tag{2}$$

In Eq. (2), $\sigma_{v'v}$ is the integrated vibrational excitation cross section which may be regarded as a normalization constant here. The summation over the angular momentum transfer j_t is restricted to even values by the Clebsch-Gordan coefficients $(j_1m_1,j_2,m_2\,|\,j_3m_3)$ and the parity favoredness ($\Sigma^+\rightarrow\Sigma^+$) of the transition. The angular function Θ is again given in Table I of I. Applying the usual procedure of evaluating the DCS to Eq. (2), we obtain

$$\frac{d\sigma}{d\Omega}(v'\leftarrow v)=\sigma_{v'v}[\,0.15(1+\cos2\beta)^2(1+2\cos^2\theta)$$

$$+0.178(1-\cos2\beta)^2(1+5.69\cos^2\theta-17.7\cos^4\theta+14.3\cos^6\theta)$$

$$+0.183(2\sin^2 2\beta)(1+1.09\cos^2\theta)]\,. \tag{3}$$

The first term in Eq. (3) [as in Eq. (2)] represents the pure $p\sigma$ wave. The second term is due to the $f\sigma$ wave and therefore is identical to Eq. (1a). Finally, the last term is the usual interference term. Over the width of the resonance, β is expected to vary only slowly with the incident energy E. In principle, β can be obtained from an *ab initio* calculation. Here we choose to regard it as a parameter, obtained by fitting Eq. (3) to the experimental DCS.

The available vibrational excitation data ($v=0\rightarrow1$) in N_2 consist of the results of Tanaka *et al.*[7] at 18, 20, 22.5, and 25 eV, and of Tronc *et al.*[8] at 18, 22.5, and 25 eV. All the DCS's show a forward peak, a minimum at 90°, and some flattening at 50°. However, they differ in detail by as much as 50% even at the same energy. The error bars given by Tronc[8] in Fig. 3 at 18 eV indicate their estimate of the relative error is ±8%, while their absolute error is stated as 30%. In the work of Tanaka *et al.* the estimated relative maximum error was given as 25%. Thus the data often lie outside of each other's error bars if they are all normalized to unity at 90°. In any event, the scatter in the experimental DCS appears to be too large for fitting Eq. (3) to determine the mixing parameter, in contrast to the 1.8-eV resonance data in CO discussed in II. Instead, we try to find a value of β in Eq. (3) which will produce a theoretical angular distribution which possesses all the consistent features of the experimental DCS described above.

In Fig. 3 we show a curve (solid line) obtained from Eq. (3) with $\cos2\beta=-0.5$, i.e., $\beta=60°$ or the mixing parameter $\tan\beta=1.73$. Explicitly, the DCS is then given by

$$\frac{d\sigma}{d\Omega}=0.71\sigma_{01}(\,1+4.02\cos^2\theta-10.1\cos^4\theta$$

$$+8.05\cos^6\theta)\,. \tag{4}$$

Note that it displays a forward peak, a flattening at 50°, and a dip at 90°. (Symmetry about 90° is required by theory as shown in II.) For comparison, only some experimental DCS's are shown, selected on the basis of larger integrated cross sections and/or more angular positions. They are normalized to theory, Eq. (4), at 50°. In Fig. 3, the experimental DCS's are now seen to be reasonably consistent with each other and with theory. Thus the experimental DCS's of Tronc *et al.* and Tanaka *et al.* from 18 to 22.5 eV for vibrational excitation in N_2 consistently exhibit the shape of a $^2\Sigma_u^+$ resonance with the ratio of f- to p-wave amplitude equaling

$$\frac{(1+0.5)}{(1-0.5)}=3\,.$$

Nevertheless, the sharp disagreement with the data of Pavlovic *et al.* remains to be explained. We will show how high resolution discriminates against some rotational components and leads to different measured DCS's from those with lower resolution.

So far, we have neglected the rotational structure of the molecules. At first sight that seems entirely appropriate since the rotational constant of N_2 is $B=0.25$ meV, while the energy resolutions are quoted as 50 meV in the works of Tronc *et al.* and Tanaka *et al.*, and 30 meV in Pavlovic *et al.* However, the predominantly f resonance implies sizable rotational excitation cross sections of the type $\Delta j=\pm4,\pm6$ as well as $\Delta j=\pm2$, and the pure elastic

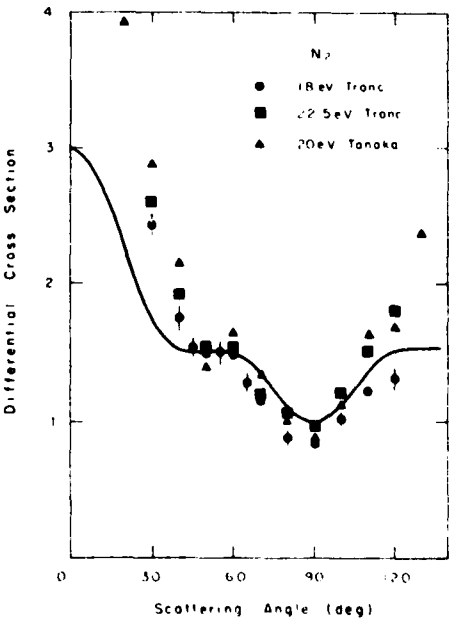

FIG. 3. Theoretical and experimental angular distribution for electrons having excited the $v=1$ state in N_2 (arbitrary units).

Δj 0. In general, the additional energy loss due to a rotational branch Δj is

$$[2j\Delta j + (\Delta j)^2 + \Delta j]B \ .$$

At room temperature, $j=10$ is a typical rotational state with significant population; for this state, the energy losses for $\Delta j=4$ and $\Delta j=6$ are 25 and 40 meV, respectively. Now we see that the DCS of Pavlovic *et al.* essentially excludes rotational excitation of the type $\Delta j=6$, and partially those with $\Delta j=4$, while those of Tronc *et al.* and Tanaka *et al.* partially exclude those with $\Delta j=6$.

To scrutinize this issue of rotational excitation in addition to vibrational excitation, we need the rotational-vibrational DCS. With suitable modifications for the $^2\Sigma_u^+$ resonance, Eq. (2) of I becomes

$$\begin{aligned}\frac{d\sigma}{d\Omega}(j'v'\leftarrow jv) = \pi\sigma_{v'v}\sum_{j_t}(j0,j_t0\mid j'0)^2[&(1+\cos2\beta)^2(10,j_t0\mid 10)^2\Theta(j_t,1111\theta)\\ &+(1-\cos2\beta)^2(30,j_t0\mid 30)^2\Theta(j_t,3333\theta)\\ &+2\sin^2 2\beta(10,j_t0\mid 10)(30,j_t0\mid 30)\Theta(j_t,1313\theta)\\ &+2\sin^2 2\beta(30,j_t0\mid 10)^2\Theta(j_t,1133\theta)\\ &-2\sin^2 2\beta(10,j_t0\mid 30)(30,j_t0\mid 10)\Theta(j_t,1331\theta)] \ . \end{aligned} \tag{5}$$

Accepting the value of -0.5 for $\cos2\beta$ found earlier, we can now calculate each individual rotational-vibrational cross section in N_2 for all significantly populated levels in N_2 at the molecular beam temperature. For example, the Ehrhardt group[9] measured their temperature to be 500 ± 30 K. Rather then calculating all 26 or so DCS's for each populated rotational state and averaging the population, we calculate the DCS for each rotational branch for the median rotational level. For N_2 at 500 K, the median level is $j=10$ (population 8.56%) with the population of $j=0$ to 9 totaling 42.9%, and the population of $j=11$ to ∞ totaling 48.5%. We use the high-j approximation developed elsewhere,[11] which in effect neglects terms of order j^{-2} in comparison with unity. Therefore it is accurate to about 1%. The DCS for each rotational branch is then given by

$$\begin{aligned}\frac{d\sigma}{d\Omega}(\Delta j=0) = \tfrac{1}{4}\sigma_{v'v}[&(1+\cos2\beta)^2(0.15+1.05\cos^2\theta)\\ &+(1-\cos2\beta)^2(0.09+2.74\cos^2\theta-8.82\cos^4\theta+7.19\cos^6\theta)\\ &+2\sin^2 2\beta(0.87-0.58\cos^2\theta+1.61\cos^4\theta)] \ , \end{aligned} \tag{6a}$$

$$\begin{aligned}\frac{d\sigma}{d\Omega}(\Delta j=\pm2) = \tfrac{1}{4}\sigma_{v'v}\left(1\pm\frac{1}{j}\right)[&(1+\cos2\beta)^2(0.23+0.08\cos^2\theta)\\ &+(1-\cos2\beta)^2(0.10+0.77\cos^2\theta-1.99\cos^4\theta+1.38\cos^6\theta)\\ &+2\sin^2\beta(0.14+0.50\cos^2\theta-0.31\cos^4\theta)] \ , \end{aligned} \tag{6b}$$

$$\begin{aligned}\frac{d\sigma}{d\Omega}(\Delta j=\pm4) = \tfrac{1}{4}\sigma_{v'v}\left(1\pm\frac{2}{j}\right)[&(1-\cos2\beta)^2(0.13-0.17\cos^2\theta+0.06\cos^4\theta+0.13\cos^6\theta)\\ &+2\sin^2 2\beta(0.23-0.20\cos^2\theta-0.03\cos^4\theta)] \ , \end{aligned} \tag{6c}$$

and

$$\frac{d\sigma}{d\Omega}(\Delta j=\pm 6)=\frac{1}{4}\sigma_{v'v}\left[1\pm\frac{3}{j}\right](1-\cos 2\beta)^2(0.73+0.55\cos^2\theta-0.28\cos^4\theta+0.02\cos^6\theta)/10\ . \tag{6d}$$

The results of Eq. (6) may be directly verified when the Ehrhardt group[9] reruns their experiment and meticulous analysis at an energy of 20 eV.

For the moment, we only want to explore the effect on the measured vibrational DCS when some rotational branches are inadvertently excluded through achieving higher resolution. In this respect, the most important branch is the $\Delta j=+6$ located at an energy loss of 40 meV with a relative cross section

$$\sigma(\Delta j=6)/\sigma_{\text{sum}}$$

of 10%. The next important branch is the $\Delta j=+4$ located at 25 meV with a relative cross section of about 11%. For convenience their DCS, given, respectively, by Eqs. (6c) and (6d), are shown in Fig. 4. Since they comprise only large angular momentum transfer j_t in Eq. (5), they are nearly isotropic, as classically, electrons undergoing large change in angular momentum can be expected to "forget" their incident direction. Relatively unimportant are the corresponding superelastic branches with the same DCS, $\Delta j=-6$ and -4, located at -19 and -15 meV with relative cross sections of 4 and 5%, respectively. It is apparent that with improving resolution more of these near isotropic DCS's will be excluded in the measurement. Hence the experimental DCS will tend to be too high in the forward direction as is the case in the data shown in Figs. 2 and 3. Further, if the experimental resolution is varied with the scattering angle, the measured DCS can take on an unexpected shape. Such appeared to be the case in the work of Pavlovic *et al.*[4] when the angle was fixed, and the incident energy was varied in the measurement. The best energy resolution achieved was 30 meV at some angle, but at other angles the resolution might have been lower. In contrast, Tanaka *et al.*[7] fixed the energy while varying the angle, as did Tronc *et al.*[8] In both latter experiments, the resolution was 50 meV, which appeared low enough to include most of the $\Delta j=+6$ rotational branch. Therefore the measured DCS of Pavlovic *et al.* can be expected to be quite different from the latter two experimental groups and from theory.

Next, we turn our attention to the equivalent resonance in CO. DCS's have been measured by Tronc *et al.*[8] at 16, 19.5, and 23 eV, and by Chutjian and Tanaka[6] at 20 eV. Figure 5 shows that these DCS's are all quite consistent with each other and fit the theoretical $f\sigma$ expression (dashed line) given in Eq. (1a) quite well. Once more we can conclude that e-CO vibrational excitation is dominated by a $^2\Sigma^+$ resonance at about 20 eV with a width of at least 3.5 eV. In principle, a $^2\Sigma^+$ resonance may contain $s(l=0)$, $p(l=1)$, $d(l=2)$ as well as $f(l=3)$ components. However, it can be argued that only the d component needs to be considered as only it is dipolarly coupled to the dominant f component.

Then the DCS for the vibrational excitation of CO is essentially the same as for N_2 given in Eq. (2), except for the replacement of the p wave by the d wave. For the sake of completeness, it is given below:

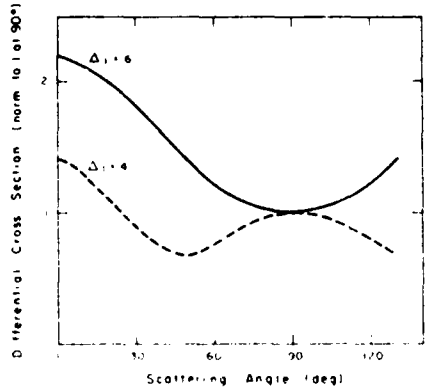

FIG. 4. Theoretical angular distributions for f-wave electrons with the selection of specific rotational branches.

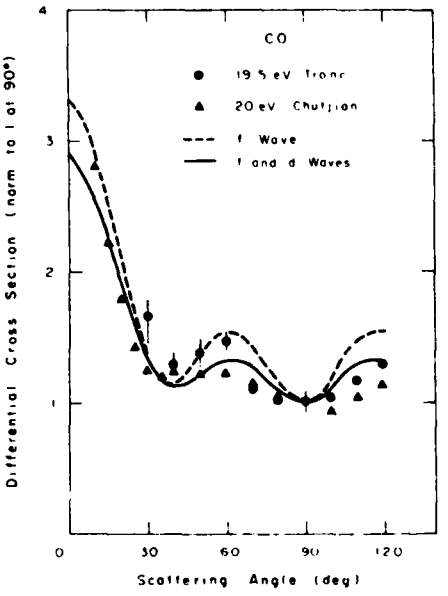

FIG. 5. Theoretical and experimental angular distributions for electrons having excited the $v'=1$ state in CO.

$$\frac{d\sigma}{d\Omega}(v'\leftarrow v)=\pi\sigma_{v'v}\sum_{j_t}[\,(1+\cos2\beta)^2(20,j_t0\,|\,20)^2\Theta(j_t,2222\theta)$$
$$+(1-\cos2\beta)^2(30,j_t0\,|\,30)^2\Theta(j_t,3333\theta)$$
$$+2\sin^22\beta(30,j_t0\,|\,20)^2\Theta(j_t,2233\theta)\,]\,. \tag{7}$$

In comparison with Eq. (1a), a better fit with all data is obtained with $\cos2\beta=-0.75$ in Eq. (8), i.e.,

$$\frac{d\sigma}{d\Omega}(v'\leftarrow v)=\sigma_{v'v}(0.78)(1+3.59\cos^2\theta-11.7\cos^4\theta+9.98\cos^6\theta)\,, \tag{8}$$

as shown in Fig. 5. Nevertheless, significant discrepancy between the DCS's of Tronc *et al.* (at 19.5 eV) and Chutjian and Tanaka up to 20% at 20 eV prevents us from obtaining a value for $\cos2\beta$ more accurate than -0.75 ± 0.25. Thus the $^2\Sigma^+$ resonance in CO is also dominated by the f wave as in the case of the $^2\Sigma_u^+$ resonance in N_2. However, the admixture is lower in this case with the d-wave amplitude ratio to the f wave given by

$$\frac{(1-0.75)}{(1+0.75)}=\frac{0.25}{1.75}=\frac{1}{7}\,.$$

In anticipation of the measurement of the rotational-vibrational DCS in CO at 20 eV by the Ehrhardt group, we present the individual differential cross section below. The general expression from the initial state (j,v) to the final state (j',v') is given by

$$\frac{d\sigma}{d\Omega}(j'v'\leftarrow jv)=\pi\sigma_{v'v}\sum_{j_t}(j0,j_t0\,|\,j'0)^2$$
$$\times[\,(1+\cos2\beta)^2(20,j_t0\,|\,20)^2\Theta(j_t,2222\theta)$$
$$+(1-\cos2\beta)^2(30,j_t0\,|\,30)^2\Theta(j_t,3333\theta)$$
$$+2\sin^22\beta(20,j_t0\,|\,20)(30,j_t0\,|\,30)\Theta(j_t,2323\theta)$$
$$+2\sin^22\beta(30,j_t0\,|\,20)^2\Theta(j_t,2233\theta)$$
$$-2\sin^22\beta(20,j_t0\,|\,30)(30,j_t0\,|\,20)\Theta(j_t,2332\theta)\,]\,. \tag{9}$$

In practice, as in the case of N_2, only the rotational branches can be separated out. With the same high-j approximation, the DCS for each branch is found to be

$$\frac{d\sigma}{d\Omega}(\Delta j=0)=\tfrac{1}{4}\sigma_{v'v}[\,(1+\cos2\beta)^2(0.41-1.69\cos^2\theta+2.49\cos^4\theta)$$
$$+(1-\cos2\beta)^2(0.10+2.73\cos^2\theta-8.81\cos^4\theta+7.20\cos^6\theta)$$
$$+2\sin^22\beta(9.34\cos\theta-2.75\cos^3\theta+4.48\cos^5\theta)\,]\,, \tag{10a}$$

$$\frac{d\sigma}{d\Omega}(\Delta j=\pm1)=\tfrac{1}{4}\sigma_{v'v}\left[1\pm\frac{1}{2j}\right](2\sin^22\beta)(\,0.20-0.54\cos\theta-0.38\cos^2\theta+2.62\cos^3\theta$$
$$+0.67\cos^4\theta-2.57\cos^5\theta)\,, \tag{10b}$$

$$\frac{d\sigma}{d\Omega}(\Delta j=\pm 2)=\tfrac{1}{4}\sigma_{v'v}\left|1\pm\frac{2}{2j}\right|[(1+\cos 2\beta)^2(0.22-0.30\cos^2\theta+0.35\cos^4\theta)$$
$$+(1-\cos 2\beta)^2(0.10+0.77\cos^2\theta-1.99\cos^4\theta+1.38\cos^6\theta)$$
$$+2\sin^2 2\beta(-0.08\cos\theta+1.11\cos^3\theta+1.08\cos^5\theta)], \tag{10c}$$

$$\frac{d\sigma}{d\Omega}(\Delta j=\pm 3)=\tfrac{1}{4}\sigma_{v'v}\left|1\pm\frac{3}{2j}\right|(2\sin^2 2\beta)(0.18-0.12\cos\theta-0.30\cos^2\theta+0.19\cos^3\theta$$
$$+0.32\cos^4\theta-0.28\cos^5\theta), \tag{10d}$$

$$\frac{d\sigma}{d\Omega}(\Delta j=\pm 4)=\tfrac{1}{4}\sigma_{v'v}\left|1\pm\frac{4}{2j}\right|[(1+\cos^2\beta)^2(0.11+0.08\cos^2\theta+0.01\cos^4\theta)$$
$$+(1-\cos 2\beta)^2(0.14-0.17\cos^2\theta+0.07\cos^4\theta+0.13\cos^6\theta)$$
$$+2\sin^2 2\beta(-0.02\cos\theta+0.11\cos^3\theta-0.04\cos^5\theta)], \tag{10e}$$

$$\frac{d\sigma}{d\Omega}(\Delta j=\pm 5)=\tfrac{1}{4}\sigma_{v'v}\left|1\pm\frac{5}{2j}\right|(2\sin^2 2\beta)(0.91-1.16\cos\theta+0.66\cos^2\theta-0.28\cos^3\theta$$
$$+0.20\cos^4\theta-0.33\cos^5\theta)/10, \tag{10f}$$

and

$$\frac{d\sigma}{d\Omega}(\Delta j=\pm 6)=\tfrac{1}{4}\sigma_{v'v}\left|1\pm\frac{6}{2j}\right|(1-\cos 2\beta)^2(0.73+0.55\cos^2\theta+0.28\cos^4\theta+0.02\cos^6\theta)/10. \tag{10g}$$

For the purpose of comparison with the anticipated data of the Ehrhardt group, the initial rotational state j should be taken to be the *median* level at the molecular beam temperature. At 500 K in the Jung *et al.*[9] experiment, two levels tie as the median $j=10$ and 11 with a relative population of 6.35 and 6.15%, respectively. (The sum from $j=0$ to 9 is 42.8%, and the sum from $j=12$ to ∞ is 44.7%.)

In conclusion, we have applied a previous theory to elucidate the DCS of an f resonance in electron scattering from a diatomic molecule. The 20-eV resonances in N_2 and CO are both confirmed to be of $^2\Sigma^+$ in symmetry with a dominant f component. Present in the former is a p component with a relative amplitude of 0.33, and in the latter a d component with a relative amplitude of 0.14.

Through analysis of the rotational branches, we have shown that spurious DCS's may be obtained through too *high* an energy resolution. Even a modest resolution of 30 meV used by Pavlovic *et al.*[4] will exclude some rotational branches, resulting in a distorted vibrational DCS.

Finally, we have presented the DCS's of all the rotational branches in the vibrational excitation of N_2 and CO in the $^2\Sigma^+$ resonance region of about 16–25 eV. They await direct confirmation by the new experimental technique developed by the Ehrhardt group.

The author thanks H. Sakai for useful discussions. Helpful correspondence with H. Tanaka, M. Tronc, and H. Ehrhardt are gratefully received. This work was supported by Air Force Contract No. F19628-81-K-0007.

[1]G. J. Schulz, Rev. Mod. Phys. 45, 423 (1973).
[2]E. S. Chang, Phys. Rev. A 16, 1841 (1977).
[3]E. S. Chang, Phys. Rev. A 16, 1850 (1977).
[4]Z. Pavlovic, M. J. W. Boness, A. Herzenberg, and G. Schulz, Phys. Rev. A 6, 676 (1972).
[5]J. L. Dehmer, J. Siegel, J. Welch, and D. Dill, Phys. Rev. A 21, 101 (1980).
[6]A. Chutjian and H. Tanaka, J. Phys. B 13, 1901 (1980).
[7]H. Tanaka, T. Yamamoto, and T. Okada, J. Phys. B 14, 2081 (1981).
[8]M. Tronc, R. Azria, and Y. LeCoat, J. Phys. B 13, 2327 (1980); M. Tronc has informed that their error bars may have been underestimated.
[9]K. Jung, Th. Antoni, R. Müller, K. H. Kochem, and H. Ehrhardt J. Phys. B 15, 3535 (1982).
[10]In paper II, the factor (4π) should be deleted from Eqs. (2), (5), (6), (7), (8), (9), (10), and (11); and in paper I, footnote 17, is in error; it should read

$$\int \Theta(jt;l_0l_0'll'\theta)\sin\theta\, d\theta\, d\theta\, d\phi$$
$$=(-1)^{l_0-l_0'}(2j_t+1)(jt^0,l_0'0\,|\,l'0)(jt\,0,l_00\,|\,l0)\,.$$

[11]E. S. Chang J. Phys. B 15, L873 (1982).

The U.S. Government is authorized to reproduce and sell this report.
Permission for further reproduction by others must be obtained from
the copyright owner.

Reprinted from SPIE Vol 366– Modern Utilization of Infrared Technology VIII
© 1983 by the Society of Photo Optical Instrumentation Engineers, Box 10, Bellingham, WA 98227-0010 USA

Atmospheric infrared emission observed at altitude of 27000 to 28000 m

Hajime Sakai
Department of Physics and Astronomy, University of Massachusetts
Amherst, Massachusetts 01003

George Vanasse
Optical Physics Division, Air Force Geophysics Laboratory
Hanscom AFB, Massachusetts 01731

Abstract

The molecules in the lower part of atmosphere are in thermal equilibrium with the local surrounding. The infrared emission resulted by their thermal excitation can be studied to determine their temperature and concentration profile in the atmosphere. We used a cryogenically cooled Fourier spectrometer mounted on a balloon-borne platform to study the infrared emission spectrum of atmosphere for this purpose. The experiment, which took place on October 7, 1981, at Holloman AFB, produced the analyzable data for more than two hours at altitude of 27000 ∿ 28000 m along the horizontal and the vertical line of sight. The spectral data extended from 550 cm^{-1} to 1000 cm^{-1} covering the CO_2 15μ bands ($\Delta v_2 = 1$) with a resolution of 0.2 cm^{-1}. The data were found interesting on two accounts: (1) a continuum background feature was superimposed with the molecular emission feature; (2) the radiance level of the CO_2 15μ bands observed along the horizontal line of sight varied by a much greater degree than expected.

Introduction

The infrared radiative transfer characteristics in the atmosphere[1] are principally controlled by two parameters, the local abundance of the molecules responsible for the emission or the absorption process, and the local temperature. The third parameter, the local pressure, plays a secondary importance to the problem. In the lower part of atmosphere including the stratosphere, the molecules are generally in thermal equilibrium with the local surrounding. The radiative transfer characteristics under the local thermal equilibrium condition could be solved in a straightforward calculation, if those parameters are known.[2] In the stratosphere, some of these parameters are poorly known at present because of experimental difficulties. We designed an experiment to collect the infrared radiative transfer data in the stratosphere by observing the infrared emission along the horizontal line of sight. A cryogenically cooled Fourier interferometer spectrometer mounted on a balloon-borne platform was used for the experiment.[3] The balloon flight took place on October 7, 1981, at Holloman AFB, New Mexico, and obtained the spectral data taken at the balloon ceiling altitude of ∿ 28500 m for more than two hours.[4] The instrumentation part of our experiment is detailed in another paper presented at this meeting.[5] In this paper, our discussion will be focused on the spectral data obtained.

In the past, the spectral study of the atmosphere was done either with the absorption scheme using the sun as its infrared source,[6] or with the satellite-borne spectrometer looking down toward the earth's surface.[7] The absorption scheme ties its path on the sun's position. The path for an adequate absorption required in the quantitative study of stratosphere must be long, because few molecules are available there. The measurement is then limited to a short period during sunrise or sunset. The molecules suspected of the diurnal concentration variation cannot be studied well if their observation requires a long absorption path. The satellite-borne experiment measures a cumulative effect of the absorption or the emission along the path. It requires an elaborate analysis scheme if the radiative transfer characteristics of a thin atmospheric layer is sought. The scheme that we adopted observes the atmospheric emission along the horizontal line of sight independent of the solar position. The radiative transfer characteristic of a thin atmospheric layer is more readily available in our measurement scheme. The observation extended a long period of time over the entire balloon flight, since the line of sight for observation did not tie into the solar position. The radiance level was very low. At the maximum, it would correspond to the blackbody radiance at the stratosphere local temperature of 220° ∿ 230°K. The sensitivity of measurement was a critical issue in our experiment and it is fully discussed in our other paper.

Balloon flight

The flight profile, given in terms of the balloon altitude as a function of time, was monitored using radar on the ground. It is shown in Fig. 1 with the local temperature measured with a thermistor bolometer hung below the gondola. The measured value of the total radiance level is also shown in the figure. Even though the laser signal failure

which occurred during some part of the flight resulted in some loss of the data, the interferometer produced the analyzable data for more than two hours at the maximum balloon altitude. The spectral data obtained during the flight consisted of three parts: (1) the data along the horizontal line of sight; (2) the data along the vertical line of sight; and (3) the radiance calibration spectra obtained using an on-board blackbody source which was presumably in thermal equilibrium with the ambient. As seen in the thermistor bolometer data, the ambient temperature at the altitude of 28000 m ∿ 28500 m fluctuated between 270°K and 250°K, closely correlating with the balloon motion. The data indicated that the stratospheric ambient temperature measured with the on-board thermistor was considerably higher than that of the model atmosphere, and that its fluctuation was unexpectedly large.

Our balloon flight was accompanied by two radio-sonde flights. The temperature measured by the radio-sonde sensor was at most 230°K, as seen in Fig. 2, at this altitude range, much lower than the temperature measured with the on-board thermistor. Even if a rapid motion of the radio-sonde balloon was accounted for, the discrepancy among those three temperature readings defied a single explanation. This puzzle remains unsolved at present. Both data showed the temperature fluctuation of approximately 10°K at the altitude of 28000 m. The variation in the total radiance level measured along the horizontal line of sight was also found an unexpectedly large value of 50%. It was also found to be correlated with the measured temperature.

Calibration of the radiance level

Two sets of spectra were taken using the on-board blackbody source, one at 17:30 GMT and another between 18:45 and 19:30 GMT. Both sets were taken at the balloon ceiling altitude of ∿ 28000 m. Their spectral characteristics as well as their radiance levels were found very similar. We estimated these spectra to be those of a 255°K blackbody radiance, and proceeded to calibrate all the measured spectral data, horizontal-looking and down-looking, accordingly. The calibrated down-looking spectra showed the radiance level at the center of the CO_2 15μ band corresponding to 215°K ∿ 220°K and that of the window region to the ground temperature of 285°K. The radiance level obtained for the down-looking spectra was, therefore, consistent with the atmospheric radiative transfer expected for this spectral region.

The radiance level of the interferogram signal was estimated with respect to the noise level contained in it. Since the gain factor of the detector amplifier was not transmitted to the ground, it had to be determined from the recorded interferogram data. The noise level in the interferogram data increased or decreased whenever the detector amplifier switched its gain setting. Since we had no reason to believe that the absolute level of noise in the interferogram signal varied from time to time, we determined the gain of the detector amplifier using the noise level observed in the recorded interferogram signal. We observed the noise level stepped in accordance with the step in the amplifier gain setting. Therefore, our procedure for estimating the detector amplifier gain was self-consistent. The total radiance level received by the spectrometer was proportional to the central maximum modulation and it was estimated by multiplying the central maximum modulation with the gain factor which was determined from the noise level observed in the interferogram very far from the central maximum.

An exception to the procedure for the radiance calibration had to be observed for the data taken after 19:30 GMT, when the blackbody source was removed from the field of view at the last time in the flight. The radiance level determined using the procedure above showed a dramatic increase for the horizontal-looking spectra taken after 19:30 GMT, while the balloon altitude and the measured ambient temperature remained unchanged as before. At that time, the liquid helium level in the detector dewar became definitely low and the detector temperature started to rise. We reasoned that the apparent increase of the radiance level after 19:30 GMT, shown by a solid curve, was resulted by an improved noise figure of the detector, rather than by an increase in the incident radiance level. The radiance level probably remained at the same level as indicated by a dotted curve. Anyway, the data obtained after 19:30 GMT certainly had a larger degree of ambiguity than the rest because the radiance level calibration was not repeated after the observation of these spectra. The rest of our discussion will be made excluding the data collected after 19:30 GMT.

The sensitivity of our spectrometer was determined using the blackbody calibration spectrum. As described above, the calibration source was assumed at 255°K. The obtained blackbody spectrum and the determined radiance level given as a function of wavenumber are shown in Fig. 3. The obtained curves were used to determine a relative radiance level of the data at each wavenumber position. The absolute value of the radiance level was then determined by normalizing the integrated relative radiance value to the total radiance level obtained using the procedure described above.

CO_2 bands

The major atmospheric bands observable in our measurement are CO_2 ($\Delta v_2 = 1$) transitions. All bands have a strong Q branch. Table I lists the band center for the observable transitions. Of these, the Q branch of the (01101-00001) band of the 626 isotope should show a strong saturation even at our balloon altitude with an assumption that the CO_2 concentration in the stratosphere is given by the mixing ratio of 3.3×10^{-4}. Our observation along the horizontal line of sight was made at the elevation angle of 7.5°. With the CO_2 mixing ratio of 3.3×10^{-4} and the mid-latitude model atmosphere, we can expect the CO_2 column density to be approximately 5.0×10^{20} molecules/cm^2.

Table I. Major CO_2 Bands in the 700 cm^{-1} Region

Band	Isotope	Band Center
01101-00001	626	667.4 cm^{-1}
10001-01101	626	720.8
10002-01101	626	619.8
02201-01101	626	667.8
03301-02201	626	668.1
01101-00001	636	648.5
01101-00001	628	662.4

The down-looking data

The emission spectra observed along the vertical line of sight is presented in Fig. 4. All data observed along this direction varied very little among them in their spectral characteristics and their radiance level. As mentioned earlier, the source radiance level in the 675 cm^{-1} region was found to be $\sim 4.0 \times 10^{-6}$ W/cm^2 str cm^{-1}, the blackbody radiance level of 210° $\sim$ 220°K. The level in the 800 cm^{-1} region was 1.1×10^{-5} W/cm^2 str cm^{-1}, consistent with the concurrently measured ground temperature of 285°K. The theoretical spectrum calculated using the FASCOD1B code[2] with the AFGL atmospheric line parameters[8] is shown in Fig. 5. No significant differences were found between the observed and the calculated.

The horizontal-looking data

The data observed along the horizontal line of sight showed their spectral characteristics almost identical to each other. Their difference was noticed in the radiance level as demonstrated in the data of Figs. 6 and 7, which were taken at 18:15 and 18:45 GMT. Two distinctive features were found in these observed spectra: (1) a continuum feature which amounted to the radiance level of $2 \sim 3 \times 10^{-6}$ watt/cm^2 str cm^{-1} at the 600 cm^{-1} region, and (2) a large fluctuation in the observed radiance level.

A theoretical spectrum shown in Fig. 8 was generated for the emissivity of those CO_2 transitions observable in the spectral region. The calculation assumed that a column of 4×10^{20} CO_2 molecules/cm^2 was at a kinetic temperature of 230°K. If the temperature was different from 230°K by a small degree, the emissivity would have changed little. Thus the curve is a very convenient guide for estimating the radiance level. In the figure, a solid line representing a radiance level of 5×10^{-6} watt/cm^2 str cm^{-1} gives the scaling factor for 230°K. If the temperature is 210°K, the radiance level would have to be scaled by a dotted line which provides a radiance level of 4.0×10^{-6} watt/cm^2 str cm^{-1}. Our observation at altitude of 28000 m with the elevation angle of 7.5° should have yielded the CO_2 emission with its column density of 5×10^{20} molecules/cm^2. The Q branch of the (01101-00001, 626) band was expected to show a complete saturation (emissivity = 1) at its peak. The radiance level at this peak was found to be 3.7×10^{-6} watt/cm^2 str cm^{-1} for the spectrum of Fig. 7, and 3.0×10^{-6} watt/cm^2 str cm^{-1} for Fig. 6. The spectrum of Fig. 7 could be interpreted as the emission at 210°K. This interpretation ran into a difficulty because it produced no satisfactory explanation for the continuum feature. The radiance level of 3.0×10^{-6} watt/cm^2 str cm^{-1} compounded our difficulty in explaining these results.

The theoretical calculation obtained using the FASCOD1B code with the CO_2 column density of 1.2×10^{21} molecules/cm^2 at 220°K is shown in Fig. 9. Both theoretical results contained no indication of the continuum feature. We engaged in an extensive search for any experimental artifacts which could possibly produce a continuum feature, and found none. We are rather confident that the continuum feature seen in Figs. 6 and 7 is real and of atmospheric origin, even though we have no explanation for it at this moment.

The two unsolved mysteries are our principal discoveries of our latest balloon flight.

We are honing that future flights will bring some light onto the observed mysteries and that we will gain more insight into the stratosphere.

Acknowledgments

This work is supported by AFOSR under the atmospheric science project 2310 and performed as part of AFGL Task 2310G1. We acknowledge W. Gallery of AFGL who provided the theoretical spectra calculated using the FASCOD1B. ESD #82-615

References

1. Goody, R.M., Atmospheric Radiation I. Theoretical Basis, Oxford, London, 1964.
2. Clough, S.A. et al, "Atmospheric Spectral Transmittance and Radiance: FASCOD1B," SPIE Vol. 277, 152 (1981).
3. Sakai, H. et al, Proc. 1981 Int. Conf. on Fourier Transform Infrared Spectroscopy, SPIE Vol. 289, 196 (1981).
4. Vanasse, G.A., AFGL Report TR-81-0048 (1981); NTIS #AD/A 100 218.
Sakai, H. and Vanasse, G.A., AFGL Report TR-82-0150 (1982).
5. Sakai, H. et al, SPIE Conference 364 Proc., Vol. 364, Paper 364-06 (1982).
6. Goldman, A., Murcray, D.G., Murcray, F.J., and Niple, E., Appl. Opt. 19, 3721 (1980).
NASA Conference Publication 2134, "High Resolution Infrared Spectroscopy Technique for Upper Atmospheric Measurements," 1979.
7. Yates, H., Appl. Opt. 21, 203 (1982).
8. McClatchey, R.A. et al, "AFCRL Atmospheric Absorption Line Parameter Compilation," AFCRL Report TR-73-0096 (1973); NTIS #AD 762 904.
Rothman, L.S., Appl. Opt. 20, 791 (1981).
Rothman, L.S. et al, Appl. Opt. 20, 1323 (1981).

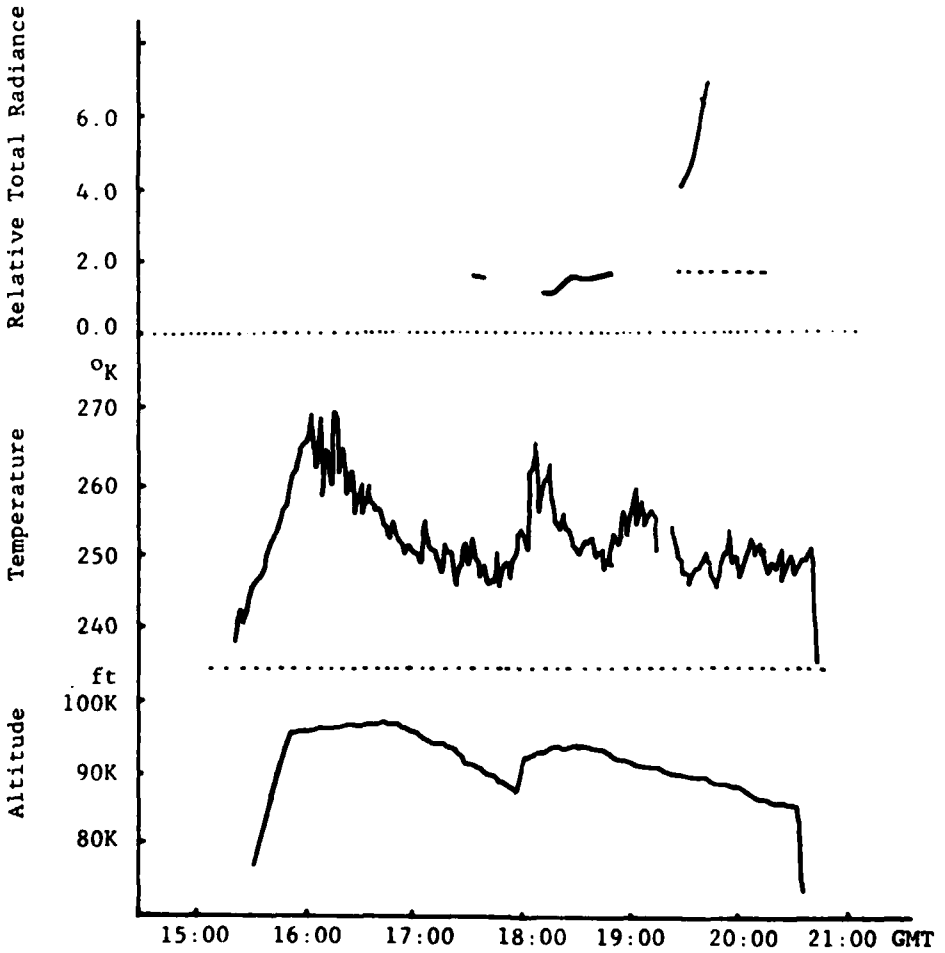

Figure 1. Flight Profile: Balloon Altitude, Ambient Temperature, and Observed Total Radiance.

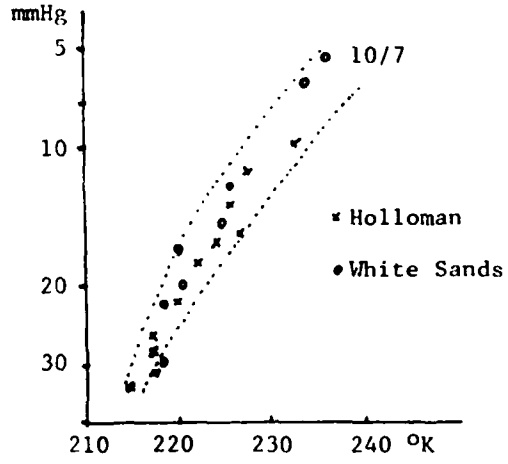

Figure 2. Temperature vs. Pressure Measured Using Radio-sonde.

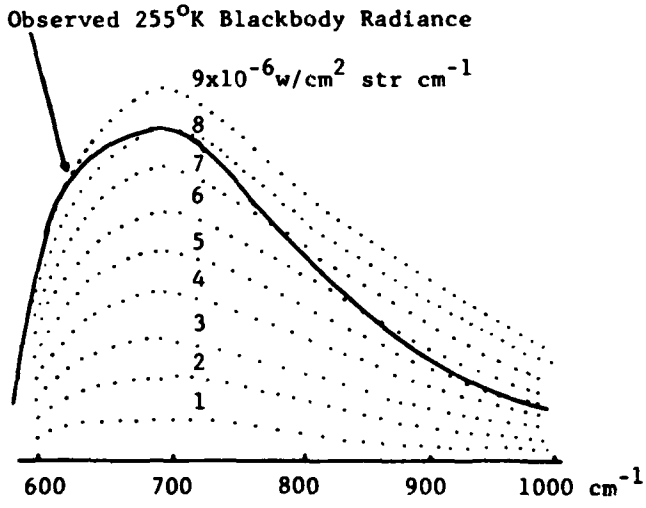

Figure 3. Observed Blackbody Radiance and Spectrometer Radiance Calibration Curves.

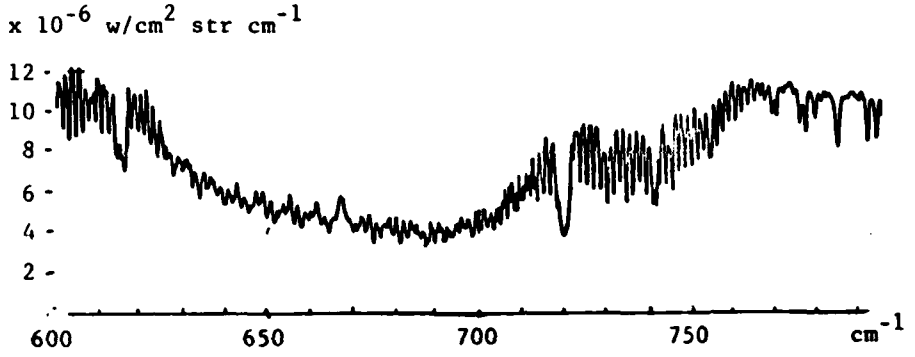

Figure 4. Observed Radiance Level at 28000 m Along Vertical Line of Sight.

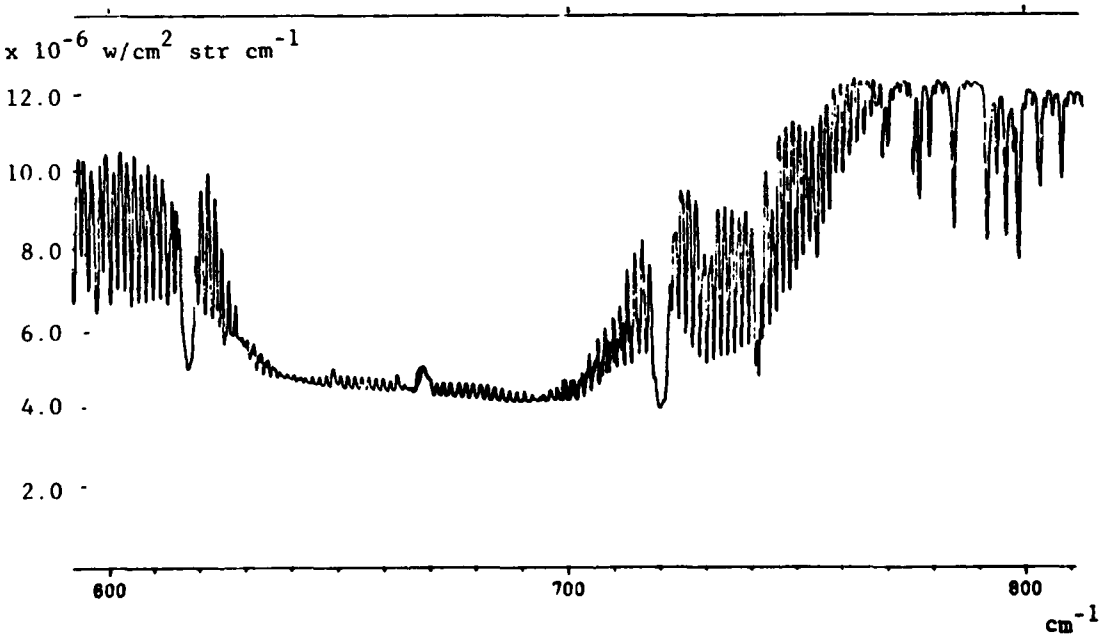

Figure 5. Calculated Radiance Level Along Vertical Line of Sight.
Mid-latitude Model Atmosphere: FASCOD1B
Ground Temperature = 295°K

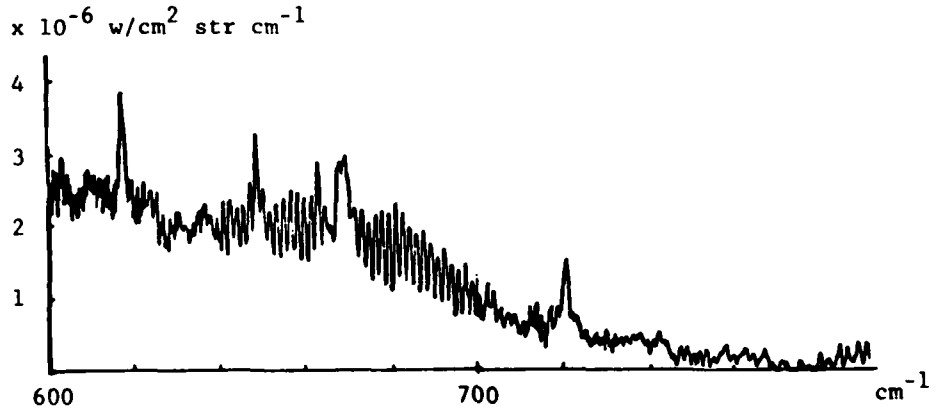

Figure 6. Observed Radiance Level Along Horizontal Line of Sight: 18:15 GMT.

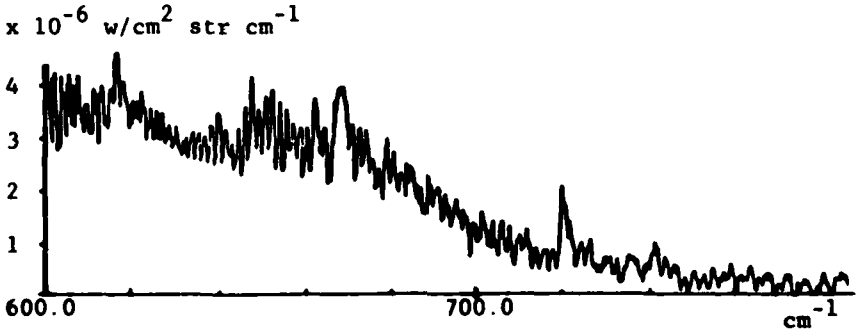

Figure 7. Observed Radiance Level Along Horizontal Line of Sight: 18:45 GMT.

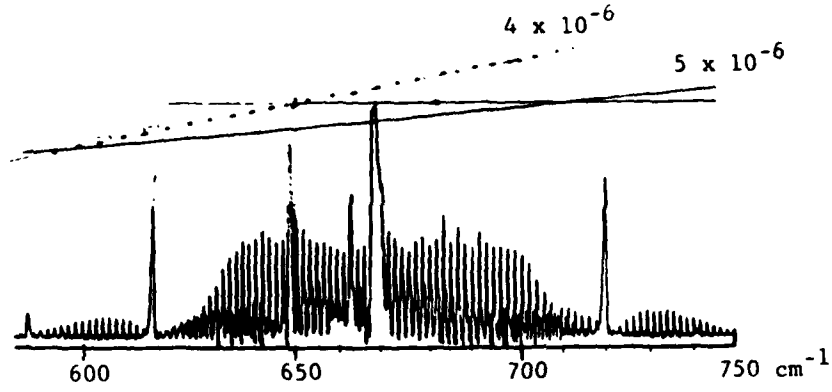

Figure 8. Emissivity Calculated Assuming CO_2 Column Density = 4×10^{20} Molecules/cm^2 and Temperature = $230^{\circ}K$.

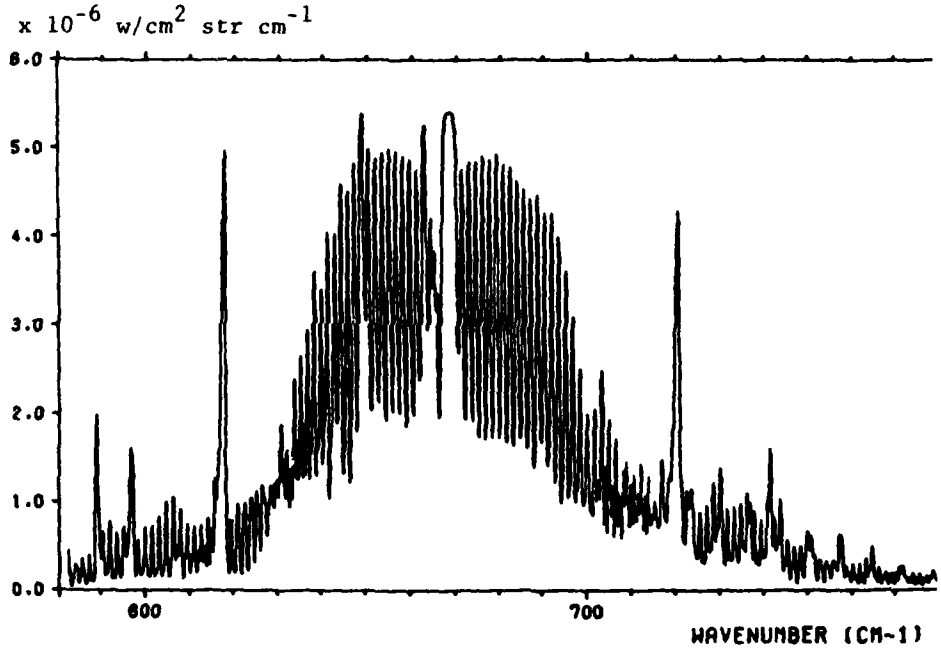

Figure 9. Radiance Calculated Using FASCOD1B, CO_2 Column Density = 1.2×10^{21} Molecules/cm^2, and Temperature = $220^{\circ}K$.

J. Phys. B: At. Mol. Phys. 15 (1982) L873–L879. Printed in Great Britain

LETTER TO THE EDITOR

Theory of rotational branch structure with application to N_2 and CO

Edward S Chang

Department of Physics and Astronomy, University of Massachusetts, Amherst, MA 01003, USA

Received 17 August 1982

Abstract. Analysis of rotational branch structure in high resolution electron energy-loss spectroscopy is greatly facilitated by a high j approximation to the Clebsch–Gordan coefficient. A more accurate approximation than Read's is found for molecules in the Σ state. When assimilated into the theory of Chang, the resulting expressions for the branch differential cross sections for N_2 and CO turn out to be easily evaluated by hand. In both cases, good agreement is found with experiment in both the shape and the magnitude of the cross sections at an electron energy of around 2 eV.

With the continuing improvement of energy resolution in electron energy-loss spectroscopy, it has finally become possible to separate out the rotational branches in typical molecules such as N_2 and CO. The process of deconvoluting the branches was greatly facilitated by utilising the high j (rotational quantum number) approximation, elegantly advanced by Read (1972). However, the approximation is good only to order j^{-1}, or alternatively by Read's own estimation, the error is within a factor of two given by $(50l_{max}/j)\%$. Either way yields an error of 10% in the present case where $j \simeq 10$. Further, even with the above approximation, Read's expression for the differential cross section is sufficiently cumbersome as to require a computer for its evaluation.

In this letter, an alternative high j approximation is proposed, which is valid to order j^{-2} and therefore 1%. When incorporated into the theory of Chang (1977a, b, referred to as I and II respectively), it produces simple expressions for the rotational branches of the differential cross section, which are easily evaluated by hand. To demonstrate the utility of the present method, we evaluate these expressions for N_2 and CO in the Π resonance region around 2 eV. Comparison will be made with the experimental data of Jung *et al* (1982) and the theory of Read and Andrick (1971). To emphasise that the present theory predicts more than just the angular distribution, comparison will also be made for the integrated cross sections.

In contrast to the theory of Read (Read and Andrick 1971, Read 1972), the theory of Chang contains only one squared Clebsch–Gordan coefficient which depends on the rotation quantum numbers j and $j' = j + \Delta$. For Σ states, all magnetic quantum numbers vanish. Thus, we only need a high j approximation for the following

$$(j0, t0|j+\Delta 0)^2 = (2j+2\Delta+1)\begin{pmatrix} j & t & j+\Delta \\ 0 & 0 & 0 \end{pmatrix}^2. \tag{1}$$

0022-3700/82/230873+07$02.00 © 1982 The Institute of Physics

The U.S. Government is authorized to reproduce and sell this report. Permission for further reproduction by others must be obtained from the copyright owner.

A well known formula (Edmonds 1957) gives the expression in terms of factorials,

$$(j0, t0|j+\Delta\,0)^2 = \frac{(2j+2\Delta+1)(2j+\Delta-t)!\,(t+\Delta)!\,(t-\Delta)!}{(2j+\Delta+t+1)!}\left(\frac{\left(j+\frac{t+\Delta}{2}\right)!}{\left(j+\frac{\Delta-t}{2}\right)!\left(\frac{t+\Delta}{2}\right)!\left(\frac{t-\Delta}{2}\right)!}\right)^2. \tag{2}$$

After some manipulation we obtain

$$(j0, t0|j+\Delta 0)^2 = \left(1+\frac{2\Delta+1}{2j}\right) \times \frac{(t+\Delta-1)!!\,(t-\Delta-1)!!\left(1+\frac{\Delta+t}{2j}\right)\left(1+\frac{\Delta+t-2}{2j}\right)\cdots\left(1+\frac{\Delta-t+2}{2j}\right)}{2^t\left(\frac{t+\Delta}{2}\right)!\left(\frac{t-\Delta}{2}\right)!\left(1+\frac{\Delta+t+1}{2j}\right)\left(1+\frac{\Delta+t-1}{2j}\right)\cdots\left(1+\frac{\Delta-t+1}{2j}\right)}. \tag{3}$$

In the high j limit, we may keep terms only to order j^{-1} and ignore terms of $O(j^{-2})$. Then we find

$$(j0, t0|j+\Delta 0)^2 \simeq \left(1+\frac{\Delta}{2j}\right)\frac{(t-\Delta-1)!!\,(t+\Delta-1)!!}{2^t\left(\frac{t-\Delta}{2}\right)!\left(\frac{t+\Delta}{2}\right)!}. \tag{4}$$

Note that the dependence on j in equation (4) entirely lies in the trivial factor $(1+\Delta/2j)$. Further, detailed balance is satisfied to the same order since

$$\left(1-\frac{\Delta}{2j}\right)\frac{d\sigma}{d\Omega}(vj \to v'j+\Delta) = \left(1+\frac{\Delta}{2j}\right)\frac{d\sigma}{d\Omega}(vj \to v'j-\Delta). \tag{5}$$

To confirm the validity of our approximation, the right hand side of equation (4) is evaluated numerically for $j = 10$ in table 1. The exact values below the approximate

Table 1. High j and exact squared Clebsch–Gordan coefficients for $j = 10$.

	t				
Δ	0	1	2	3	4
0 (−1)	1 1	(0.475 0.476)	0.25 0.252	(0.179 0.181)	0.141 0.144
1 (−2)		0.525 0.524	(0.338 0.338)	0.197 0.198	(0.141 0.144)
2 (−3)			0.413 0.410	(0.265 0.265)	0.172 0.173
3 (−4)				0.359 0.355	(0.219 0.217)
4					0.328 0.322

ones are obtained from the tables of Rotenberg *et al* (1959). The agreement is about 2%, which is hardly surprising since we have neglected terms of order j^{-2} with $j = 10$. The sum rule, which requires that the columns add to unity, is satisfied by the approximate values (as by the exact ones) to ±0.001. Finally we note that the double factorial in equation (4) is related to the gamma function by (Abramowitz and Stegun 1964)

$$(2n-1)!! = 1.3\ldots(2n-1) = 2^n\Gamma(n+\tfrac{1}{2})/\sqrt{\pi}. \tag{6}$$

So $(-1)!!$ has the value of unity when $n = 0$ in equation (6).

Now the approximation in equation (4) will be utilised in the analysis of branch structure in N_2 and CO at the 2 eV resonance. For the Π resonance, the expression for the rotational–vibrational differential cross section has been given in equation (II.4). In the case of N_2, the $^2\Pi_g$ resonance implies that $\cos 2\beta = -1$, resulting in this simple expression,

$$\frac{d\sigma}{d\Omega}(vj \to v'j+\Delta) \simeq 4\pi\sigma_{vv'}\left(1+\frac{\Delta}{2j}\right)\sum_t \frac{(t-\Delta-1)!!\,(t+\Delta-1)!!}{2^t\left(\frac{t-\Delta}{2}\right)!\left(\frac{t+\Delta}{2}\right)!}(21, t0|21)^2\Theta(t; 2222\Theta). \tag{7}$$

In equation (7) $\sigma_{vv'}$ may be regarded as a normalisation factor, which is constant except for the often negligible factor of $[(E-E_{\Delta v,\Delta j})/E]^{2.5}$ for d waves. It is obvious that the dependence on j lies only in the first bracket and so members of the same rotational branch Δ have the same angular distribution. For the analysis of energy-loss data, Jung *et al* (1982) had to represent the entire branch by a single 'level' labelled by the appropriate typical value of j. Evidently, this value should be the median so that about half of the rotational population lay on one side and half on the other. In terms of the area under the energy-loss spectra, the same choice should be made with a slight shading to the low j side for $\Delta > 0$ (and the high j side for $\Delta < 0$) because of the $(1+\Delta/2j)$ factor. At a temperature of 500 K in the Jung experiment, the median value of j for N_2 is 10 with 42.9% of the population in $j = 0$ to 9 and 48.5% in $J = 11$ to ∞.

We proceed to evaluate equation (7) explicitly for the case of N_2. The Clebsch–Gordan coefficients and the angular functions Θ may be found in table 1 of I. The results are

$$\frac{d\sigma}{d\Omega}(vj \to v'j) = \sigma_{vv'}(0.301 - 1.540\cos^2\theta + 2.310\cos^4\theta) \tag{8a}$$

$$\frac{d\sigma}{d\Omega}(vj \to v'j\pm 2) = \tfrac{1}{10}\sigma_{vv'}\left(1\pm\frac{1}{j}\right)(0.651 - 0.663\cos^2\theta + 0.886\cos^4\theta) \tag{8b}$$

$$\frac{d\sigma}{d\Omega}(vj \to v'j\pm 4) = \tfrac{1}{10}\sigma_{vv'}\left(1\pm\frac{2}{j}\right)(0.503 + 0.336\cos^2\theta + 0.055\cos^4\theta). \tag{8c}$$

After summing over all rotational branches, we obtain

$$\frac{d\sigma}{d\Omega}(v \to v') = \sigma_{vv'}(0.536 - 1.607\cos^2\theta + 2.5\cos^4\theta) = \tfrac{15}{28}\sigma_{vv'}(1 - 3\cos^2\theta + \tfrac{14}{3}\cos^4\theta) \tag{8d}$$

which first appeared in the work of Ehrhardt *et al* (1968). For the vibrational excitation

$v = 0 \rightarrow v' = 1$, say at 2.27 eV, our results based on equations (8) are indistinguishable from those of Read and Andrick (1971), where Read's high j approximation has not been used. As discussed by Jung *et al* (1982), experiment is in excellent agreement with theory. However, one minor difference is the ratio of areas under the rotational branches. Our analysis gives the ratios for $\Delta = -2$ to $+2$ as 0.82 and for $\Delta = -4$ to $+4$ as 0.63, while that of Jung *et al* obtained from Read's approximation gives the values 0.76 and 0.56. Further, it should be emphasised that equations (8) contain only one normalisation factor σ_{01}, so that once it is determined from any one of the four expressions, the other three show excellent agreement with experiment, not only in the shape but also in the magnitude of the differential cross sections.

The case of the $^2\Pi$ resonance has already been treated by Chang (1977b) in II. With the high j approximation developed here, we obtain the differential cross sections,

$$\frac{d\sigma}{d\Omega}(vj \rightarrow v'j) = (\sigma_{vv'})[(1+\cos 2\beta)^2(0.038 + 1.103\cos^2\theta) + (1-\cos 2\beta)^2(0.298 - 1.532\cos^2\theta + 2.302\cos^4\theta) + (2\sin^2 2\beta)(-0.507\cos\theta + 1.478\cos^3\theta)] \tag{9a}$$

$$\frac{d\sigma}{d\Omega}(vj \rightarrow v'j \pm 1) = (\sigma_{vv'})\left(1 \pm \frac{1}{2j}\right)2\sin^2 2\beta \times (0.102 + 0.319\cos\theta + 0.230\cos^2\theta - 0.650\cos^3\theta) \tag{9b}$$

$$\frac{d\sigma}{d\Omega}(vj \rightarrow v'j \pm 2) = (\sigma_{vv'}/10)\left(1 \pm \frac{2}{2j}\right)[(1+\cos 2\beta)^2(0.56 + 0.19\cos^2\theta) + (1-\cos 2\beta)^2(0.67 - 0.66\cos^2\theta + 0.89\cos^4\theta) + 2\sin^2 2\beta(-0.14\cos\theta - 0.40\cos^3\theta)] \tag{9c}$$

$$\frac{d\sigma}{d\Omega}(vj \rightarrow v'j \pm 3) = (\sigma_{vv'}/10)\left(1 \pm \frac{3}{2j}\right)2\sin^2 2\beta \times (0.54 - 0.67\cos\theta + 0.27\cos^2\theta - 0.13\cos^3\theta) \tag{9d}$$

$$\frac{d\sigma}{d\Omega}(vj \rightarrow v'j \pm 4) = (\sigma_{vv'}/10)\left(1 \pm \frac{4}{2j}\right)(1-\cos 2\beta)^2(0.50 + 0.33\cos^2\theta + 0.06\cos^4\theta). \tag{9e}$$

After summing over all the branches, we obtained equation (II.2) as expected.

Figure 1 shows the fit of equation (II.2) to the vibrational excitation data of Jung *et al* (1982). They obtained a value of $\cos 2\beta = 0.15$, which differed somewhat from the previous value of 0.25 resulting from fitting to the data of Ehrhardt *et al* (1968).

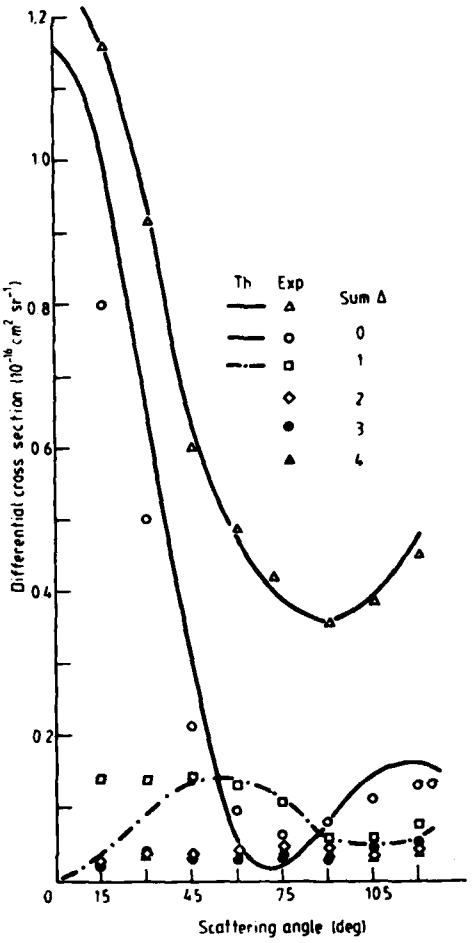

Figure 1. Differential cross sections by rotational branches in CO of resonant vibrational excitation at 1.8 eV. Experimental points are from Jung *et al* (1982), while theory is from equations (9) and (II.2), with $\cos 2\beta = 0.15$.

Also seen are the differential cross sections for the rotational branches $\Delta = 0$, and +1. The agreement between theory and experiment is better revealed here than in the ratios shown by Jung *et al*. The other branches given by equations (9*c* to *e*) are virtually indistinguishable from the data and are not shown. Nevertheless, significant discrepancy exists in the forward direction in all branches of CO, which is even apparent in the case of N_2. Examination of the energy-loss profiles of Jung *et al* (1982) at small angles shows that virtually all broadening is due to the instrumental width rather than the inelastic branches. Therefore, the deconvolution technique become unreliable and, in addition, some discrepancy may also be due to the non-resonant contributions neglected by theory as discussed by Jung *et al* (1982). In contrast to our theory, Jung *et al* found that the theory of Read and Andrick (1971) did not agree well with their data, in spite of the presence of more parameters.

Finally, our theory is capable of predicting the integrated branch ratios to the vibrational cross section, i.e., $\sigma(vj \to v'j + \Delta)/\sigma(v \to v')$. Table 2 shows these ratios from theory and from the experiment of Jung *et al* (1982). In N_2, because all differential cross sections are symmetrical about 90°, they are able to account reliably for the

Table 2. Integrated rotational branch ratios† in N_2 and CO for vibrational excitation $v{-}0 \rightarrow 1$.

	N_2		CO	
Δ	Theory‡	Experiment§	Theory‡	Experiment‖
0	0.5	0.477	0.358	—
+1			0.183	
+2	0.138	0.157	0.070	
+3			0.071	
+4	0.150	0.157	0.026	
−1			0.166	
−2	0.113	0.118	0.058	
−3			0.052	
−4	0.100	0.091	0.017	

† Ratios are taken with respect to the vibrational excitation cross section $\sigma(v = 0 \rightarrow 1)$. Each column should add to 1.

‡ Strictly speaking, each theoretical ratio should be multiplied by the flux conservation factor $[(E - E_{v\Delta})/(E - E_{v0})]^{(2l+1)/2}$, which differs from unity by less than 3% in the present cases.

§ Jung *et al* (1982) 2.25 eV: for conversion into absolute cross sections, the denominator is 5.41×10^{-16} cm^2. Ratios at other resonant energies are virtually identical.

‖ Jung *et al* (1982) 1.8 eV, unavailable, (missing data from 120 to 180°): for conversion into absolute units, the denominator is 7.45×10^{-16} cm^2.

missing range of 120 to 180°. It can be seen that the agreement between theory and experiment is about 10%. For the case of CO, the differential cross section of the rotational branches are quite asymmetrical about 90°, so no experimental values are given. Nevertheless, the vibrational (summed over rotational branches) cross section is symmetrical, so $\sigma(0 \rightarrow 1)$ at 1.8 eV can be determined reliably to be 7.45×10^{-16} cm^2. (This value is about twice as large as the one measured by Ehrhardt *et al* (1968)). So theoretical absolute rotational cross sections for each branch can be obtained by multiplying this value to the ratios given in the last column of table 2.

In summary, the high j approximation developed here is shown to be more accurate than Read's by one order of magnitude. When incorporated into the theory of Chang, the resulting expressions are so simple as to obviate the use of a computer. Theoretical rotational branch cross sections in vibrational excitation in N_2 and CO are evaluated and shown to be in good agreement with experiment in both shape and magnitude. Application of theory to non-Σ states is deferred to a future work.

The author acknowledges useful correspondence with H Ehrhardt, and thanks J F Walker for a fruitful discussion. This work was supported by Air Force Contract #F19628-81-K-0007.

References

Abramowitz M and Stegun I A 1964 *Handbook of Mathematical Functions* (Washington, DC: National Bureau of Standards)

Chang E S 1977a *Phys. Rev.* A **16** 1841–9
—— 1977b *Phys. Rev.* A **16** 1850–3
Edmonds A R 1957 *Angular Momentum in Quantum Mechanics* (Princeton, NJ: Princeton University Press)
Ehrhardt H, Langhans L, Linder F and Taylor H S 1968 *Phys. Rev.* **173** 222–30
Jung K, Antoni Th, Muller R, Kochem K H and Ehrhardt H 1982 *J. Phys. B: At. Mol. Phys.* **15** 3535–55
Read F H 1972 *J. Phys. B: At. Mol. Phys.* **5** 255–64
Read F H and Andrick D 1971 *J. Phys. B: At. Mol. Phys.* **4** 911–7
Rotenberg M, Bivens R, Metropolis N and Wooten J K 1959 *The 3-j and the 6-j Symbols* (Cambridge, MA: MIT)

J. Phys. B: At. Mol. Phys. 16 (1983) L581–L585. Printed in Great Britain

LETTER TO THE EDITOR

The *n*f complexes in molecular nitrogen

Edward S Chang† and K Yoshino‡

† Department of Physics and Astronomy, The University of Massachusetts, Amherst, Massachusetts 01003, USA

‡ Harvard-Smithsonian Center for Astrophysics, Cambridge, Massachusetts 02138, USA

Received 12 July 1983

Abstract. We have investigated the vacuum ultraviolet absorption of N_2 at 77 K. The bands at 810, 815 and 825 Å are identified as the (0, 0) bands of the 7f, 6f and 5f complexes, each with O, Q and S branches. Theoretical analysis of our data confirms a theoretical value for the quadrupole moment of $2.1\, e\, a_0^2$, and predicts a value of $19\, a_0^3$ for the polarisability of the $N_2^+\ ^2\Sigma_g^+\ (v=0)$ core.

Typical molecular Rydberg states, which are core penetrating are usually studied in absorptions from the ground state in the wavelength region below 1000 Å (Yoshino *et al* 1976, 1979). On the other hand, non-penetrating Rydberg states are found in infrared emissions: 5g–4f in NO by Dressler *et al* (1981) and 5g–4f and 4f–3d in H_2 and D_2 by Herzberg and Jungen (1982). We report here absorptions from the ground state to the non-penetrating *n*f Rydberg complexes of N_2. The spectra for each complex resemble the P, Q and R branches of an ordinary electronic band, except that the spacing between adjacent lines here is $4B$ rather than $2B$ (where the rotational constant B is nearly equal for both the upper and lower states). Our theory attributes this feature to all homonuclear molecules in a Σ ground state. Therefore it was not present in the 4f and 5f absorption study of the $^2\Pi$ state of NO (Jungen and Miescher 1969), which was complicated further by the unpaired electron spin.

In this work the absorption spectra of nitrogen were photographed by a 6.65 m McPherson Model 265 vacuum spectrograph in the second order. The reciprocal linear dispersion of the spectrum is approximately 0.63 Å mm^{-1}. Figure 1 (plate) shows the absorption spectrum of N_2 at liquid nitrogen temperature from λ = 808–830 Å. Features marked *n*f clearly correspond to the approximate wavelengths of $n = 7$, 6 and 5 in $(I - \mathrm{Ryd}/n^2)$, if we adopt the ionisation potential of I = 125 667.5 cm^{-1} (Loftus and Krupenie 1977). Not shown is the appearance of the isotope bands, $^{15}N_2$, at about the same wavelength which confirms the vibration assignment of these bands as the (0, 0). For greater clarity, the 810 Å feature is shown in figure 2(*a*) on an expanded wavenumber scale. On the left side of this figure, it is evident that the main absorption lines are regularly spaced at about 8 cm^{-1} apart, which is $4B$ since the rotational constants of N_2 and N_2^+ are B = 1.9982 and B' = 1.9319 cm^{-1} respectively. In fact, the intensities are seen to alternate with strong/weak lines as expected in an ordinary P (or R) branch. However as just noted, the spacing here is $4B$ rather than $2B$, so by analogy we label this group the O branch. Not unexpectedly, the Q branch is not completely resolved, and appears primarily as the broad feature at 123 413 cm^{-1}. The S branch overlaps slightly with the Q branch and takes on a somewhat irregular appearance as will be explained later.

© 1983 The Institute of Physics

The U.S. Government is authorized to reproduce and sell this report. Permission for further reproduction by others must be obtained from the copyright owner.

Theory for non-penetrating molecular Rydberg states appropriate for low rotational states has been given by Herzberg and Jungen (1982) and by Eyler and Pipkin (1983). In Hund's coupling case d, the Hamiltonian is nearly diagonal with the diagonal elements given by

$$E_{nlRN} = I - \frac{\text{Ryd}}{n^2} + R(R+1)B' - \alpha P(n,l) - \frac{2QC(l,R,N)}{n^3 l(l+\frac{1}{2})(l+1)}\text{Ryd}. \tag{1}$$

The ionisation potential I is already given, Ryd for N_2 is 109 735.16 cm^{-1}, R is the rotational quantum number of N_2^+, and its rotational constant $B' = 1.9319\,cm^{-1}$. The polarisability and the quadrupole moment Q of the core are treated here as independent of R, as in the work of Jungen and Miescher (1969). It is also understood that α is the isotropic part of the polarisability, while the anisotropic part is essentially hidden in Q, representing the effective quadrupole moment. The standard polarisation formula (Edlen 1964) gives

$$P(n,l) = \frac{3n^2 - l(l+1)}{2n^5(l-\frac{1}{2})l(l+\frac{1}{2})(l+1)(l+\frac{3}{2})}\text{Ryd} \tag{2}$$

while Eyler and Pipkin (1983) find

$$C(l,R,N) = \frac{3Y(Y-1) - 4R(R+1)l(l+1)}{2(2l-1)(2l+3)(2R-1)(2R+3)} \tag{3}$$

where

$$Y = R(R+1) + l(l+1) - N(N+1). \tag{4}$$

They also give the off-diagonal matrix elements which couple states of the same N but different R, however not odd and even values because of nuclear symmetry. These have the same n (and l) dependence as the last term in equation (1). In diagonalising the Hamiltonian, the value of $Q = 2.10\,ea^2$ found by Cade (1983) is used (his value of $Q = 2.08\,ea_0^2$ is substantially different from $3.12\,ea_0^2$ quoted in Krauss (1967)). For the 7f states, the shifts of the eigen-energies due to the off-diagonal matrix elements is seldom larger than 1 cm^{-1}, but for lower values of n, these shifts can be more substantial.

The initial state is of course $N_2\,X\,{}^1\Sigma_g^+$ $(v=0, N)$ in Hund's coupling case b, with its energy given by $N(N+1)B$. Then the transition wavenumber is trivially given by the energy difference shifted by $\alpha P(n,l)$, where the unknown α may be treated as a parameter. However, the transition strengths are not readily calculated when the lower state is in Hung's case b and the upper state is in case d. We choose to transform the lower state $X_{l\Lambda}^N$ into a superposition of case d states $\Phi_{l,R}^N$, preserving parity and nuclear symmetry. From the frame transformation theory (Chang and Fano 1972), the $3\sigma g$ molecular orbital approximated by the d component becomes

$$X_{20}^N = (20, N0|N-20)\Phi_{2,N-2}^N + (20, N0|N0)\Phi_{2,N}^N + (20, N0|N+20)\Phi_{N+2}^N \tag{5}$$

where $(l_1m_1, l_2m_2|l_3m_3)$ is the Clebsch–Gordan coefficient. Now the Einstein A coefficient in the electric dipole approximation may be computed from equation (5) and the nf states $\Phi_{3,R'}^{N'}$ to be

$$A_{2RN}^{3R'N'} = \delta_{RR'}(2N'+1)(20, N0|R0)^2 \begin{Bmatrix} R & 3 & N' \\ 1 & N & 2 \end{Bmatrix}^2 F \tag{6}$$

J. Phys. B: At. Mol. Phys. 16 (1983) L581–L585. Printed in Great Britain

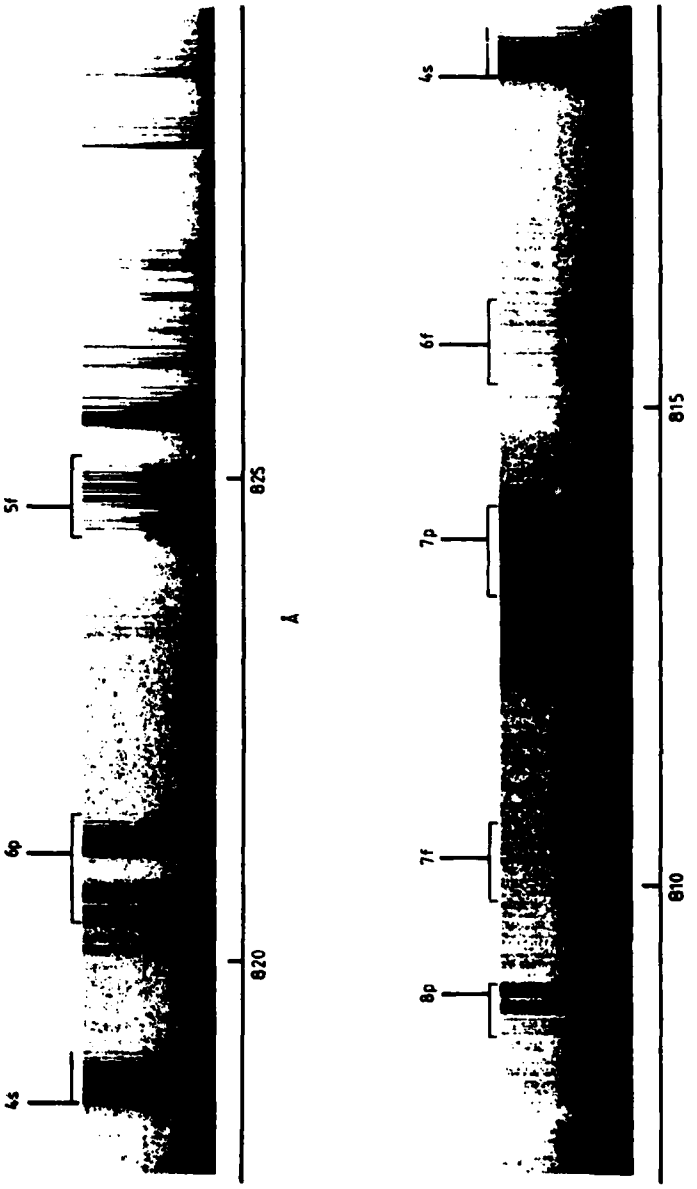

Figure 1. Absorption spectra of nitrogen at 0.09 Torr and 77 K. Features marked 4s and *np* have previously been identified as *ns* o_4 $^1\Pi_u$ and *np* $^1\Pi_u + {}^1\Sigma_u^+$ respectively. The present work elucidates the features marked *nf*.

[facing p L582]

where

$$F=\frac{4}{3}\frac{e^2k^3}{\hbar}(2l+1)(20,10|30)^2|(3d|r|nf)|^2\langle v|v'\rangle^2 \tag{7}$$

may be regarded as a normalisation factor. The Krönecker delta in equation (6) emphasises that the N_2^+ core remains passive while the $3\sigma g$ molecular orbital absorbs a photon into the *nf* Rydberg orbital. However, equation (6) belies the fact that an initial state is really a superposition of three (or less) core states, of which only one can contribute to the A coefficient for a particular σ. Correspondingly, three branches arise depending on

$$R-N=\begin{cases}-2: & \text{O branch}\\ 0: & \text{Q branch}\\ +2: & \text{S branch.}\end{cases}$$

Since B' is approximately equal to B in N_2 and the effect of the last term in equation (1) is relatively small, the absorption spectra are organised into the above three branches with the Q branch piling up in the band centre and the O and S branches spreading out with a spacing of approximately $4B$. The designation of O, Q and S branches to describe the rotationally resolved photoionisation cross sections in H_2 was advocated by Niehaus and Ruf (1971). Our adoption of their rotation emphasises the similarity of l uncoupling in absorption here to the uncoupling of the electron into the continuum there.

Further, the intensities are obtained by multiplying the A coefficients to the population, i.e.,

$$I^R_{NN'}=g(2N+1)\exp[-N(N+1)B/kT]A^{3RN'}_{2RN}. \tag{8}$$

In equation (8) g has the value 2 when N = even (nuclear symmetry s) and the value 1 when N = odd (a) in isotope 14, which gives rise to the alternation of intensities. At 77 K, there is only adequate population up to the $N=8$ level. Therefore we can expect about 15 lines, which are easily discernible in figure 2.

In figure 2(*b*), we show calculated line positions shifted by 17.5 cm^{-1} and the calculated intensities broadened by the instrumental line widths. The lines are designated by the three branches, O, Q and S with the lower rotational state given below. The subscripts P, Q or R are the normal spectroscopic branch notation for $N'-N=-1$, 0, or 1 respectively. Here they serve no organising purpose, but instead cause each line to split into three. Fortunately, in the O branch, the O_R lines are substantially more intense than the other two. Consequently they dominate the spectra from 123 343 to 123 395 cm^{-1} appearing regularly with a spacing of about 8 cm^{-1} and with an alternation of intensities. The Q branch starts out at 123 405 cm^{-1}, but quickly piles up at the broad structure, 123 410 to 123 415 cm^{-1}, engulfing the strong $S_R(O)$ line. Finally, the S branch assumes a somewhat irregular appearance because the intensities here are more evenly distributed among the S_P, S_Q and S_R lines.

Generally, the agreement between observed and calculated line position is within ± 0.5 cm^{-1}. Occasionally it is worse when the identification is more doubtful. Usually the intensity pattern also compares favourably. It should be noted that while the calculated intensities are linear the observed densitometer tracings are not. The shift of 17.5 cm^{-1} in the calculated spectra implies a value of $19\,a_0^3$ for α. Overall, the combined position and intensity matching leave no doubt of the correct identification of the 7f complex.

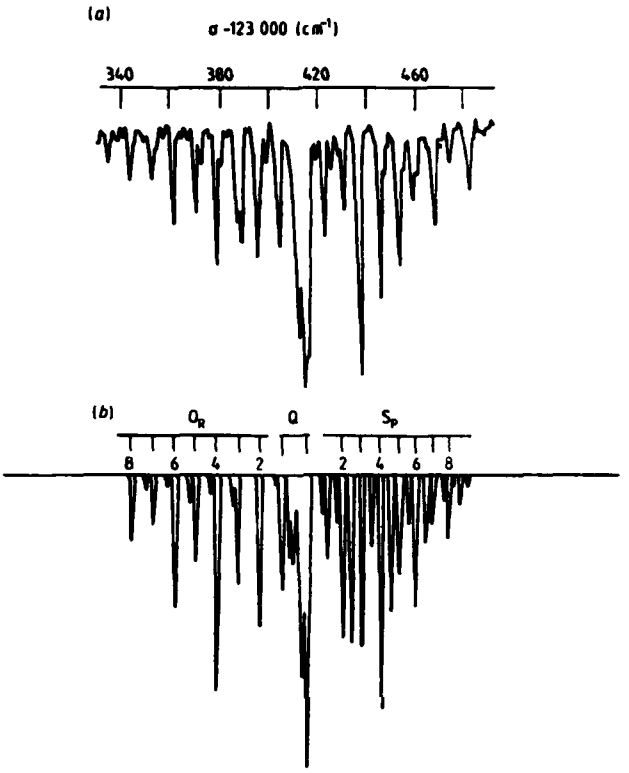

Figure 2. High resolution spectra of 7f. (*a*) Experiment, (*b*) theory calculated with the experimental line width.

Returning to the 815 and the 824 Å features in figure 1 (plate), we are able to identify them as the 6f and the 5f complexes in N_2. Computation with equation (1) using the same values of α and Q from the 7f complex generally yields line positions within 1 cm^{-1} of the data. It should be noted that better fits can be obtained by treating both α and Q as free parameters as in the case of atoms (Chang and Sakai 1982). Such work with a detailed analysis of the 5f and 6f complexes is deferred to the future.

In conclusion, we have measured and identified the 5f, 6f and 7f spectra in the ultraviolet absorption of N_2. In particular, the 7f complex is seen to have a regular O branch, a compressed Q branch, and a somewhat irregular S branch. These features are expected to be common in the UV spectra of other molecules in Σ states.

We thank S Polchtopek for the computer work producing figure 2(*b*). Partial support by the US Air Force under AFGL Contract No 19628-81-K-007 is gratefully acknowledged.

References

Cade P E 1983 private communication

Chang E S and Fano U 1972 *Phys. Rev.* A **6** 173–85
Chang E S and Sakai H 1982 *J. Phys. B: At. Mol. Phys.* **15** L649–53
Dressler K, Jungen Ch and Miescher E 1981 *J. Phys. B: At. Mol. Phys.* **14** L701–4
Edlen B 1964 *Encyclopedia of Physics* vol 27 (Heidelberg: Springer)
Eyler E E and Pipkin F M 1983 *Phys. Rev.* A **27** 2462–78
Herzberg G and Jungen Ch 1983 *J. Chem. Phys.* **77** 5876–84
Jungen Ch and Miescher E 1969 *Can. J. Phys.* **47** 1769–87
Krauss M 1967 *Technical Note N55* (Washington, DC: US Govt Printing Office)
Loftus A and Krupenie P H 1977 *J. Phys. Chem. Ref. Data* **6** 113–307
Niehaus A and Ruf M W 1971 *Chem. Phys. Lett.* **11** 55–7
Yoshino K, Freeman D E and Tanaka Y 1979 *J. Mol. Spectrosc.* **76** 153–63
Yoshino K, Ogawa M and Tanaka Y 1976 *J. Mol. Spectrosc.* **61** 403–11

Extended analysis of the $5g \rightarrow 4f$ emissions in H_2

Edward S. Chang and Stanley Pulchtopek

Department of Physics and Astronomy, University of Massachusetts, Amherst, Massachusetts 01003

E. E. Eyler[a)]

Department of Physics, Harvard University, Cambridge, Massachusetts 02138
(Received 16 June 1983; accepted 6 October 1983)

An analysis starting from Hund's case d has been used to extend the work of Herzberg and Jungen on the $5g \rightarrow 4f$ emissions in H_2. A simple analytical expression for the line intensities is presented that agrees with their calculations is about 1%. All of the experimentally observed lines have been accounted for by including higher vibrational levels in our calculations.

Recently, a group of infrared emission lines in H_2 has been identified as the electronic transitions between two nonpenetrating Rydberg states, namely the $5g$ and the $4f$ states, by Herzberg and Jungen[1] (referred to as HJ). Their theoretical treatment started from a Hund's coupling case b basis and the Hamiltonian was then transformed into Hund's case d. Instead, we have chosen to start from case d because the Hamiltonian is already nearly diagonal in this basis set, following the same general approach that was applied to the triplet $4d$ states of H_2 by Eyler and Pipkin[2] (referred to as EP). After applying small corrections towards case b, the resulting level energies are essentially identical to those found by HJ. The case d approach is particularly useful for the line intensities, where a simple analytical expression gives results that agree closely with the numerical calculations of HJ.[3] This formulation is nearly identical to our treatment of the analogous states in atoms.[4,5] A number of the observed lines were not previously identified. By extending the calculation to higher vibrational numbers, we have been able to account for all of these lines, indicating that all of the observed spectra belong to the $5g-4f$ system.

In Hund's coupling case d, the diagonal term of the Hamiltonian is given in EP as

$$E_{nlRN\nu}(0) = I - \frac{Ry}{n^2} + \epsilon(R,v) - \alpha Ry\langle r^{-4}\rangle_{nl} - 2Ry\left[Q\langle r^{-3}\rangle_{nl} + \tfrac{2}{3}\gamma\langle r^{-4}\rangle_{nl}\right]\langle lRN|P_2|lRN\rangle \ . \quad (1)$$

The states are labeled according to electronic angular momentum l, core rotation R, and total angular momentum N. This notation differs from that of HJ, but agrees with EP and the commonly accepted usage of Hougen's monograph.[6] In Eq. (1) the first term is, of course, the Rydberg term, where for H_2, $Ry = 109\,707.45\ \mathrm{cm}^{-1}$. The next term is the rotational-vibrational energy of the H_2^+ core as calculated by Hunter *et al.*[7] In the third term, α is the expectation value of the isotropic polarizability of the core $\alpha = \langle Rv|\alpha(A)|Rv\rangle$, where the internuclear separation is denoted by A to avoid confusion with the rotation R. $\alpha(A)$ is taken from Bishop and Cheung[8] as was done in HJ. The last term contains the anisotropic interaction between the angular momenta of the electron l and of the core R. Q is the expectation value of the quadrupole moment $Q = \langle Rv|Q(A)|Rv\rangle$, where $Q(A)$ is taken from the more extensive calculation of Karl *et al.*[9] rather than from Bates and Poots[10] as was done in HJ. The anisotropic polarizability $\gamma = \langle Rv|\alpha_\parallel(A) - \alpha_\perp(A)|Rv\rangle$ is calculated in the same manner as α. Sample values of α, γ, and Q are 3.181 and $4.027a_0^3$, and $1.643ea_0^2$ for $R=1$ and $v=0$, which compare closely with those given in Table I of EP.

From Eq. (1), the energy level structure of the $5g$ (or $4f$) state can be easily envisioned. All levels are uniformly shifted downwards as predicted by the polarization model,[11] of order 1 cm^{-1} for the $5g$ or 10 cm^{-1} for the $4f$. The main splitting is due to the core's rotational and vibrational structure with a spacing of $\simeq 100\ \mathrm{cm}^{-1}$, analogous to the atomic core fine structure spacing. Interplay between R and l through the quadrupole interactions produces a finer splitting of the order $\simeq 1\ \mathrm{cm}^{-1}$ for the $5g$ (or $\simeq 10\ \mathrm{cm}^{-1}$ for the $4f$). The resultant angular momentum N and, in turn, the energy $E_{nlRN}(0)$ depend on the relative orientation of l and R. When N is a maximum (or minimum), l and R are parallel (or antiparallel), so the positively charged molecular axis lies in the plane of the Rydberg electron's orbit, thereby lowering the electrostatic energy. In contrast, when N is midway, l and R are perpendicular, and the electrostatic energy is then the highest. Of course, quantum precession ameliorates the simple classical picture resulting in some out of the plane motion and less electrostatic attraction when N is a maximum. Consequently, the energy levels are usually ordered $N_{\min}$, $N_{\max}$, $N_{\min}+1$, $N_{\max}-1$, etc.[1] While this simple picture explains the level structure well, it neglects the nondiagonal interaction between different R levels (subject to the *para/ortho* restriction). The off-diagonal terms have the same form as Eq. (1) except that the last factor must be changed to

$$\langle lRN|P_2|lR'N\rangle = (-1)^{R+R'}(2l+1)\sqrt{(2R+1)(2R'+1)} \times \begin{pmatrix} l & 2 & l \\ 0 & 0 & 0 \end{pmatrix}\begin{pmatrix} R & 2 & R' \\ 0 & 0 & 0 \end{pmatrix}\begin{Bmatrix} N & R' & l \\ 2 & l & R \end{Bmatrix} . \quad (2)$$

In Eqs. (1) and (2), explicit expressions for $\langle r^{-3}\rangle_{nl}$, $\langle r^{-4}\rangle_{nl}$, and the 3-$j$ and 6-j symbols were given in EP. The resultant matrices for each value of n, l, N, v, and

a) Present address: Yale University Physics Department, New Haven, Connecticut 06511.

 0021 9606/84/020601 05$02.10 © 1984 American Institute of Physics

The U.S. Government is authorized to reproduce and sell this report. Permission for further reproduction by others must be obtained from the copyright owner.

TABLE I. Calculated and observed wave numbers of the $5g \rightarrow 4f$ lines in H_2. † denotes new identification and * signifies contrary identification to HJ.

σ_c	Branch v	σ_0	σ_c	Branch v	σ_0
2459.89	$R_1(3)$ 0	2459.50	2500.39	$Q_3(2)$ 3	2500.38
2459.94	$R_1(3)$ 1	2459.50	2502.93	$R_2(5)$ 2	2502.89
2460.65	$Q_3(4)$ 2	2459.96	2503.05	$R_2(2)$ 3	2502.89
2460.68	$R_1(3)$ 2	2459.96	2503.63	$R_0(3)$ 3	
2460.69	$Q_3(4)$ 3	2459.96	2504.34	$R_3(1)$ 0	
2461.02	$Q_3(4)$ 1	2461.44	2504.71	$R_1(2)$ 1	2504.76
2461.39	$Q_3(4)$ 4	2461.44	2504.72	$R_3(6)$ 2	2504.76
2461.62	$Q_3(4)$ 0	2461.44	2504.90	$Q_1(4)$ 1	2504.76
2461.87	$R_2(3)$ 4	2462.14 *	2506.21	$R_2(1)$ 0	2506.36
2462.11	$R_2(3)$ 3	2462.14	2506.52	$R_3(2)$ 3	2506.36
2462.43	$R_2(3)$ 5	2462.47 *	2507.38	$Q_3(2)$ 4	
2462.48	$R_1(3)$ 3	2462.47	2508.04	$R_1(4)$ 3	2508.34
2462.73	$R_2(3)$ 2	2462.82	2510.67	$R_2(5)$ 3	2509.06 †
2463.12	$R_3(4)$ 2	2462.82	2511.02	$R_3(1)$ 1	2511.29
2463.19	$R_3(4)$ 1	2462.82	2511.05	$R_2(2)$ 4	2511.29
2463.22	$Q_3(4)$ 5	2462.82	2511.87	$R_1(2)$ 2	2512.09
2463.50	$R_3(4)$ 0	2463.60	2512.32	$5f$–$4d$ 1	2512.94
2463.50	$R_3(4)$ 3	2463.60	2512.52	$Q_1(4)$ 2	2512.94
2463.51	$R_2(3)$ 1	2463.60	2512.58	$R_3(6)$ 3	2512.94
2464.30	$R_2(3)$ 0	2464.34	2513.21	$R_2(1)$ 1	2513.31
2464.58	$R_3(4)$ 4	2464.34	2513.87	$R_0(3)$ 4	2513.31
2465.31	$R_2(4)$ 0	2464.88	2514.41	$R_3(2)$ 4	2513.75 †
2465.91	$R_1(3)$ 4	2465.52 †	2516.42	$Q_3(2)$ 5	2517.48 †
2466–2470	B_α		2517.89	$R_1(4)$ 4	2515.77 †
2470.34	$Q_3(3)$ 0		2518.96	$R_3(1)$ 2	2518.78 †
2470.85	$Q_3(3)$ 1		2520.54	$R_2(5)$ 4	
2471.28	$R_3(5)$ 2		2520.63	$R_1(2)$ 3	2521.31 *
2471.53	$Q_3(3)$ 2	2471.94 †	2521.51	$R_2(2)$ 5	2521.02
2471.83	$R_1(3)$ 5	2472.34 †	2521.52	$R_2(1)$ 3	2521.02
2472.41	$Q_3(3)$ 3	2472.86 †	2521.92	$Q_1(4)$ 3	2521.02
2473.52	$Q_3(3)$ 4	2473.76	2522.59	$R_3(6)$ 4	
2474.05	$R_3(3)$ 0	2473.76	2523.06	$5f$–$4d$ 1	
2474.08	$R_2(4)$ 4	2473.76	2524.49	$R_3(2)$ 5	
2474.17	$R_3(5)$ 3	2473.76	2527.40	$R_0(3)$ 5	
2474.92	$Q_3(3)$ 5	2475.39	2528.53	$R_3(1)$ 3	
2475.15	$R_3(3)$ 1	2475.39	2530.78	$R_1(4)$ 5	2529.71 *
2476.49	$R_3(3)$ 2		2531.52	$R_2(1)$ 3	2533.12 †
2478.11	$R_3(3)$ 3		2531.54	$R_1(2)$ 4	2533.12
2478.53	$R_3(5)$ 4		2533.37	$R_2(5)$ 5	2534.87 †
2480.09	$R_3(3)$ 4		2533.75	$Q_1(4)$ 4	2534.87
2480.34	$R_2(4)$ 5		2535.55	$R_3(6)$ 5	2534.87
2482.49	$R_3(3)$ 5	2482.97 †			
2485.05	$R_0(8)$ 0	2484.86			
2485.07	$R_3(5)$ 5	2484.86			
2486.74	$Q_3(2)$ 0	2486.21 †			
2487.76	$R_2(2)$ 0	2487.15 †			
2489.51	$R_1(4)$ 0	2489.33			
2489.74	$R_0(3)$ 1	2489.64			
2490.40	$Q_3(2)$ 1	2490.31			
2490.75	$R_3(2)$ 0	2491.04 †			
2491.75	$R_2(5)$ 0	2491.64			
2491.80	$R_2(2)$ 1	2492.99			
2493.22	$R_3(6)$ 0	2493.43 †			
2494.34	$R_1(4)$ 1	2494.25			
2494.49	$5f$–$4d$ 0	2494.76			
2494.86	$Q_3(2)$ 2	2494.76			
2495.03	$R_3(2)$ 1	2495.74			
2495.79	$R_0(3)$ 2	2495.74			
2496.75	$R_2(5)$ 1	2496.67			
2496.79	$R_2(2)$ 2	2496.67			
2498.38	$R_3(6)$ 1	2497.76 †			
2498.59	$5f$–$4d$ 0	2498.65			
2498.66	$Q_1(4)$ 0	2498.65			
2498.78	$R_1(2)$ 0	2498.65			
2500.20	$R_1(2)$ 2	2500.38			
2500.38	$R_1(4)$ 2	2500.38			

TABLE II. Theoretical line strengths and observed intensities according to the present assignments. Brackets denote shared intensities, with the square bracket indicating the strongest line and the round bracket weaker lines. B_α: blended with the atomic Brackett alpha line.

Branch	S	$v=$ 0	1	2	3	4	5
$R_0(3)$	1.00	[2.3]	2.4	[3.0]	0.8	[1.4]	...
$R_1(4)$	3.67	6.5	5.5	[2.7]	2.3	1.3	0.7
$R_1(3)$	2.81	[7.0]	(7.0)	[1.4]	[0.8]	1.3	0.5
$R_1(2)$	2.14	[4.7]	[4.7]	1.7	[1.6]	[0.9]	...
$Q_1(4)$	0.19	(4.7)	(4.7)	(0.5)	(0.5)	(0.9)	...
$R_2(5)$	1.44	1.8	[1.4]	[0.8]	0.5	(1.6)	(0.9)
$R_2(4)$	1.10	1.4	B_α	B_α	B_α	(0.8)	
$R_2(3)$	0.82	[1.4]	(1.0)	(0.3)	[0.5]	(0.5)	(0.8)
$R_2(2)$	0.60	0.6	0.4	(1.4)	(0.8)	(0.4)	(0.5)
$R_2(1)$	0.43	[0.6]	(1.4)	[0.5]	(0.9)	...	...
$R_3(6)$	5.00	0.8	0.9	(4.7)	[0.5]		[0.9]
$R_3(5)$	3.78	B_α	B_α	0.5	(0.8)		(2.3)
$R_3(4)$	2.79	[1.0]	[0.3]	(0.3)	(1.0)	(1.4)	B_α
$R_3(3)$	1.95	[0.8]	[0.6]				0.7
$R_3(2)$	1.32	0.5	(3.0)	(2.7)	(0.6)	0.5	
$R_3(1)$	0.81		[0.4]	1.0		...	...
$Q_3(4)$	0.96	[1.4]	(1.4)	(1.4)	(1.4)	(1.4)	(0.3)
$Q_3(3)$	0.93			0.5	0.5	(0.8)	(0.6)
$Q_3(2)$	0.75	0.5	0.6	0.8	(2.7)		0.7

$(-1)^R$ are diagonalized to yield the eigenenergies E_{nlRNv}.

In conformity with the HJ notation, the transition frequency σ is labeled by the lower state. Thus,

$$\sigma[R_R(N)v] = E_{54R(N+1)v} - E_{43RNv} \,. \tag{3}$$

The intensity is proportional to the product of the line strength S and the Boltzmann factor. From the Einstein A coefficients given in EP, the line strength S is

$$S = \{2-(-1)^R\}(2N'+1)\begin{pmatrix} 4 & N' & R \\ N & 3 & 1 \end{pmatrix}^2 . \tag{4}$$

The first factor is the statistical weight due to nuclear spin, i.e., 1 when R is even (*para*) or 3 when R is odd (*ortho*). The rest of Eq. (4) is identical to the analogous line strengths in atoms.[5]

Results of our calculated σ are given in Table I along with the line designations and the observed values of HJ.

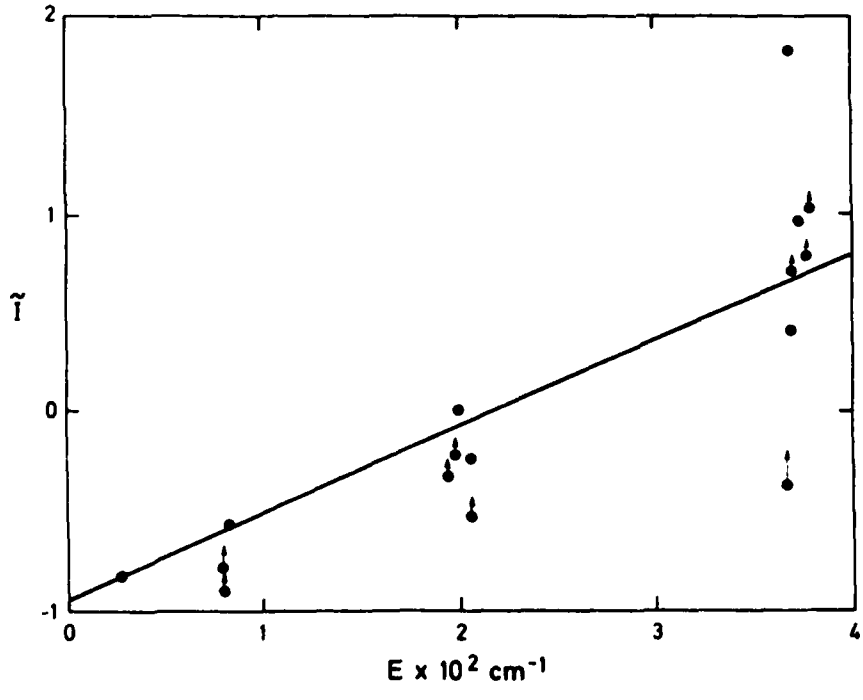

FIG. 1. Determination of the rotational temperature for $v=0$ lines. $\tilde{T}$ given by Eq. (5) is plotted against the energy of the 5g sublevels. Note the bunching of the data points according to $R=0$, 1, 2, and 3. Arrows indicate the direction of displacement due to shared intensities.

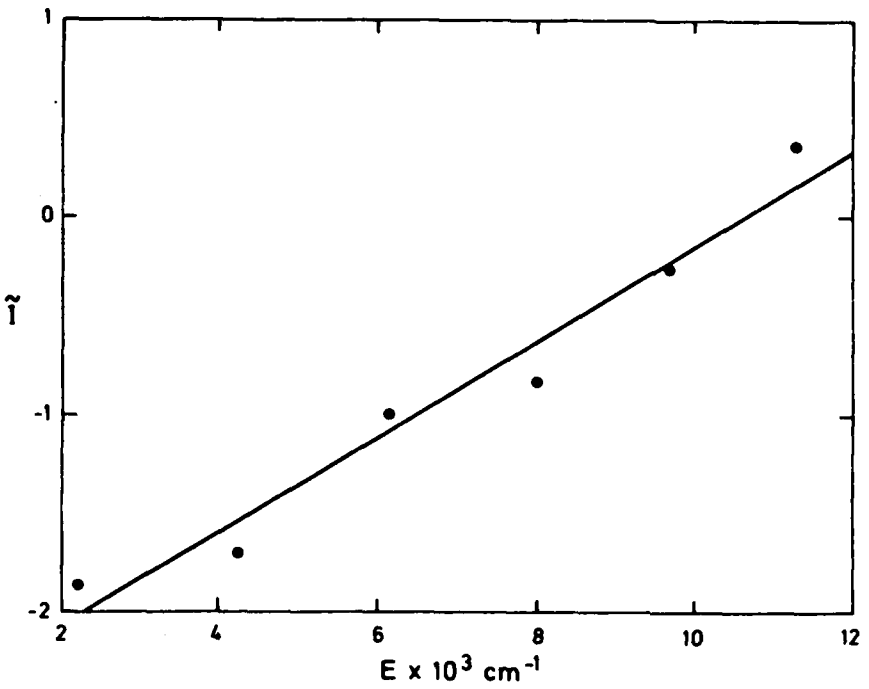

FIG. 2. Determination of the vibrational temperature from the $R_1(4)$ lines. $\tilde{I}$ given by Eq. (5) is plotted against the vibrational energy of the H_2^+ core.

Generally, our calculated values agree with their calculated ones to 0.1 cm^{-1}. In addition, we have calculated σ for $v=4$ and 5 as well as for some weaker lines with $v=0$ to 3. Further, we have calculated the positions of some $5f \rightarrow 4d$ lines. A few fall within the range of the HJ spectra, but there is no convincing evidence that any of these lines have been observed. It is possible that some of the observed spectra share intensity with these transitions. From Table I, it is seen that we are able to identify all observed lines. More often than not, an experimental feature corresponds to more than one calculated line, though usually only one is expected to be strong. The new identifications are marked †. While we agree with HJ on the identification of strong lines, we have made a few reassignments of the weaker lines, marked by asterisks.

The task of line assignment is greatly facilitated by intensity considerations. In Table II, we show the line strengths given by Eq. (4) for all of the calculated transitions. The other columns show the experimental line intensities I_0 from HJ, using the revised assignments. To facilitate analysis of the rotational temperature, the Boltzmann factor was separated from the theoretical line strength from Eq. (4) by taking the ratio

$$\tilde{I} = -\ln(I_0/S) = E/kT \ . \tag{5}$$

In Fig. 1, we plot $\tilde{I}$ against E for $v=0$. It fits a straight line reasonably well, taking into account that arrows indicate the effect of shared intensity. From the slope, we determine a rotational temperature of 330 K in rough agreement with the value quoted in HJ.

Experimental intensities for higher v reveal a general decreasing trend as v increases. They also have more shared or missing lines, making a determination of rotational temperature for each higher v difficult. Fortunately, the intense $R_1(4)$ lines are unshared for all v, so a vibrational temperature can be extracted. Figure 2 shows that a straight line fits the data rather well, where E is the vibrational energy[7] of H_2^+. From the slope, we determine a vibrational temperature of 6000 K, thus confirming the HJ value. With the addition of the higher vibrational quantum numbers, the task of identification has been completed in that all experimental lines are now labeled and conversely, all theoretically strong lines are matched to an experimental feature.

In conclusion, our extended analysis strengthens the identification of the spectra between 2459 and 2534 cm^{-1} observed by HJ as the $5g \rightarrow 4f$ emissions in H_2. In particular, each observed line is assigned to one or more of the calculated $5g \rightarrow 4f$ lines from $v=0$ to 5. Our line assignments are mostly the same as HJ with just a few exceptions. Thus, there is no evidence for the existence of other systems or resolvable singlet–triplet splittings in the above spectral range. However, our extended calculations and new assignments provide more information allowing for a more accurate determination of the rotational and vibrational temperatures. While the former is only moderately well defined and somewhat higher than the value found by HJ, the latter is surprisingly well defined and is identical to the value of HJ. Finally, this l-uncoupling model including only long-range interactions is shown to be a powerful tool for investigating the spectra of molecules as well as of atoms involving nonpenetrating Rydberg states.

ACKNOWLEDGMENTS

This work was supported by the Air Force under AFGL Contract number F19628-81-K-0007, to the University of Massachusetts and in part by NSF PHY80-26547 to Harvard University.

[1]G. Herzberg and Ch. Jungen, J. Chem. Phys. **77**, 5876 (1982).
[2]E. E. Eyler and F. M. Pipkin, Phys. Rev. A **27**, 2462 (1983).
[3]Ch. Jungen (private communication).
[4]E. S. Chang and H. Sakai, J. Phys. B **15**, L649 (1982)..
[5]E. S. Chang and H. Sakai, J. Phys. B **14**, L391 (1981).
[6]J. T. Hougen, *The Calculation of Rotational Energy Levels and Rotational Line Intensities in Diatomic Molecules*, Natl. Bur. Stand. (U.S.) Monogr. **115** (U. S. GPO, Washington, D. C., 1970).
[7]G. Hunter, A. W. Yau, and H. O. Prithcard, At. Data Nucl. Data Tables **14**, 11 (1979).
[8]D. M. Bishop and L. M. Cheung, J. Phys. B **11**, 3133 (1978). Another calculation of $\alpha(A)$ by A. I. Sherstyuk and N. S. Yakovleva, Opt. Spectrosc. (USSR) **40**, 560 (1976) is found to contain minor numerical errors.
[9]G. Karl, B. Nickel, J. D. Poll, and L. Wolniewicz, Phys. Rev. Lett. **34**, 1302 (1975).
[10]D. R. Bates and G. Poots, Proc. Phys. Soc. London Sect. A **66**, 784 (1953).
[11]B. Edlen, *Encyclopedia of Physics* (Springer, Heidelberg, 1964), Vol. 27.

TIME RESOLVED FTS OF MOLECULAR AND ATOMIC INFRARED EMISSION

W. Barowy and H. Sakai

Astronomy Research Facility, Department of Physics and Astronomy

University of Massachusetts, Amherst, Mass. 01003, U.S.A.

The technique of Fourier spectroscopy applied to time dependent studies was first developed by Sakai and Murphy (1,2,3). The technique is essentially to measure the time dependent interferogram signal given by:

$$F(x,t) = \int B(\sigma,t) \cos 2\pi\sigma x \, d\sigma. \qquad (1)$$

The spectral signal $B(\sigma,t)$ is recovered by applying the inverse transformation to the interferogram $F(x,t)$ with the same t:

$$B(\sigma,t) = \int F(x,t) \cos 2\pi\sigma x \, dx. \qquad (2)$$

Our scheme is devised to measure the time resolved interferogram $F(x,t)$ at each position of x while the time parameter varies continuously. The entire $F(x,t)$ are collected by repeating the same procedure for all x from zero to the maximum path difference, as the interferometer is held at each sample position and then stepped to the next. At the University of Massachusetts , we are applying this technique to the study of atomic and molecular infrared emissions.

SOURCE

The source is a glow discharge operated in the central 12 meters of a 30 meter long, 1 meter diameter steel tube as seen in Figure 1. The discharge is excited by the application of an ac voltage of up to 1000 volts (peak to peak) between the walls of the tube and a 12 meter long, cooled aluminum cylinder, located at the axial center of the tube. The pressure at which the discharge can operate reliably is between 50 and 300 millitorr. Two f/30 mirrors are situated at each end of the tube and focused on each other, providing an optical path length of 90 meters. A KBr lens at the exit port of the tube collimates the beam in preparation for entrance to the interferometer. The simplest waveform used for excitation is a 60 Hz sinusoid generated by a step-down transformer operated in reverse. A pulsed discharge is also used with pulses of both polarities available.

INSTRUMENTATION

The detector is a 3 millimeter diameter InSb photodiode cooled to liquid nitrogen temperature. The detector accepts radiation from the interferometer at the focus of an f/2.25 off-axis parabolic mirror. The interferometer is tilt-compensated with corner reflectors and is scanned in the step-and-hold mode. Our corner-reflector interferometer is shown in Figure 2. Sampling of the time-dependent signal occurs while the movable mirror is held in position with a servo mechanism referenced to the 6329A line of a HeNe laser. Thus the unit stepping distance is 6329A.

The mirror is driven by a linear "speaker-coil" motor with the

control electronics enslaved to an LSI11/V03 computer. The detector signal is wide band amplified (5Hz to 10 KHz) and is sampled by a 12 bit A/D converter at 130 microsecond intervals, the cycle time of the master clock. The master clock is synchronized with the excitation source and the sampling is "locked-in" to the excitation waveform with the phase-locked-loop (PLL). The LSI11 computer reads in the sampled time-resolved interferogram F(x,t) via a DRV11 parallel I/O interface, pre-processes the data to improve the signal-to-noise ratio, and stores the results on either a floppy disk [DX1] or a magnetic tape [TM11] via the PDP11/20. A block diagram of the apparatus is shown in Figure 3.

PREPROCESSING

The recording of the time-resolved interferogram F(x,t) is controlled by the software structured as in the flow chart shown in Figure 4. The entire scheme enjoys the flexibility and power inherent in software processing. As the signal is repetitively sampled, the LSI11 co-adds corresponding points of each excitation cycle in real-time for each optical path retardation. The possible number of coadditions is virtually unlimited; in reality, however, it is constrained by the holding time of the LN2 dewar. This mode preserves the time dependence of the signal while increasing the signal-to-noise as the square root of the number of coadditions. Thus, molecular features that appear weak or out of phase with the excitation can be detected and the phase of peak emission determined using low spectral resolution. Then appropriate processing such as synchronous demodulation can be programmed for non-time-resolved, high resolution studies of these features.

However, synchronous demodulation may distort a spectrum in a modulating source due to different excitation and de-excitation rates and phases of individual spectral features (4). In this case, where interest is in the entire spectrum, an asynchronous sum is done, which is simply the integral of the modulus of the A.C. component of the waveform. In this manner all frequency components of the signal are summed, independent of phase, and the contributions of each spectral element are maximized. 60 Hz pick-up, which is independent of path difference, adds a D.C. offset to the interferogram in this type of average. The offset can be calculated however, by sampling the signal with a shunt resistance placed across the detector output. This can then be subtracted later from the interferogram. At present, preprocessing of non-time-resolved spectra allow integration times that are constrained solely by the dewar holding time.

Instabilities, such as arcs in the discharge, are compensated by intelligent data acquisition routines. This is especially important in Fourier Spectroscopy, where an arc could cause a spike in the interferogram, thereby distorting the entire spectrum.

By a short study of arcing phenomena, we have found that arcs tend to appear at specific times in the excitation cycle. When an arc occurs, it is apparent in both the waveform of the disharge current as well as the detector signal. Implementation of "smart" routines with time resolution allow the computer to identify these anomalies within certain tolerances, and to reject them if they occur.

POSTPROCESSING

The spectral recovery process is performed as indicated in Figure 4. The first step in rearranging F(x,t) requires a very large working space in order to perform it with high efficiency. For example, a study with spectral resolution of 1 wavenumber requires over one million data to be shuffled. Currently we use our University central site CDC Cyber system for the rearranging process as well as the rest of the spectral recovery.

PRELIMINARY RESULTS

Some typical data for nitrogen and oxygen in the 60 Hz discharge are shown in Figures 5 and 6, respectively. The time evolution flows from the top to the bottom of the figures. For clarity, the full time resolution is not displayed, rather, the presented spectral plots occur approximately 2 milliseconds apart. The spectral resolution is 4 wave numbers. The first plot of each series corresponds to a point in time when the voltage of the central electrode is positive with respect to the walls of the tube and near its peak value.

Several features in the development of the spectrum of nitrogen that are immediately apparent are the $B^3\Pi$-$A^3\Sigma$ transitions in Figure 5(e-h) between 6000 and 7500 wave numbers. Atomic lines of nitrogen and oxygen in Figure 5(e-g) and Figure 6(e-g) show preferentially during only specific stages of the discharge cycle.

We believe that the cylindrical geometry of the source leads to a significant difference in the distribution of electron energies with respect to the polarity of the applied voltage. In general, the cross sections for electron impact excitation from the ground state of the

molecule to an upper state depend on the identity of the excited state as well as the incident electron energy (5). As a result, individual electronic states of a molecule manifest themselves in the discharge at different stages as seen in Figures 5 and 6. This is complicated by the extreme variety in lifetimes of these electronic states (6,7) and by the role of collisions, which lead to such phenomena as intra-system cascading.

The process of unraveling these effects will be facilitated with the pulsed discharge, where the external excitation can be applied or removed rapidly, and the evolution of excited states followed by examining the infrared spectrum. At our present operating pressures, many of the infrared transitions of atmospheric molecules have radiative decay rates comparable to the mean inter-molecular collision rate, thereby providing a good probe for exploring the excitation and relaxation phenomena.

ACKNOWLEDGEMENT

This research is supported by AFOSR under the Atmospheric Science Project 2310.

References

1 R.E.Murphy and H.Sakai, Proc. of Aspen Int'l Conf. on Fourier Spectroscopy, p. 301 (1971)

2 R.E.Murphy,F.Cook and H.Sakai,J.Opt.Soc.Am. 65 600 (1975)

3 H.Sakai and R.E.Murphy,Appl.Opt. 17, 1342 (1978)

4 R.E.Murphy, in Spectrometric Techniques, Vol.I Ed., G.A.Vanasse, pp.229-278, Academic Press, N.Y. (1977)

5 D.C. Cartwright et al, Phys. Rev. A 16, 1013 (1977) D.C. Cartwright et al, Phys, Rev. A 16, 1041 (1977).

6 A. Lofthus and P.H. Krupenie, J. Phys. Chem. Ref. Data, 6, pp. 113-307 (1977)

7 P. Krupenie, J. Phys. Chem. Ref. Data, 1, pp. 425-534 (1972)

FIGURE CAPTIONS

Figure

1 Schematic representation of the discharge source.

2 Corner-Reflector Interferometer

3 Block Diagram of the Apparatus

4 Flow Chart for Data Processing

5 The time evolution of the spectrum of molecular nitrogen in the modulated glow discharge.

6 The time evolution of the spectrum of molecular oxygen, showing several atomic lines appearing in plots e-g.

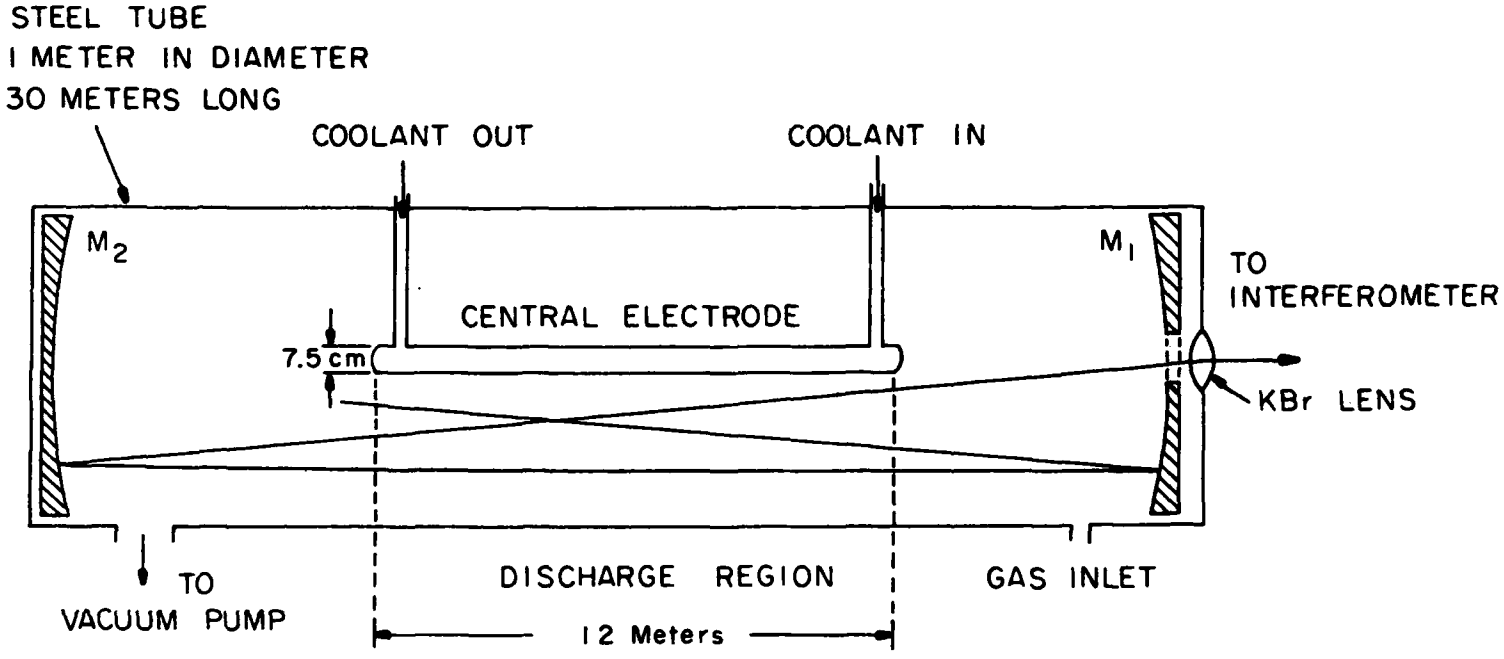
STEEL TUBE
1 METER IN DIAMETER
30 METERS LONG
COOLANT OUT
COOLANT IN
M2
M1
TO
INTERFEROMETER
CENTRAL ELECTRODE
7.5 cm
KBr LENS
TO
VACUUM PUMP
DISCHARGE REGION
GAS INLET
12 Meters

Figure 1

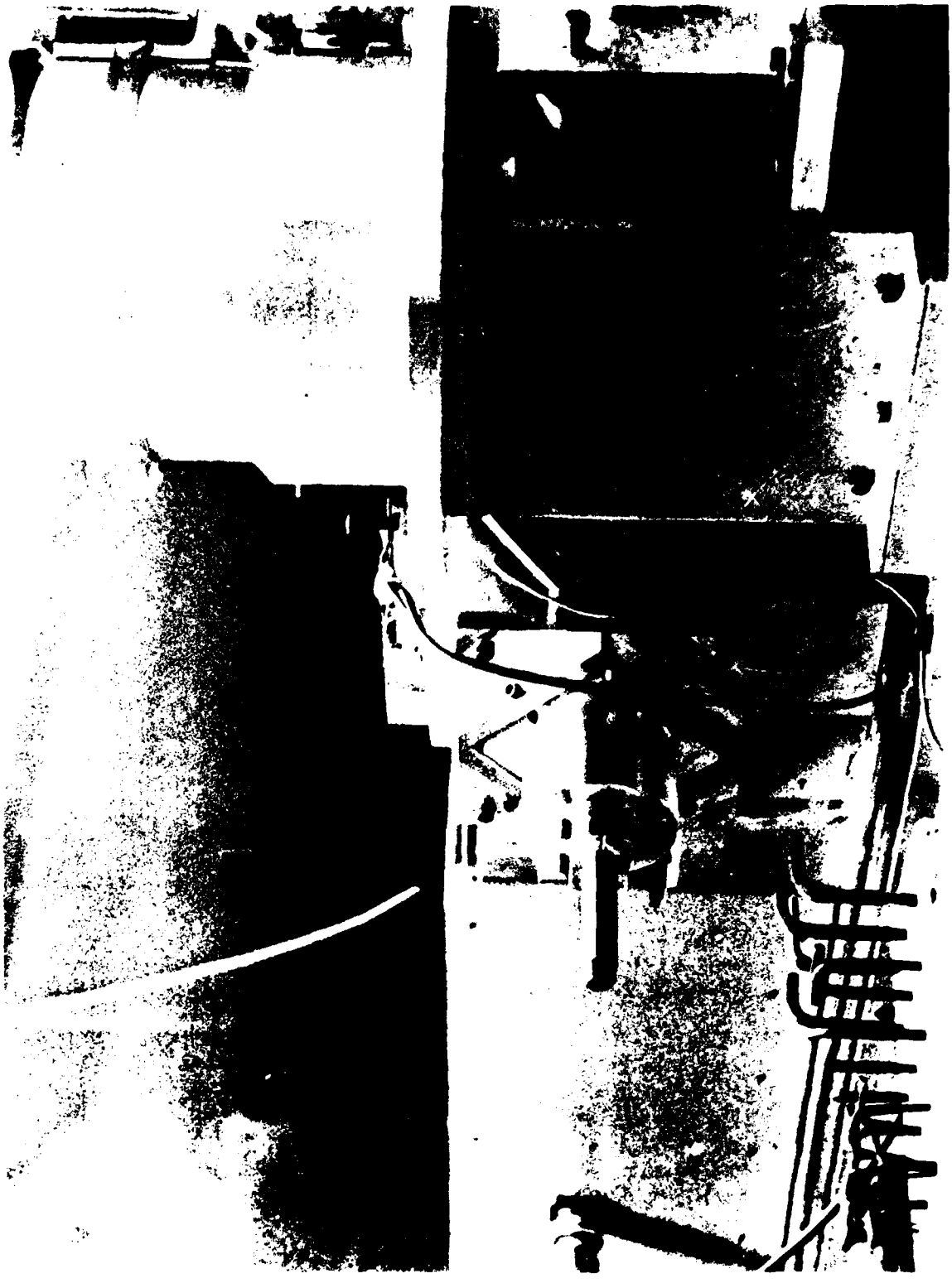

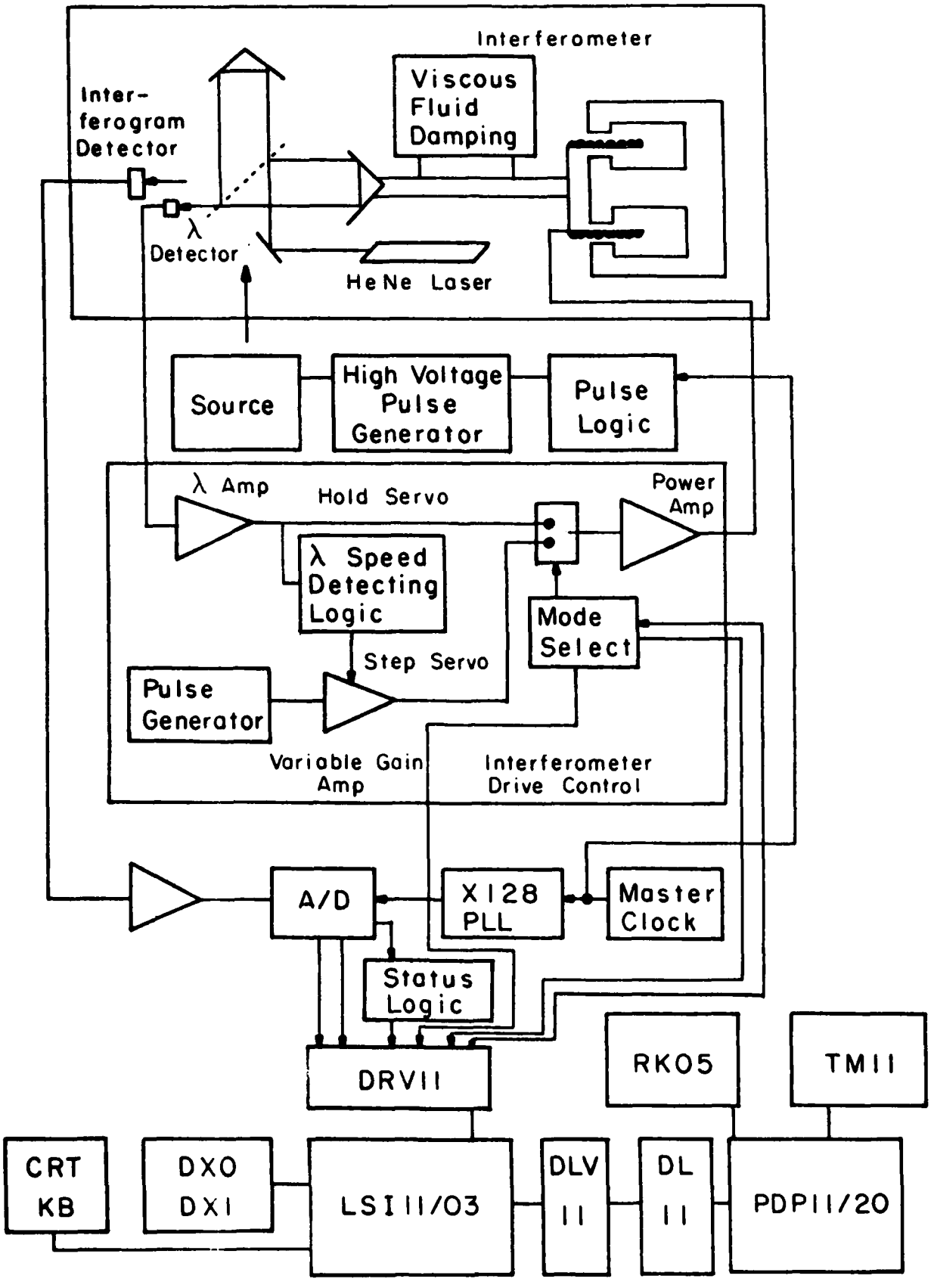
Interferometer
Viscous Fluid Damping
Inter-ferogram Detector
λ Detector
He Ne Laser
Source
High Voltage Pulse Generator
Pulse Logic
λ Amp
Hold Servo
Power Amp
λ Speed Detecting Logic
Mode Select
Step Servo
Pulse Generator
Variable Gain Amp
Interferometer Drive Control
A/D
X128 PLL
Master Clock
Status Logic
DRV11
RK05
TM11
CRT KB
DXO DXI
LSI11/03
DLV 11
DL 11
PDP11/20

Figure 3

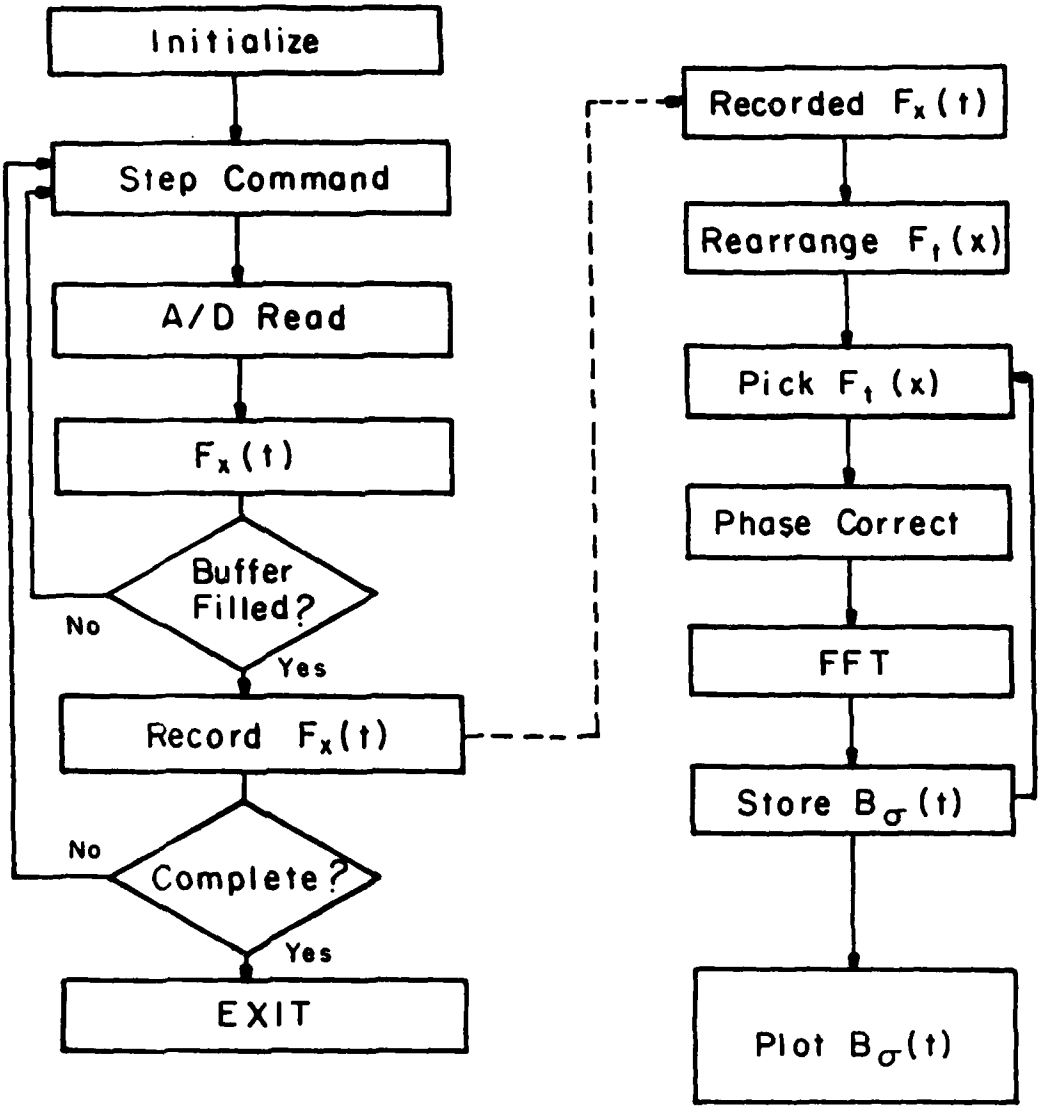
Initialize
Step Command
A/D Read
$F_x(t)$
Buffer Filled?
No
Yes
Record $F_x(t)$
Complete?
No
Yes
EXIT
Recorded $F_x(t)$
Rearrange $F_t(x)$
Pick $F_t(x)$
Phase Correct
FFT
Store $B_\sigma(t)$
Plot $B_\sigma(t)$

Figure 4

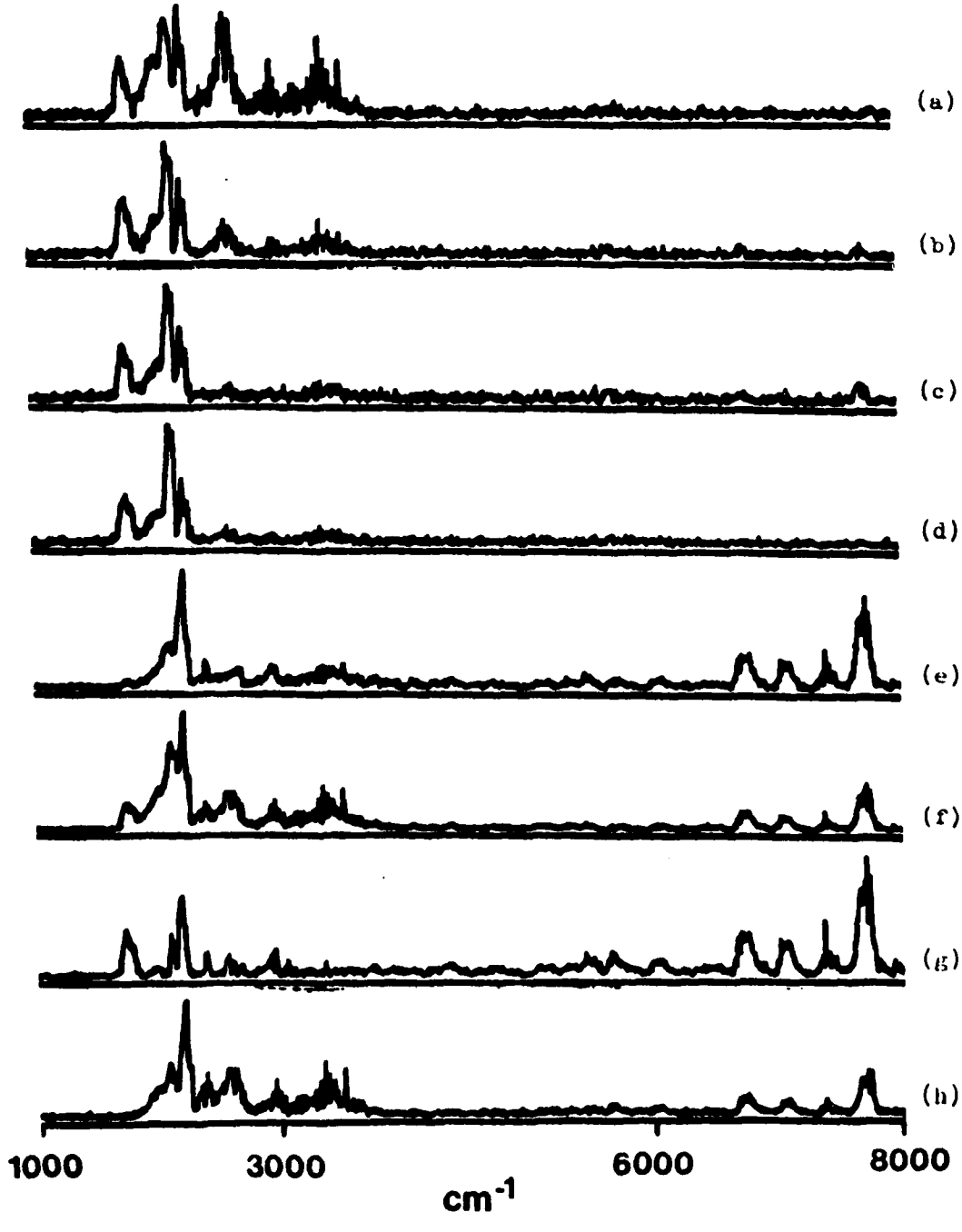

Figure 5

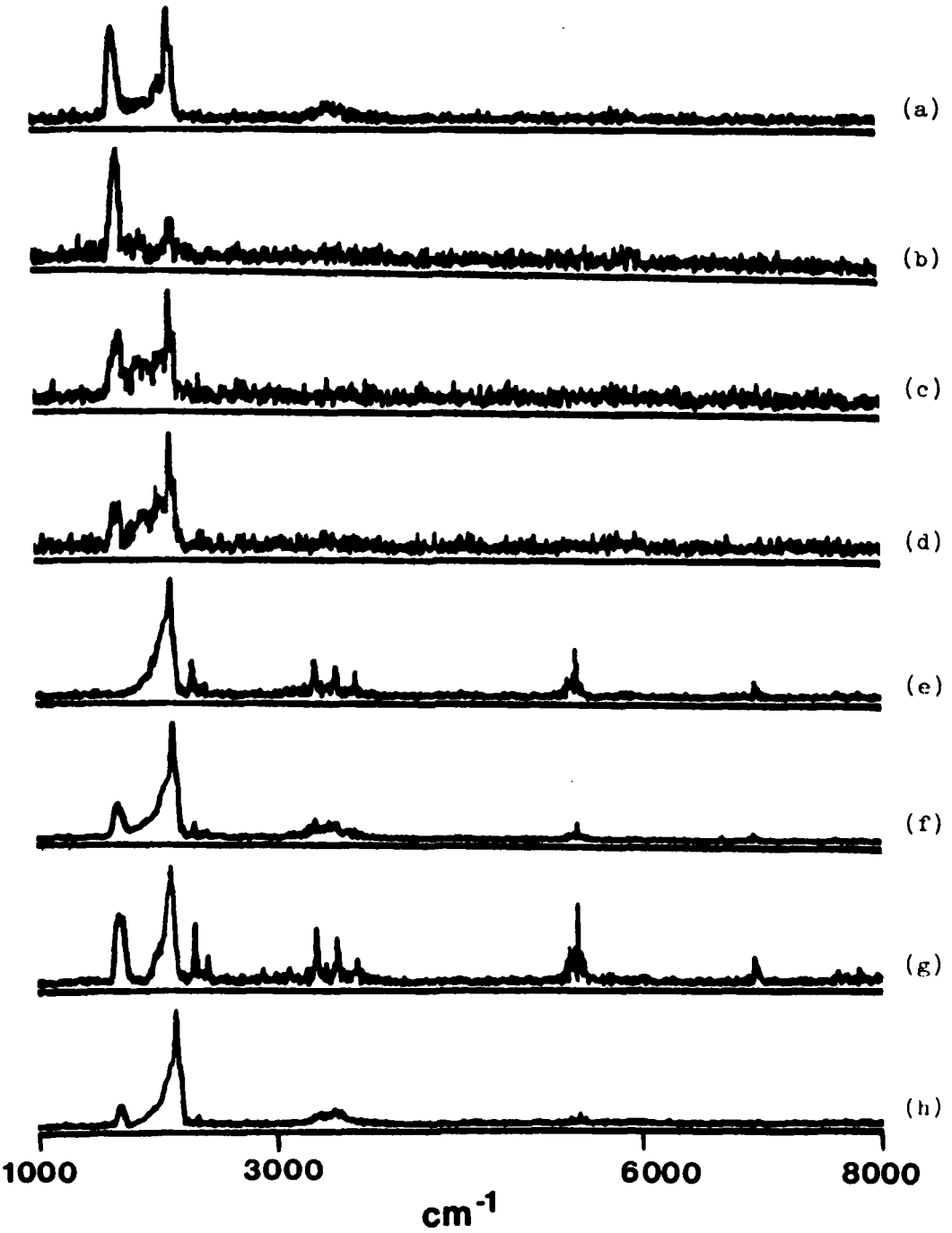

Figure 6

CRYOGENIC FOURIER SPECTROSCOPY FOR THE INFRARED ATMOSPHERIC EMISSION MEASUREMENT†

H. Sakai
Astronomy Research Facility, Department of Physics and Astronomy
University of Massachusetts, Amherst, Massachusetts 01003, U.S.A.

G. Vanasse
Optical Physics Division, Air Force Geophysics Laboratory
Hanscom AFB, Massachusetts 01731, U.S.A.

James Pritchard
Idealab, Inc., P.O. Box 427, Franklin, Massachusetts 02038,U.S.A.

F.J.Murcray
Department of Physics, University of Denver, Denver, Colorado 80208, U.S.A.

The infrared radiative process[1] through the lower part of atmosphere is a composite effect of the local characteristics, which are principally controlled by three parameters, the local abundance of the molecules responsible for the radiative process, the local temperature and the local pressure. The molecules in the lower layers of the atmosphere are generally in thermal equilibrium with the local surrounding. The third parameter, the local pressure, plays its effective role only in the atmosphere below the tropopause, while the other two in their role for controlling the infrared radiative process are important throughout the entire low atmosphere including the stratosphere. Under the local thermal equilibrium the radiative transfer characteristics in infrared are determined by integrating the local characteristics in a straightforward computation, once these parameters are known along the path.[2] Thus throughout the atmosphere up to the stratosphere , these parameters are important in their critical

role of controlling the overall budget of the incoming and the outgoing thermal radiation. At present, our knowledge of these parameters in the stratosphere is extremely scarce,as a result of limited observed data existing at present. In hoping to improve our knowledge of these parameters in the stratosphere, we designed an experiment to collect the infrared radiative transfer characteristics in the stratosphere by observing the infrared photons emitted along the horizontal line of sight. A cryogenically-cooled Fourier interferometer spectrometer mounted on a balloon-borne platform was used for the experiment.[3-5] Tne balloon flight took place on October 7, 1981, at Holloman AFB, New Mexico, and obtained the spectral data taken at the balloon altitude of 28500 m for more than two hours.

In the past , the mainstream of the stratospheric spectral study carried out by using the balloon-born platform was the absorption scheme, i.e., by means of the solar spectra.[6] A problem central to the spectral study of the stratosphere , a long absorption path necessary for the detection of various atmospheric species, is not solved in a satisfactory degree with the solar-spectra scheme. Since the absorption path is locked onto the solar position, its extreme length is available at the time of sunrise or sunset. The time available for such measurement is limited to a short time. In addition to this problem , the scheme does not allow a diurnal study of some molecules which are suspected of concentration variation with respect to the solar position.

The spectrometric study on the atmospheric emission was conducted using the satellite-borne spectrometer.[7] The measurements were to observe a cumulative effect of the atmosphere along the vertical line of sight. The individual contribution of a thin atmospheric layer to the overall radiative transfer characteristics was determined by an elaborate analysis scheme, which provided no direct grip on the local characteristics of the radiative transfer.

Our study is intended to supplement these two spectrometric studies by measuring the atmospheric emission spectra along the horizontal line of sight. The measurements are free from the limitations imposed on the solar spectrum scheme. They would be done at any time of day, any season, and at any geographical location. In addition , the measurement scheme is conceptually simple because no elaborate solar tracking system is required. The data collection extends from the beginning to the end of the balloon flight. Our scheme obtains a long atmospheric path in a thin slice of the atmosphere along the horizontal line of sight.

The radiance level expected for the atmospheric emission is characterized by the blackbody radiance of the stratospheric temperature at approximately 220 K. The peak radiance level corresponds to an optically thick layer of the emitting molecules . In general the radiance level is expected less than the blackbody radiance at 220 K. Even though the long path along the horizontal line of sight would optimize the obtained infrared radiance level, it would remain extremely

low, thereby requiring a superb sensitivity to the spectrometer. The instrumentation problem imposes a challenge for achieving the ultimate sensitivity of Fourier spectroscopy.[8-10] Since the incoming photon density is lower than the blackbody radiance density of 220 K, the interferometer spectrometer itself is required to operate at a temperature below the stratospheric temperature of 220 K.

Interferometer

Spectroscopy involved in this experiment requires a high sensitivity, a high spectral resolution, and a wide spectral coverage. The technique of Fourier spectroscopy is only the scheme which satisfies these requirements. The interferometer which is a central part of the instrumentation must function adequately at a temperature much below the stratospheric temperature. With consideration of various factors involved in operation of the instrument, we decided to operate the interferometer at 77 K. The mechanical stability over a wide temperature range is a paramount importance required to the interferometer. James Pritchard took chief responsibility for its design and fabrication. All components of the interferometer were fabricated with A2 steel. They underwent numerous annealing cycles to reduce their thermal stress until they showed a predictable thermal behavior in these annealing cycles between 300 K and 77 K. The entire interferometer was assembled on a solid base plate, as shown in Figure 1. We adapted the cat's eye retroreflecting optical system for the compensation of the wavefront tilt so as to make the two interfering

beams always stay in alignment. The ways which support the movable carriage provided a smooth motion to it at 77 K. The ball-bearing slide together with dry lubricant was found to satisfy the mechanical requirement even at this severe temperature condition. The movable mirror was driven by a speaker-coil type magnetic motor and its position was monitored by both a mechanical transducer and the interference fringes formed by the HeNe cw laser beam. The beamsplitter of a Ge film coated on a KCl substrate was paired with a compensator plate of a similar optical path, and they were mounted jointly to the supporting frame, using a spring-loaded retaining ring which served as a cushion to absorb a thermal stress associated with the temperature cycle. The essential part of our instrument , the interferometer spectrometer together with the detector assembly, was housed in a cryogenic chamber which maintained its interior temperature at 77 K. The detector was a copper-doped germanium photoconductive element operating at the liquid helium temperature. The detector and its dewar were, thus, encased in the 77 K chamber. Figure 2 shows the interior of this chamber. The mounting plate seen at the middle of the chamber was supported by four fiberglass-reinforced epoxy pillars. The interferometer and the detector assembly mounted on the base plate were secured onto this mounting plate. The liquid nitrogen reservoir seen in the lower section of the chamber held enough liquid nitrogen to maintain the interior temperature at 77 K for 10 hours or longer.

The interferometer scanning was monitored by the HeNe laser line at 6329A. The laser beam was introduced into the chamber interior through an optical fiber from the laser unit mounted outside the chamber. This arrangement worked almost adequately, even though with some mystery, during some time period in the balloon flight the laser fringe signal modulation diminished to a low figure. Fortunately, the modulation returned to a healthy value during the last half of the observation period.

The interferometer drive system was designed to reproduce its scanning motion with a high degree of accuracy. Its starting position was to occur within 1.0μm at a distance of 250μm from the central maximum position of the interferogram. The scanning was to change its direction approximately at a distance of 10 cm on the other side of the central maximum position. The mechanical accuracy of this degree was required for the interferometer scanning because of two main reasons: (1) no optical means of detecting the central maximum position could be implemented in our setup because they would cause a devastating effect on the spectral sensitivity of the instrument; and (2) the detector electronics scheme was designed to make use of the reproducible interferometer scanning. One complete cycle of the interferometer scanning consisted of 20-seconds forward motion during the interferogram measurement phase and 10-seconds reverse motion. The detector amplifier was programmed to switch its gain to a higher setting at the 800th data point from the starting position. Any malfunction in the scanning would cause an irreparable damage to the interferogram data collection, since

the central maximum and the consequent gain switching would occur at a wrong place. We were able to maintain the interferometer scan satisfactorily during the entire balloon flight.

We can write the signal intensity S reaching the detector by

$$S = BA\Omega(\Delta\sigma)T\eta$$

using the parameters defined below:

B = signal radiance per a unit cross-sectional area of the incident beam, a unit solid angle, a unit wavenumber interval, and a unit time;

$\Delta\sigma$ = spectral resolution;

A = aperture area of the interferometer mirror;

Ω = solid angle subtended by the detector;

T = time period covered in the measurement; and

η = optical transmission efficiency.

The solid angle Ω subtended by a detector circularly shaped is determined by [9]

$$\Omega = 2\pi/R,$$

where R is the resolving power at the highest wavenumber end of the observed spectral bandpass. The amount of noise generated by the detector during the same time interval is given by

$$N = \frac{\sqrt{Ad}\ \sqrt{T}}{D^*}$$

where D* is the normalized detectivity of the detector, and Ad is the detector's area.

The measurement sensitivity can be conveniently specified by the noise equivalent spectral radiance

$$NESR = \frac{\sqrt{Ad}\ \sqrt{T}}{D^*A\Omega\eta(\Delta\sigma)}$$

which is equivalent to the spectral radiance giving the S/N of unity. The detector's noise is controlled by two factors, the thermal noise of the detector at its operating temperature and the fluctuation of the background photon stream. With reducing the spectrometer's operating temperature, the latter contribution to the detector noise should be substantially reduced. The detector sensitivity is, therefore, expected to show an improvement.

Electronics

The interferogram signal level was expected to vary a large amount by more than one order of a magnitude between the maximum at the ground level and the minimum at the ceiling altitude of approximately 30 km. The detector amplifier was designed to accommodate this large signal variation by implementing an automatic gain adjustment scheme. The lower gain setting of the amplifier in the central maximum region was adjusted by degree of the previous central maximum modulation. As mentioned earlier, the amplifier was programmed to switch its gain setting to a higher value by the ratio of 5.64 at the 800th data point

from the starting position of the interferogram scanning.

The digitized interferogram data and other pertinent signals for the experiment were transmitted to the ground station through a telemetry radio link. A schematic block diagram shown in Fig. 3 illustrates the path of all electronic signals included in our experiment. A crucial requirement for the data transmission was to satisfy the condition that in Fourier spectroscopy every interferogram data point, equally critical to the spectral recovery, should not be lost in any circumstances. The data electronics were designed to satisfy this requirement. The interferometer scanning was set at a rate of 4500 interferogram data per second for 20 seconds in a single scan. The data were made into a 16-bit word format, a 12-bit interferogram data, and an additional 4-bit interferogram status. The telemetry signal was made into a total of 72-bit string, which consisted of a 20-bit synchronization code, a 16-bit interferogram data, a 4-bit frame count, and four other data. It was transmitted at 800K bits per second, or at approximately 11.1K telemetry frames per second. Thus, the telemetry data were transmitted at a rate approximately 2.5 times faster than the interferogram data acquisition, thereby accommodating the non-uniform interferometer scanning speed.

Flight Package

The flight package shown in Fig. 4 was assembled by the University of Denver. The infrared atmospheric emission signal was admitted to the cold chamber interior via a ZnSe window which remained at ambient temperature. An assembly which consists of a plane mirror intercepting the interferometer's line of sight to direct toward a vertical direction and a blackbody source was implemented for the purpose of providing the down-looking observation and the on-board radiance level calibration. This assembly was mounted just outside the ZnSe window with a trolley structure which could place the assembly at three positions by the command sent from the ground station. The first position called for a clear view to allow interferometer's line of sight at the horizontal direction. Nothing obstructed its view. The second was to place the blackbody source in the field of view for accommodating the radiance level calibration, and the third was to direct the line of sight toward the downward direction by placing the intercepting mirror. In addition to this mirror-blackbody arrangement, the entire flight package was set to tilt by the command given from the ground. With this arrangement the interferometer's line of sight could be raised up to 10 degrees from the horizon.

Balloon Flight

The flight profile, given in terms of the balloon altitude as a function of time, was monitored using radar on the ground. It is shown in Fig. 5 with the local temperature measured with a thermistor bolometer hung below the gondola. The measured value of the total

radiance level is also shown in the figure. Even though the laser signal failure which occurred during some part of the flight resulted in some loss of the data, the interferometer produced the analyzable data for more than two hours at the maximum balloon altitude. The spectral data obtained during the flight consisted of three parts: (1) the data along the horizontal line of sight; (2) the data along the vertical line of sight; and (3) the radiance calibration spectra obtained using an on-board blackbody source which was presumably in thermal equilibrium with the ambient. As seen in the thermistor bolometer data, the ambient temperature at the altitude of 28000 m ∿ 28500 m fluctuated between 270 K and 250K, closely correlating with the balloon motion. The data indicated that the stratospheric ambient temperature measured with the on-board thermistor was considerably higher than that of the model atmosphere, and that its fluctuation was unexpectedly large.

Our balloon flight was accompanied by two radio-sonde flights. The temperature measured by the radio-sonde sensor was at most 230K, as seen in Fig. 6, at this altitude range, much lower than the temperature measured with the on-board thermistor. The on-board instrument consumed a power of approximately 250W ∿ 300W. Since there was no energy sink provided in the flight package, the consumed energy by the on-board instruments was eventually removed to the ambient atmosphere through thermal radiation. Thus, the temperature of the instrument package had to remain considerably higher than the local surrounding. A difference of 20 ∿ 30K between the temperature registered by our balloon-borne thermistor and the radio-sonde sensor was found within the estimate

given based on the general configuration of the flight instrument.

Calibration of the Radiance Level

Two sets of spectra were taken using the on-board blackbody source, one at 17:30 GMT and another between 18:45 and 19:30 GMT. Both sets were taken at the balloon ceiling altitude of 28000 m. Their spectral characteristics as well as their radiance levels were found very similar. We estimated these spectra to be those of a 255K blackbody radiance, and proceeded to calibrate all the measured spectral data, horizontal-looking and down-looking, accordingly. The calibrated down-looking spectra showed the radiance level at the center of the CO_2 15μ band corresponding to 215K $\sim$ 220K and that of the window region to the ground temperature of 285K. The radiance level obtained for the down-looking spectra was, therefore, consistent with the atmospheric radiative transfer expected for this spectral region.

The radiance level of the interferogram signal was estimated with respect to the noise level contained in it. Since no information on the gain factor of the detector amplifier was transmitted to the ground, it had to be determined from the recorded interferogram data. The noise level in the interferogram data increased or decreased whenever the detector amplifier switched its gain setting. Since we had no reason to believe that the absolute level of noise in the interferogram signal varied from time to time, we determined the gain of the detector amplifier using the noise level observed in the recorded

interferogram signal. We observed the noise level stepped in accordance with the step in the amplifier gain setting. Therefore, our procedure for estimating the detector amplifier gain was self-consistent. The total radiance level received by the spectrometer was proportional to the central maximum modulation and it was estimated by multiplying the central maximum modulation with the gain factor which was determined from the noise level observed in the interferogram very far from the central maximum.

An exception to the procedure for the radiance calibration had to be observed for the data taken after 19:30 GMT, when the blackbody source was removed from the field of view at the last time in the flight. The radiance level determined using the procedure above showed a dramatic increase for the horizontal-looking spectra taken after 19:30 GMT, while the balloon altitude and the measured ambient temperature remained unchanged as before. At that time, the liquid helium level in the detector dewar became definitely low and the detector temperature started to rise. We reasoned that the apparent increase of the radiance level after 19:30 GMT, shown by a solid curve, was resulted by an improved noise figure of the detector, rather than by an increase in the incident radiance level. The radiance level probably remained at the same level, as indicated by a dotted curve. Anyway, the data obtained after 19:30 GMT certainly had a larger degree of ambiguity than the rest because the radiance level calibration was not repeated after the observation of these spectra. Our discussion on the obtained data will be made excluding the data collected after 19:30 GMT.

The spectral response of our spectrometer was determined using the blackbody calibration spectrum. As described above, the calibration source was assumed at 255 K. The obtained blackbody spectrum and the determined radiance level given as a function of wavenumber are shown in Figure 7. The obtained curves were used to determine a relative value of the radiance level at each wavenumber position. The absolute value of the radiance level was then determined by normalizing the integrated relative radiance value to the total radiance level obtained using the procedure described above.

Recovery of the Spectral Data

The telemetry signals recorded on magnetic tapes were brought back to the University of Massachusetts for retrieval of the data obtained during the flight. First the telemetry tapes were played back and the interferogram data were extracted using the PDP11 computer with a PCM telemetry signal decoder. Then the recovered raw interferogram data were recorded on the 7-track digital magnetic tapes. The rest of the numerical process was done on the CDC Cyber computer system at the University of Massachusetts. Since some of the data were sampled with faulty sampling intervals caused by insufficient laser interference modulation, the interferogram data were inspected one by one prior to application of the numerical Fourier transformation process. The interactive feature developed by us on the CDC system provided an extremely efficient inspection on the raw data displayed on the CRT terminal. The phase correction operation which followed the

interferogram inspection was applied individually to the examined interferogram data. The spectral recovery process was carried out with the sinc instrument function of a basic sampling interval of 0.24 cm^{-1}. Even though the interferogram data extended more than the optical path difference of 4.2 cm, a limited signal-to-noise ratio in the data necessitated a premature termination of the data processing at approximately 2.07 cm of the optical path difference [corresponding to the resolution figure of 0.48 cm^{-1}].

The Obtained Spectral Data

The major atmospheric bands observable in our measurement are CO_2 ($\Delta\nu_2 = 1$) transitions.[11] All bands contain a strong Q branch. Table I lists the band center for the observable transitions. The Q branch of the (01101-00001) band of $^{12}C^{16}O_2$ isotope should show a strong saturation even at our balloon altitude . The radiance level at the center of the Q branch serves as a temperature indicator of the air surrounding the balloon . With the assumption that the CO_2 concentration in the stratosphere is given by the well-established mixing ratio of 3.3×10^{-4} , our observation along the horizontal line of sight was expected to be made with the CO_2 column density of approximately 5.0×10^{20} molecules/cm^2 .

The emission spectra observed along the vertical line of sight is presented in Figure 8. All data observed along the vertical line of sight differed very little among them in their spectral characteristics as well as of their radiance level. The source radiance level in the 675 cm region was found to be approximately 4.0 x 10^{-6} W/cm^2 str cm^{-1}, the blackbody radiance level of 210∿220 K. The level in the 800 cm^{-1} was 1.1 x 10^{-5} W/cm^2 str cm^{-1}, consistent with the concurrently measured ground temperature of 285 K. The theoretical spectrum calculated using the FASCOD1B code[12] with the AFGL atmospheric line parameters[11] is shown in Figure 9. No significant differences were observed between the measured and calculated data.

The data observed along the horizontal line of sight showed their spectral characteristics very little different from each other. The difference observed in their radiance level is clearly indicated in the data of Figures 10 and 11, which were taken at 18:15 GMT and 18:45 GMT. A continuum feature which amounted to the radiance level of 2∿3x 10^{-6} W/cm^2 str cm^{-1} at the 600 cm^{-1} region, is probably due to the emission of the ZnSe window. A large fluctuation in the radiance level at the 675 cm^{-1} region indicates a rather large temperature fluctuation in the ambient atmosphere.

A theoretical spectrum shown in Figure 12 was generated using the FASCOD1B with the CO_2 column density of 1.2x10^{21} molecules/cm^2 at 220 K. The theoretical and the observed disagree by a large amount.

AD-A147 517 STUDY OF INFRARED ATMOSPHERIC EMISSION(U) MASSACHUSETTS 2/2
UNIV AMHERST ASTRONOMY RESEARCH FACILITY H SAKAI
DEC 83 UMASS-ARF-83-333 AFGL-TR-84-0006
UNCLASSIFIED F19628-81-K-0007 F/G 17/5 NL

1.0
2.8
2.5
3.2
3.6
4.0
2.2
2.0
1.8
1.1
1.25
1.4
1.6

Acknowledgement

This work is supported by AFOSR under the atmospheric science project 2310 and performed as part of AFGL Task 2310G1. We acknowledge W.Gallery of AFGL who provided the theoretical spectra calculated using the FASCOD1B code. T.C.Li, S. Pulchtopek, and W. Barowy of the University of Massachusetts did most of the data reduction. F.H.Murcray and J.Williams of University of Denver made their contribution on the balloon instrumentation. A . Giannetti of AFGL headed the balloon launching operation.

References

†The material covered in this paper was presented in a preliminary form at the following Conferences:
(a) 1981 International Conference on FTIR, Ref. 3;
(b) Ref. 4;
(c) Ref. 5;
(d) Annual Meeting of the Optical Society of America, Sakai, H. and Vanasse, G., J. Opt. Soc. Am. 72, 1724 (1982).

1. Goody, R.M., Atmospheric Radiation I. Theoretical Basis, Oxford, London (1964).

2. Clough, S.A. *et al*, SPIE Publ. 277, 152 (1981).

3. Sakai, H. *et al*, Proc. 1981 Int'l Conf. on FTIR, SPIE Publ. 289, 196 (1981).

4. Sakai, H. *et al*, SPIE Publ. 364 (1983).

5. Sakai, H. and Vanasse, G., SPIE Publ. 366, 165 (1983).

6. Goldman, A., Murcray, D.G., Murcray, F.J., and Niple, E., Appl. Opt. 19, 3721 (1980).

7. Yates, H.W., Appl. Opt. 21, 203 (1982).

8. Vanasse, G. and Sakai, H., Progress in Optics, Vol. VI, Ed., E. Wolf, pp. 259-330, North-Holland, Amsterdam (1967).

9. Sakai, H., Proc. Aspen Int'l Conf. on Fourier Spectroscopy, 1971, AFCRL Report 71-0019, pp. 19-41 (1971).

10. Sakai, H., Spectrometric Techniques, Vol. I, Ed., G. Vanasse, pp. 1-70, Academic Press, New York (1977).

11. McClatchey, R.A. *et al*, AFCRL Report TR-73-0096 (1973); NTIS #AD 762 904.
Rothman, L.S., Appl. Opt. 20, 791 (1981).
Rothman, L.S. *et al*, Appl. Opt. 20, 1323 (1981).

12. Clough, S.A. *et al*, Ref. 2.

Table I

Major CO_2 Bands in the 700 cm^{-1} Region

Band	Isotope	Band Center
01101-00001	626	667.4 cm^{-1}
10001-01101	626	720.8
10002-01101	626	619.8
02201-01101	626	667.8
03301-02201	626	668.1
01101-00001	636	648.5
01101-00001	628	662.4

Figure Captions

Figure

1 Interferometer assembled on a base plate.

2 Interior of Cryogenic Chamber.

3 Front View of the Entire Package.

4 Schematic Diagram of Instrumentation.

5 Profile of Flight, October 1981.

6 Radio-Sonde Records.

7 Blackbody Source Calibration Curve.

8 Spectrum observed along the vertical line of sight.

9 Synthetic spectrum computed for the vertical line of sight.

10 Spectrum observed along the horizontal line of sight: 18:15 GMT.

11 Spectrum observed along the horizontal line of sight: 18:45 GMT.

12 Synthetic spectrum computed for the horizontal line of sight:
CO_2 column density = 1.2×10^{21} molecules/cm^2,
temperature = 220°K.

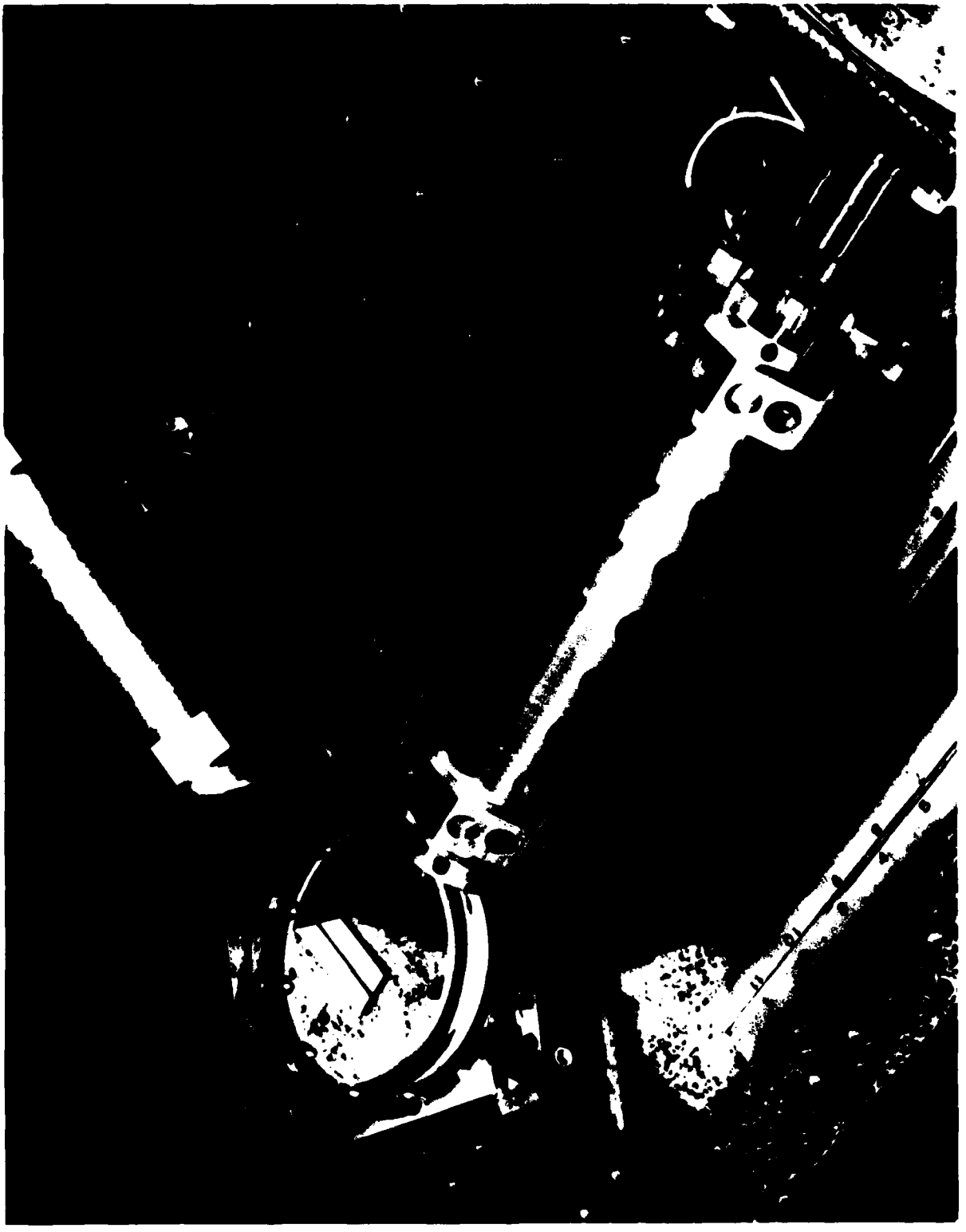

Figure 1

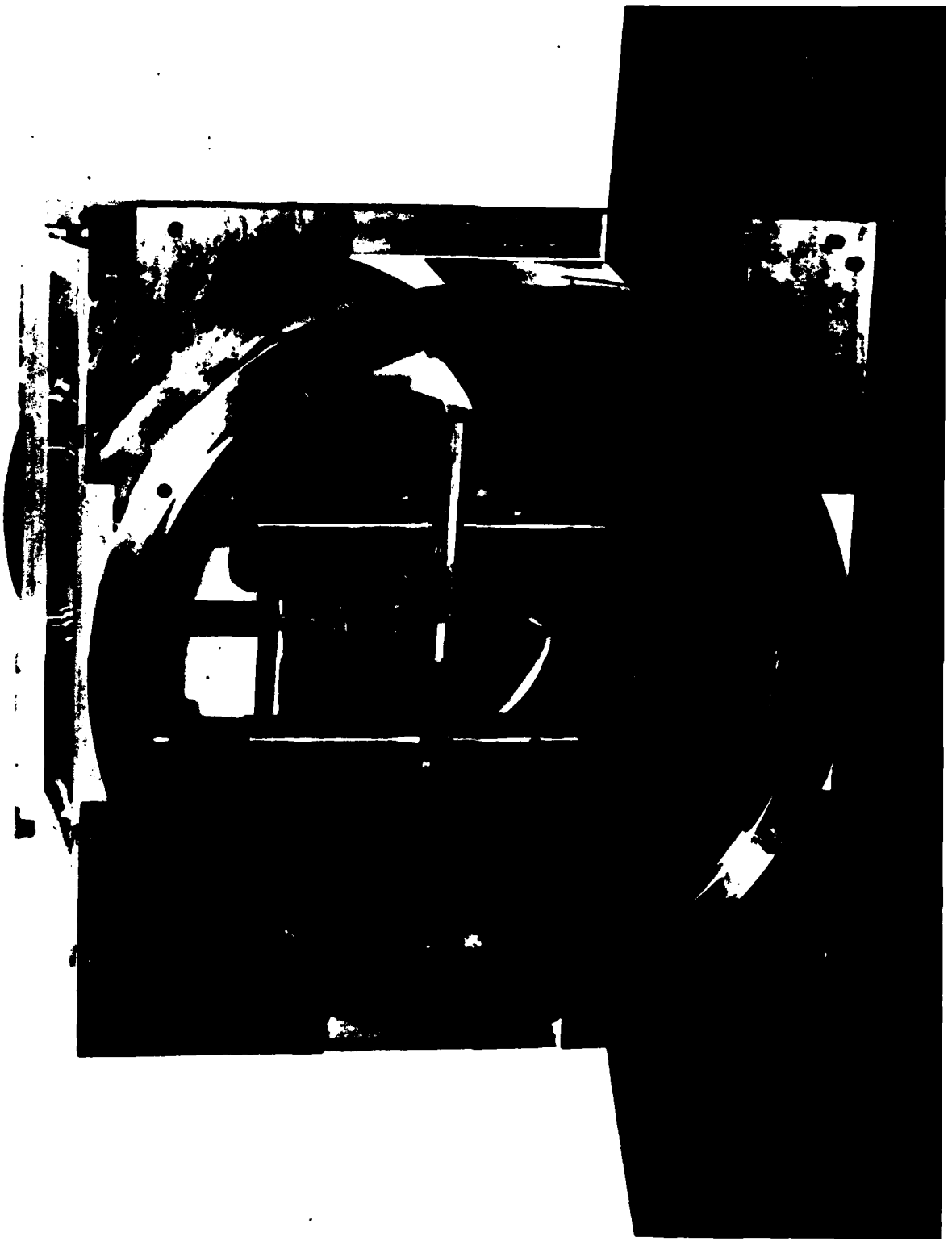

Figure 2

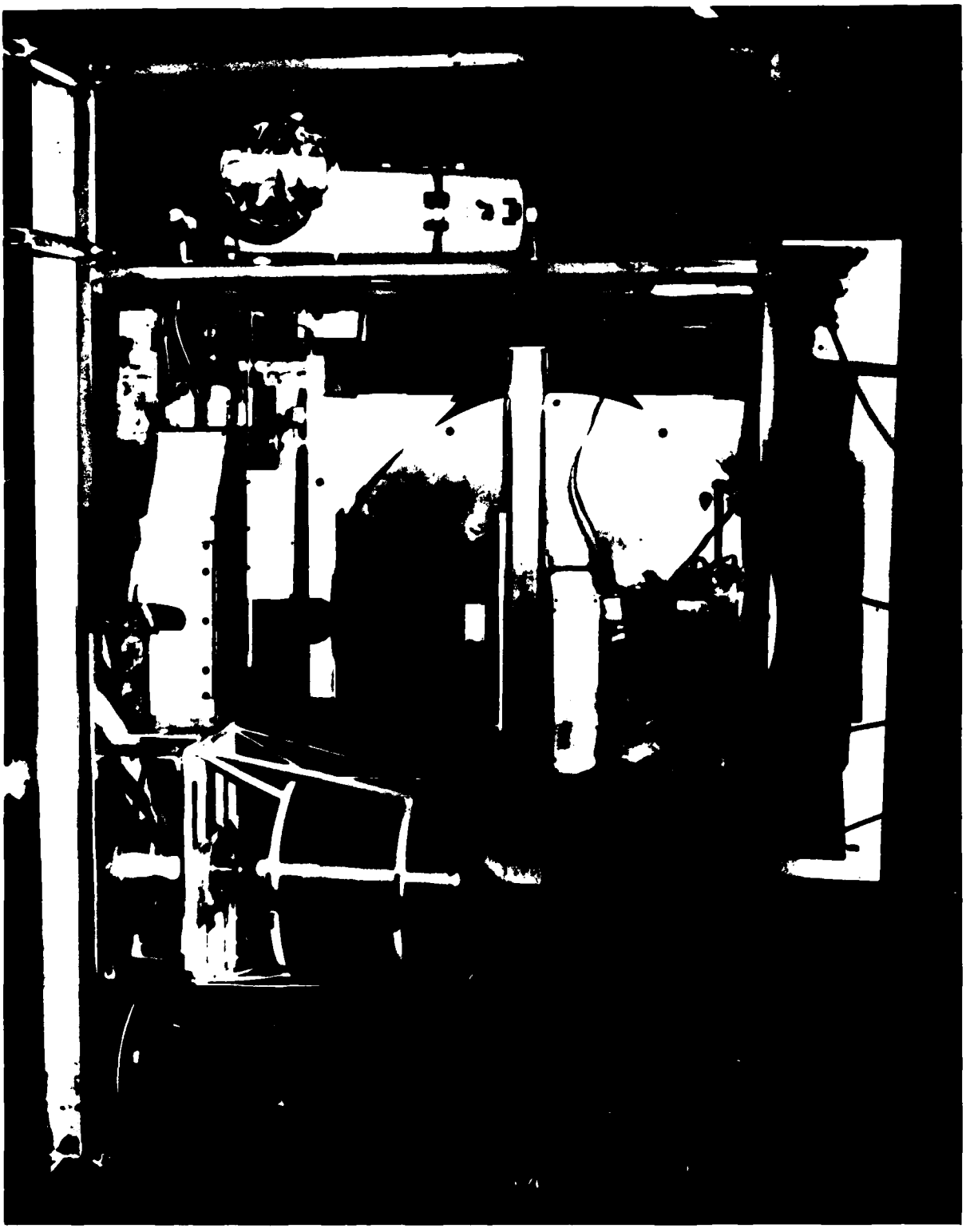

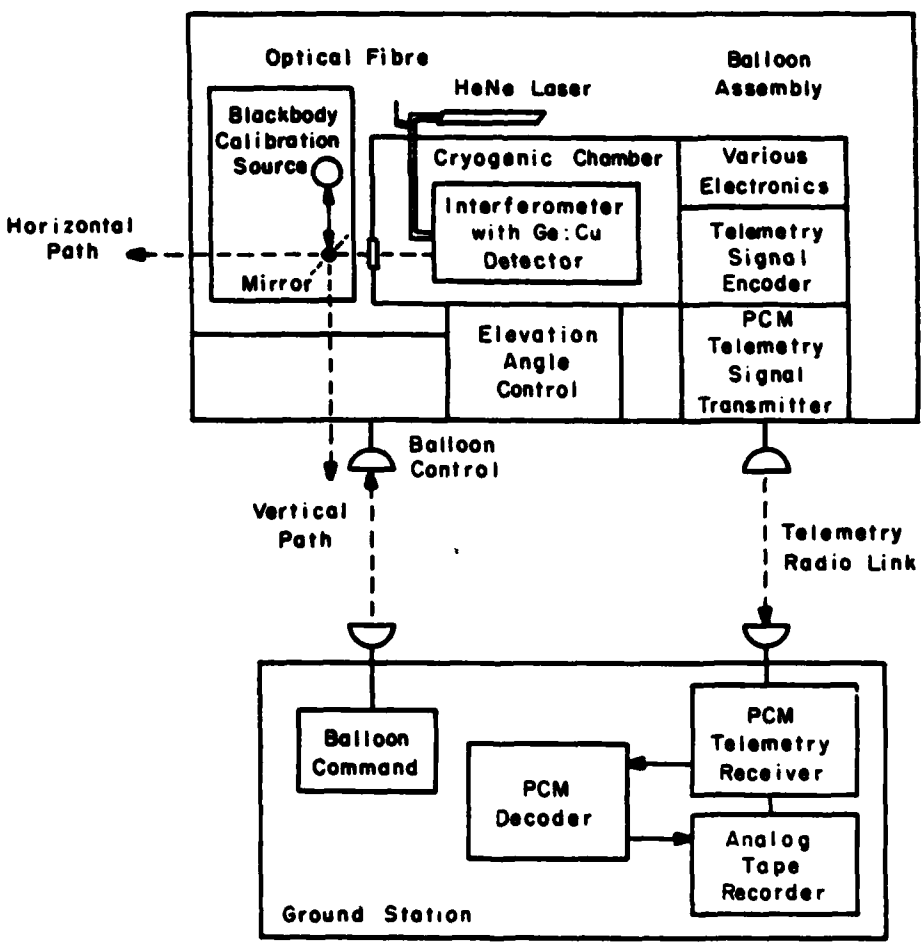
Optical Fibre
HeNe Laser
Balloon Assembly
Blackbody Calibration Source
Cryogenic Chamber
Various Electronics
Interferometer with Ge:Cu Detector
Horizontal Path
Mirror
Telemetry Signal Encoder
Elevation Angle Control
PCM Telemetry Signal Transmitter
Balloon Control
Vertical Path
Telemetry Radio Link
Balloon Command
PCM Decoder
PCM Telemetry Receiver
Analog Tape Recorder
Ground Station

Figure 4

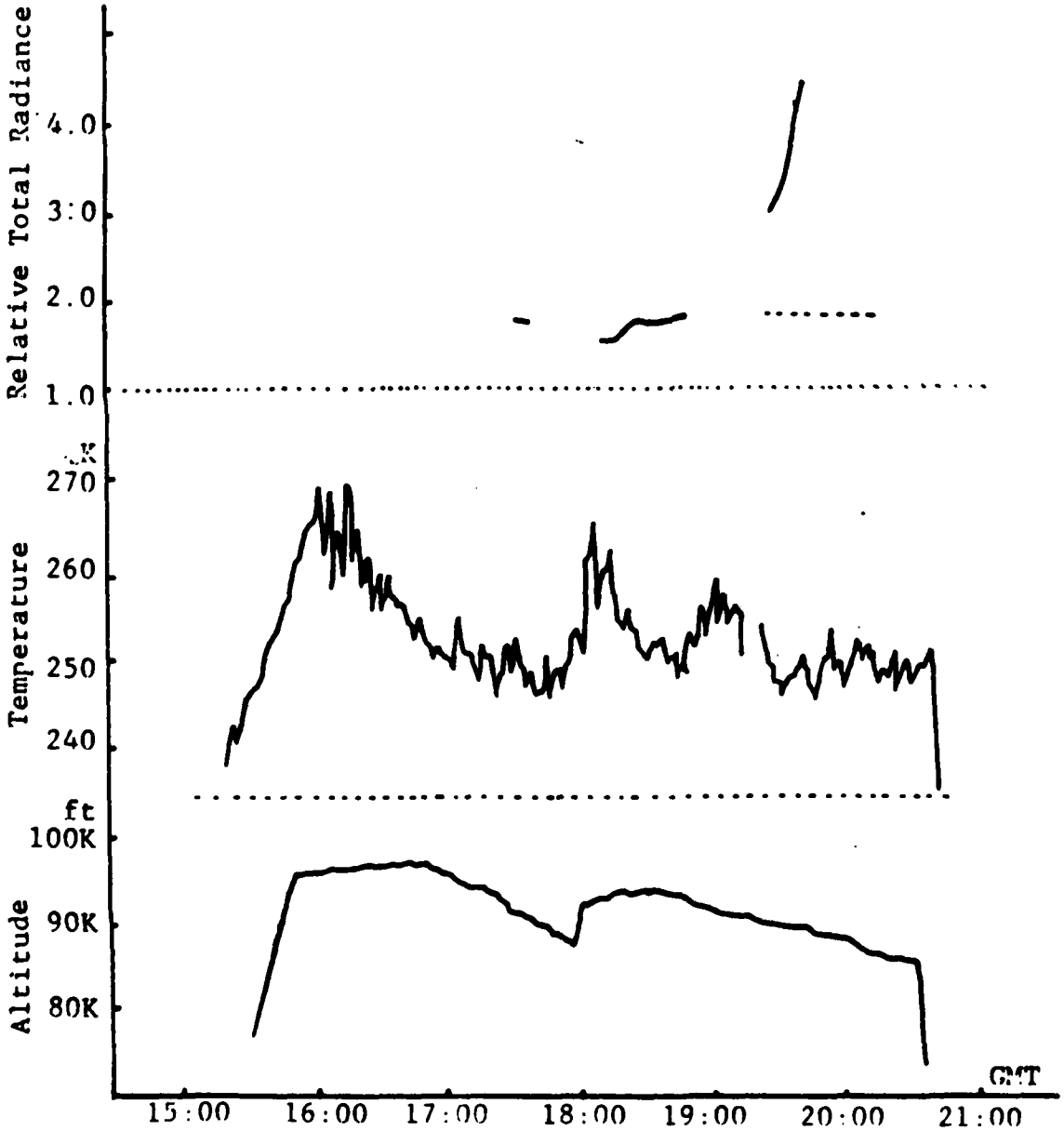
Relative Total Radiance
4.0
3.0
2.0
1.0
Temperature
270
260
250
240
ft
Altitude
100K
90K
80K
GMT
15:00
16:00
17:00
18:00
19:00
20:00
21:00

Figure 5

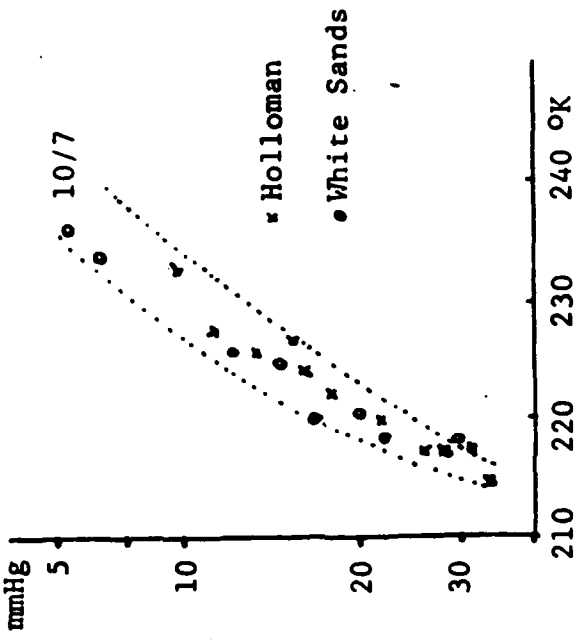

Figure 6

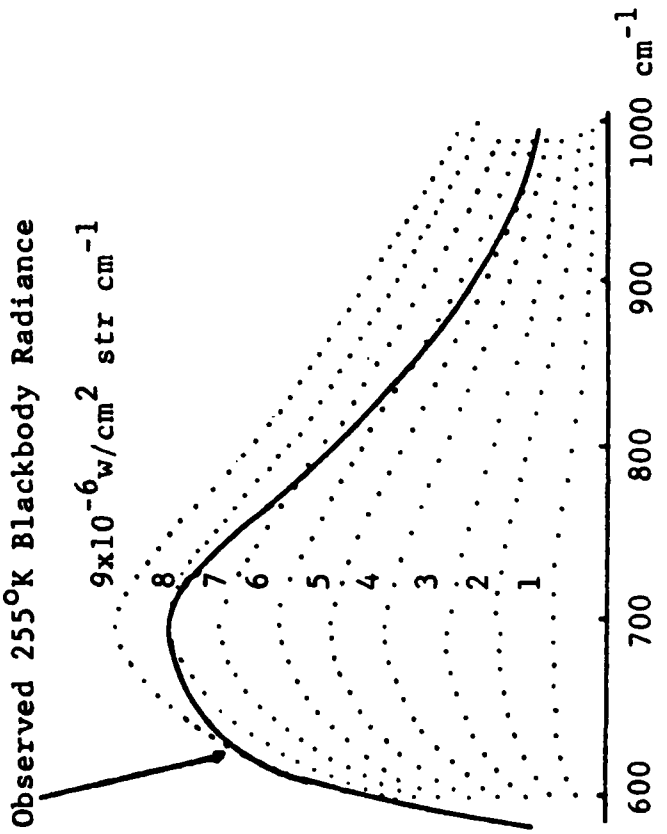
Observed 255°K Blackbody Radiance
9x10⁻⁶w/cm² str cm⁻¹
8
7
6
5
4
3
2
1
600
700
800
900
1000 cm⁻¹

Figure 7

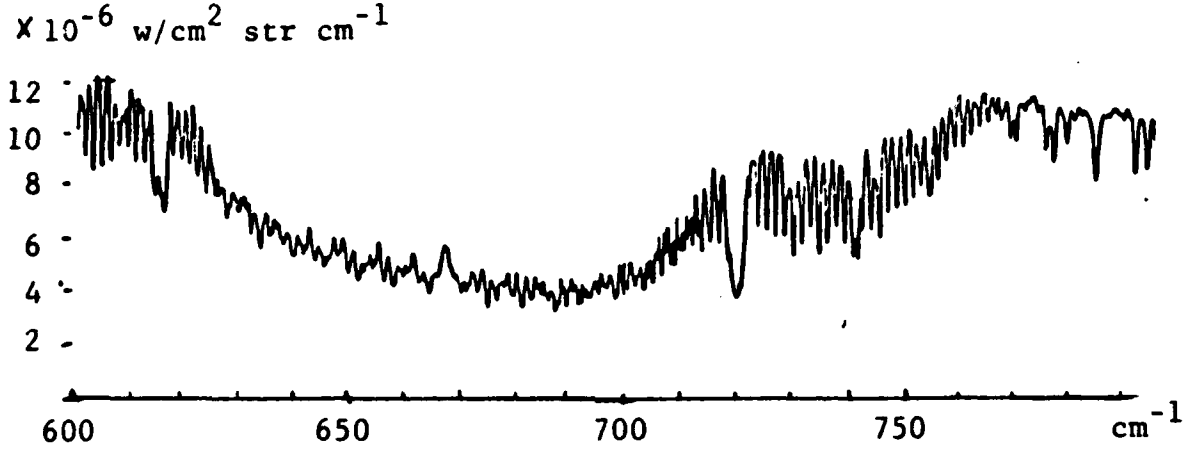
X 10-6 w/cm2 str cm-1
12
10
8
6
4
2
600
650
700
750
cm-1

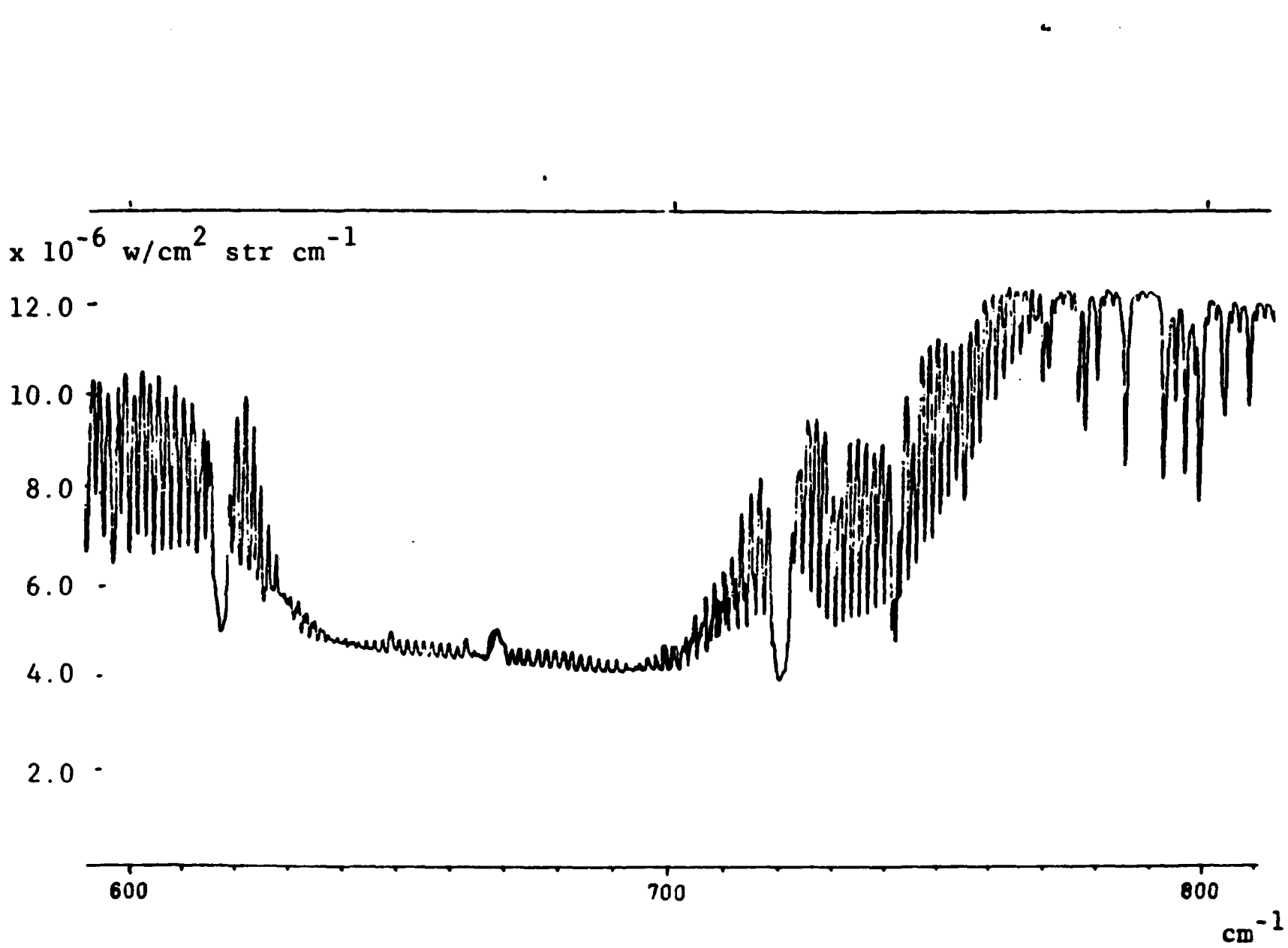
x 10^-6 w/cm^2 str cm^-1
12.0
10.0
8.0
6.0
4.0
2.0
600
700
800
cm^-1

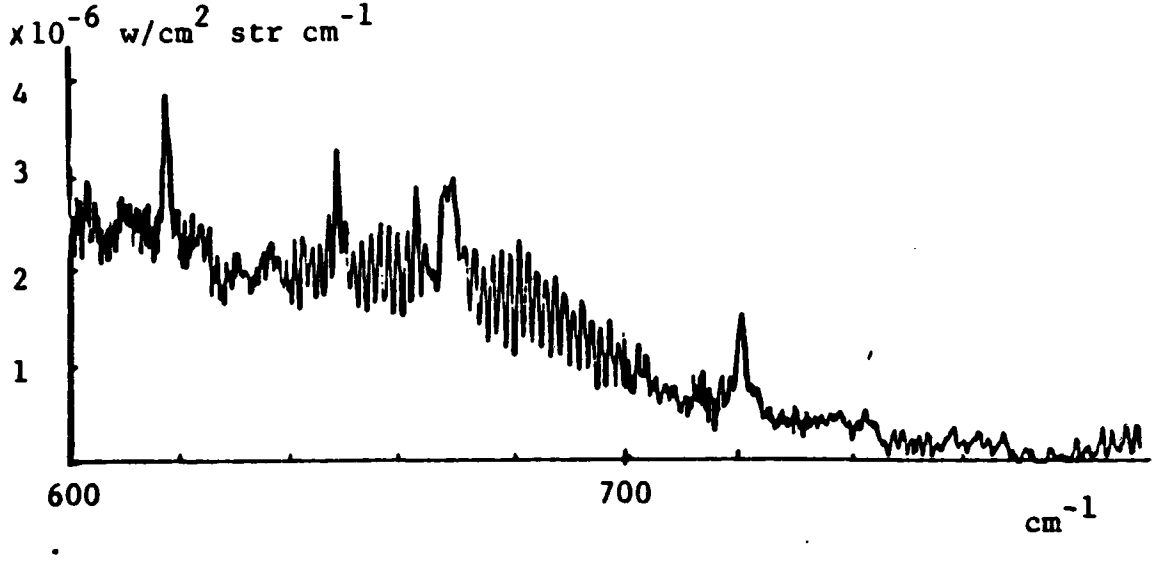
x10^-6 w/cm^2 str cm^-1
4
3
2
1
600
700
cm^-1

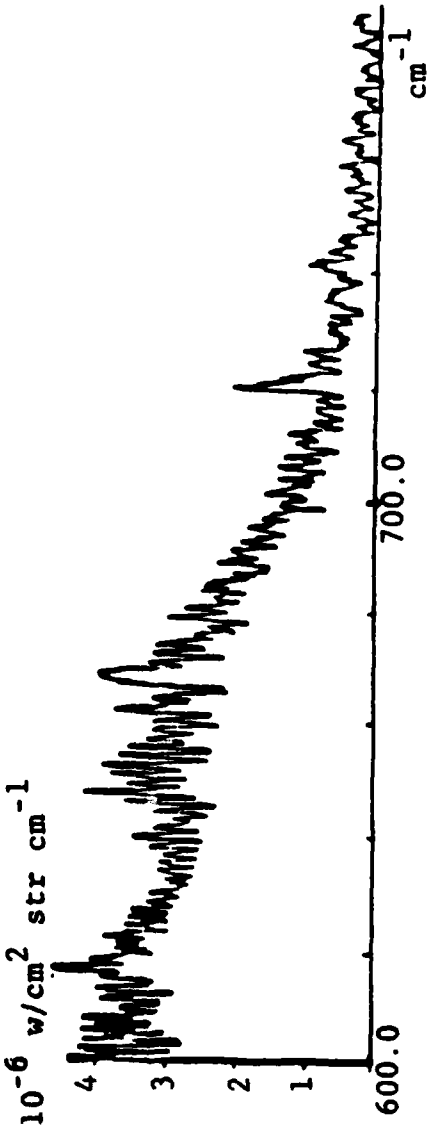

Figure 11

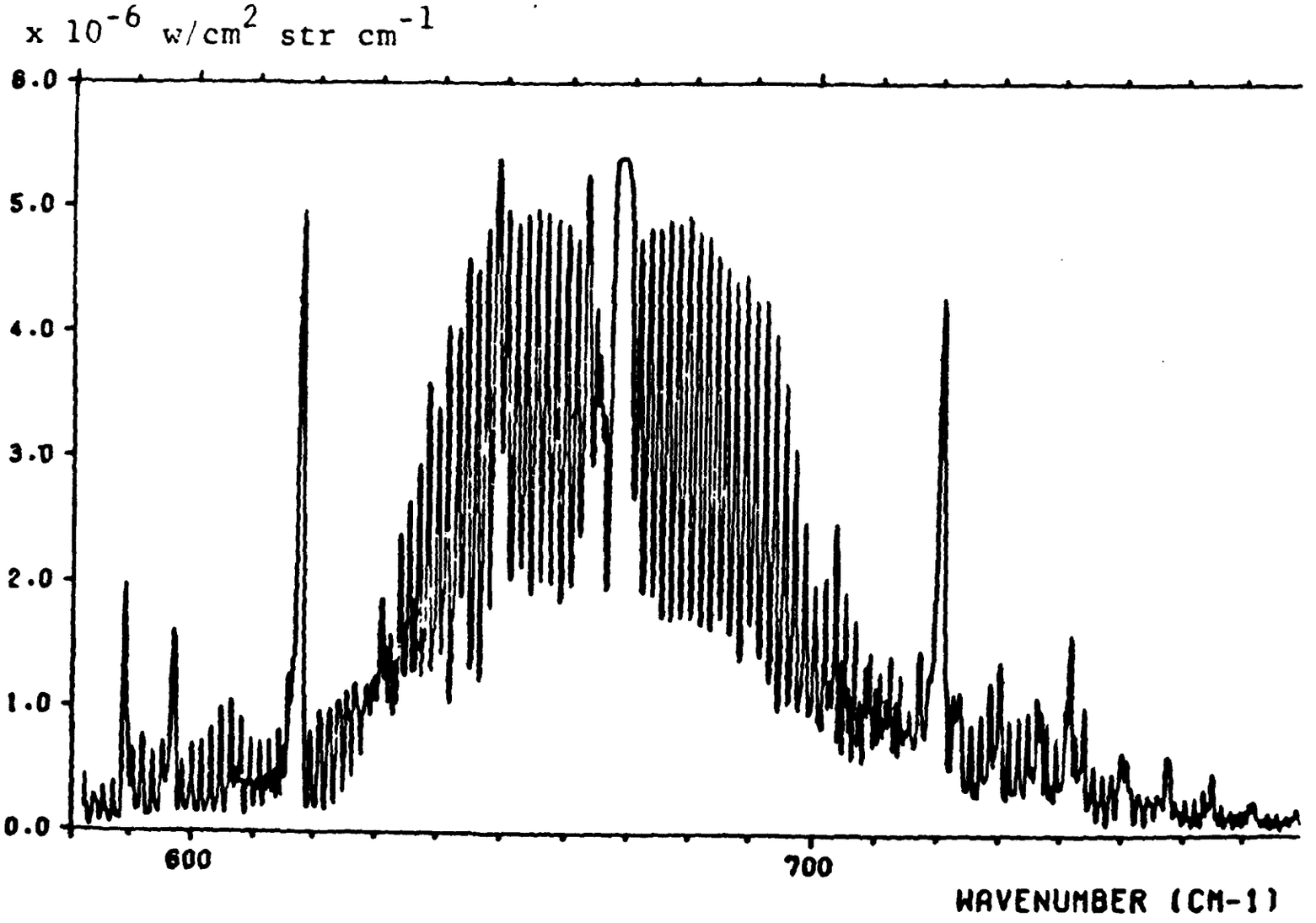
x 10^-6 w/cm^2 str cm^-1
6.0
5.0
4.0
3.0
2.0
1.0
0.0
600
700
WAVENUMBER (CM-1)

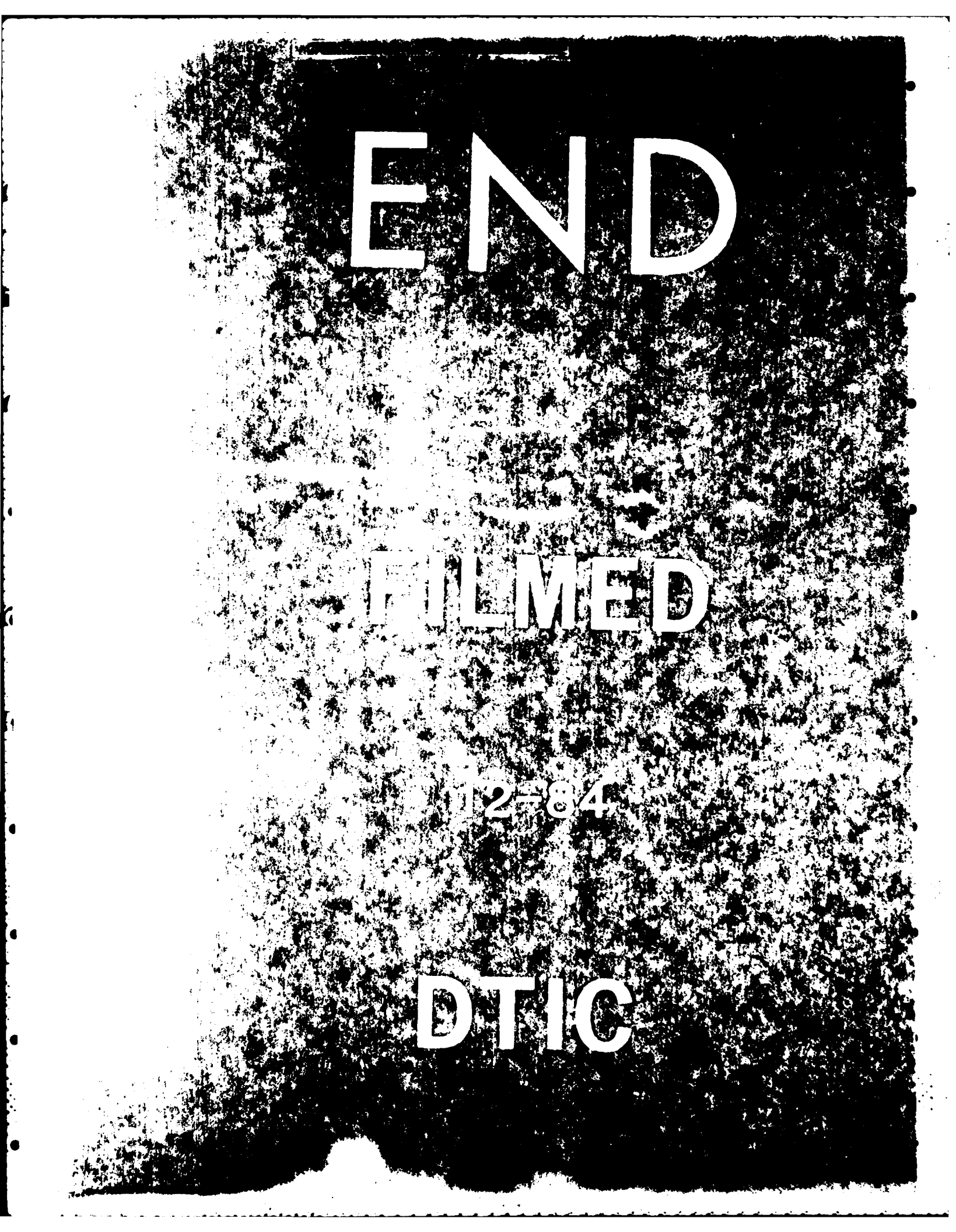
END
FILMED
12-84
DTIC